INVESTIGATION OF THE POSSIBILITY OF HIGH EFFICIENCY L-BAND SRF CAVITIES FOR MEDIUM-BETA HEAVY ION MULTI-CHARGE-STATE BEAMS

By

Safwan Shanab

A DISSERTATION

Submitted to
Michigan State University
in partial fulfillment of the requirements
for the degree of

Physics – Doctor of Philosophy

2020

ABSTRACT

INVESTIGATION OF THE POSSIBILITY OF HIGH EFFICIENCY L-BAND SRF CAVITIES FOR MEDIUM-BETA HEAVY ION MULTI-CHARGE-STATE BEAMS

By

Safwan Shanab

The possibility of using 1288 MHz (L-band) SRF elliptical cavities to accelerate heavy ion multi-charge-state (up to 5 charge states) beams is being investigated for accelerating energy higher than 200 MeV/u. This cavity can be a potential energy upgrade for heavy ions linac accelerators such as the Facility for Rare Isotope Beams (FRIB) in the United States of America and Rare Isotope Science Project (RISP) in Korea. One of possible disadvantages of the L-band frequency structure is its small longitudinal acceptance. It should be sufficiently large for transporting the ions with the limited beam loss ensuring accelerator hands-on maintenance.

A first simple analytic study was performed and it showed a promising result with 1288 MHz linac. In addition, from beam loss point of view, the study deduced that 1288 MHz linac frequency could be the limit for medium-beta heavy ion up to five charge states beam accelerators. This work is the result of the detailed beam dynamics simulation for the linac performance using TRACK code to confirm the analytic result. The result shows that the longitudinal acceptance is large enough for medium-beta heavy ion with five charge state beams. Usually accelerator upgrade projects have limitations such as environment, space, and cryogenic cooling plant. Thus, high frequency and high gradient cavity is demanded to resolve such limitations. Exploiting cavity nitrogen doping technology would be beneficial for efficient cryogenics.

Nitrogen doping technology has shown that it is more beneficial for higher frequencies cavities. This impact on BCS surface resistance (R_{BCS}). R_{BCS} is proportional to the frequency squared, nitrogen doping technology benefit is larger in the higher frequencies. For instance, the benefit is larger at 1300 MHz cavity than low frequency cavities such as 650 MHz cavity. That is due to the fact that BCS surface resistance, R_{BCS} (depends on temperature and electron mean free path of the niobium material) is higher than the residual surface resistance, R_{res} (Temperature independent) in higher frequencies. The Research and Development (R&D) of nitrogen doping technology is still on going. However, our neon doping proposal to give us more insight on the physics of nitrogen doping of RF surfaces and confirm or refute the assumption that the interstitial nitrogen atoms play the role of improving the cavity intrinsic quality factor not the nitrogen nitride (NbN) chemical compositions hasn't been implemented yet, it is still an open question.

Dedicated to my great parents and to the Arabs and Muslims who invented the number zero (0), who introduced the Arabic numbers, who invented Algebra (In Arabic “al-jabr”, it means fixing broken things) by the father of Algorithm the great Al-khwarizmi, who wrote the first book in medicine called “The Canon of Medicine” (it means the law of medicine in Arabic) by Avicenna, who invented the surgery tools, who named most the known stars, who introduced the idea of separation of church and state by Averroës, who had the Second Teacher, Al-Farabi...etc.

ACKNOWLEDGMENTS

The list of my appreciation and gratitude to who supported me through my Ph.D. program. It is what I was able to remember at the time of writing this dissertation. I apologize if I forgot anybody else.

Kenji Saito is my advisor. I learned a lot from him since I was an undergraduate student and still do. He is a very smart teacher, a great mentor and a good friend and I am glad to have him as my advisor. It is an honor for me to know him and work with him on very interesting challenging physics problems.

Yoshishige Yamazaki was my guidance through my research he provided me a great support and whenever I face any troubles, I find the first who is willing to help me.

Steve Lund always wants to me to be and do better and improve my research skills. He knows me and what I have gone through and he always offers his support to me.

Jie Wei is my Ph.D. committee member. He supported me during my school years.

Morten Hjorth Jensen is my Ph.D. committee member. He taught me a computational physics class and his way of teaching of how we can utilize computer coding to solve physics problems was very interesting and easy to follow.

Chong-Yu Ruan is my Ph.D. committee member and he taught me Advanced Physics lab course when I was an undergraduate student at MSU. His way of linking the theory to experiment observation was very helpful to get the big picture of a physical phenomenon.

Pashupati Dhakal was a great host and mentor during my visit to Thomas Jefferson Lab in Virginia and he is a great expert in SRF technology. I learned from him SRF cavity

preparation, cavity diffusion technology and RF cavity testing and much more during my visit.

Peter Ostroumov trained me in learning accelerator components, helped me to learn how to use TRACK code, and provided me with a FRIB linac layout in TRACK.

Brahim Mustapha helped me to learn how to use TRACK code and explained to me how to use the MATCH and OPTIM features in TRACK.

Felix Marti helped me by asking me questions to improve my understanding of physical concepts.

Alexander Plastun is an easygoing person who was always available to help me. I took so much time from him and probably bothered him with my endless questions. I learned a lot from him.

Haitao Ren is a good friend, mentor and teacher. He taught me so much on hands-on accelerator operations. He is an expert on accelerator components commissioning and operation.

Ting Xu helped me through my research and I learned from him and still do how to manage science projects efficiently, by observation.

Chris Compton helped me during my research. He was always available to help me. Even when he was busy with other projects, he managed to provide me the help that I needed.

John Popielarski is an easygoing person, friendly and a good teacher. I learned from him cavity vertical testing and still do. He is an expert in RF testing.

Laura Popielarski helped me by letting me use the clean room tools to conduct my research. She is friendly and very organized.

Kyle Eliot helped me in cavity disassembly and he was always willing to help whenever I needed.

Walter Hartung is a very smart physicist. He knows a lot. I have had very interesting discussions with him and he is very friendly and a very easygoing person. Looking forward for any collaborations with him in R&D projects.

Joseph Asciutto helped me in finding the cavity bolts and he was always ready to help me even when he was busy he tried to assist me whenever he can.

Scott Hitchcock, this person has a solution for every problem one have might encounter in the lab. To me his experimental knowledge is powerful.

Matt Hodek helped me how to use RF equipment and computer programs. He was very friendly and a good teacher.

Earle Burkhardt helped me in learning the concepts of magnet designs, which help me in designing the magnetic quadrupole.

Winter Zhang helped me in cavity simulations and RF testing. He is a good friend and mentor.

Sang-hoon Kim helped me in learning SRF cavity testing.

Didi Luo who was classmate and she is my fellow in our Ph.D. program. She is a good friend.

Saravan K. Chandrasekaran supported me during the start of my Ph.D. program.

Sergey Stark who I learned from him on power couplers testing.

Remco Zegers who provided me with a lot of support during my start of my Ph.D. program.

Artemis Spyrou who helped a lot me during my research program. She was my professor when I was an undergraduate student at MSU. I learned a lot from her.

Kim Crosslan is the secretary of graduate school of Astronomy and physics at MSU. She is the coolest woman ever. She is amazing and she is a nice person to talk to.

Mengxin Xu is very easygoing person. He is very friendly. He always ready for help whenever I need to.

Wei Chang is very friendly. He taught me a lot on RF testing and I still learn from him.

Jesse Craft is very easygoing person. He inspected the cavity surface and taught how the cavity inspection is performed.

John Schwartz is very friendly and he let borrow RF power couplers when I needed them for the movable coupler calibration.

Vladimir Zelevinsky is the genius. His way of explaining physics is very interesting.

Scott Bogner is a smart teacher. I learned a lot from him on quantum mechanics. He was always willing to help me to understand the mathematics behind quantum mechanics.

Martin Berz is my favorite professor in graduate school. His way of introducing physics concepts is very interesting and it raises intriguing fundamental questions. To me, his way of teaching is very powerful.

TABLE OF CONTENTS

LIST OF TABLES

LIST OF FIGURES

1 Introduction

1.1 Motivation

High frequency superconducting RF (SRF) structures are attractive for a variety of reasons. They make the accelerator very compact since the cross-section of the cavity is proportional to the inverse of the frequency squared, i.e. the higher radio frequency the smaller cavity becomes. Figure 1.1 shows elliptical SRF cavities for different frequencies [1]. That would also, scale down the other components of the accelerator such as the helium vessel, shielding, and vacuum chamber, i.e. less material use. In addition, smaller size cavities with a frequency up to 3 GHz are easier to handle, machine and process. Higher frequency provides a higher accelerating electric field. Moreover, a smaller cavity is less probable to have surface defects from cavity processing point of view. For these reasons, 1300 MHz (L-band) SRF cryomodule system was intensively studied and developed for the International Linear Collider (ILC). It is thus a mature technology and this technology is being implemented in the Linac Coherent Light Source (LCLS-II) project in the U.S. Recently established nitrogen doping technology can push up the intrinsic quality, $Q_0 > 2.7 \times 10^{10}$ at 16 MV/m (operation gradient). Although, the SRF cavity surface resistance is proportional to frequency squared, it can be minimized via doping technology. That reduces cavity's cryogenic heat load significantly. In addition, cavity doping technology has shown the trend that its reduction in cavity surface resistance is more pronounced in higher frequency cavities as shown in figure 1.2 [1]. With that in mind, we are investigating the possibility of 1288 MHz elliptical cavities for medium-beta heavy ion multi-charge-state beams. To take these benefits as well as a possible cost reduction for future medium-beta heavy-ion multi-charge-state

accelerators. However, the longitudinal acceptance of the operating frequency must be sufficiently large in order to minimize beam losses for accelerator hands-on maintenance. A simple analytic study was performed and the result showed that the 1288 MHz cavity is sufficient for medium-beta heavy ion accelerators [2]. In addition, from beam losses point of view, the study deduced that the operating frequency of 1288 MHz (L-band) could be the limit in the frequency for medium-beta heavy ion multi-charge-state beam accelerators. This work is an investigation of the possibility of high efficiency 1288 MHz SRF cavity for medium-beta heavy ion multi-charge-state beams. The detail beam simulation using TRACK code [3] to confirm the analytic result. The result shows that the longitudinal acceptance is sufficiently large for medium-beta heavy ion beams with five charge states. We can take these benefits of a high frequency (1288 MHz) cavity for future heavy ion SRF linacs.

Figure 1.1: SRF elliptical cavities for different frequencies. Image Credit: Martina Martinello, Fermilab.

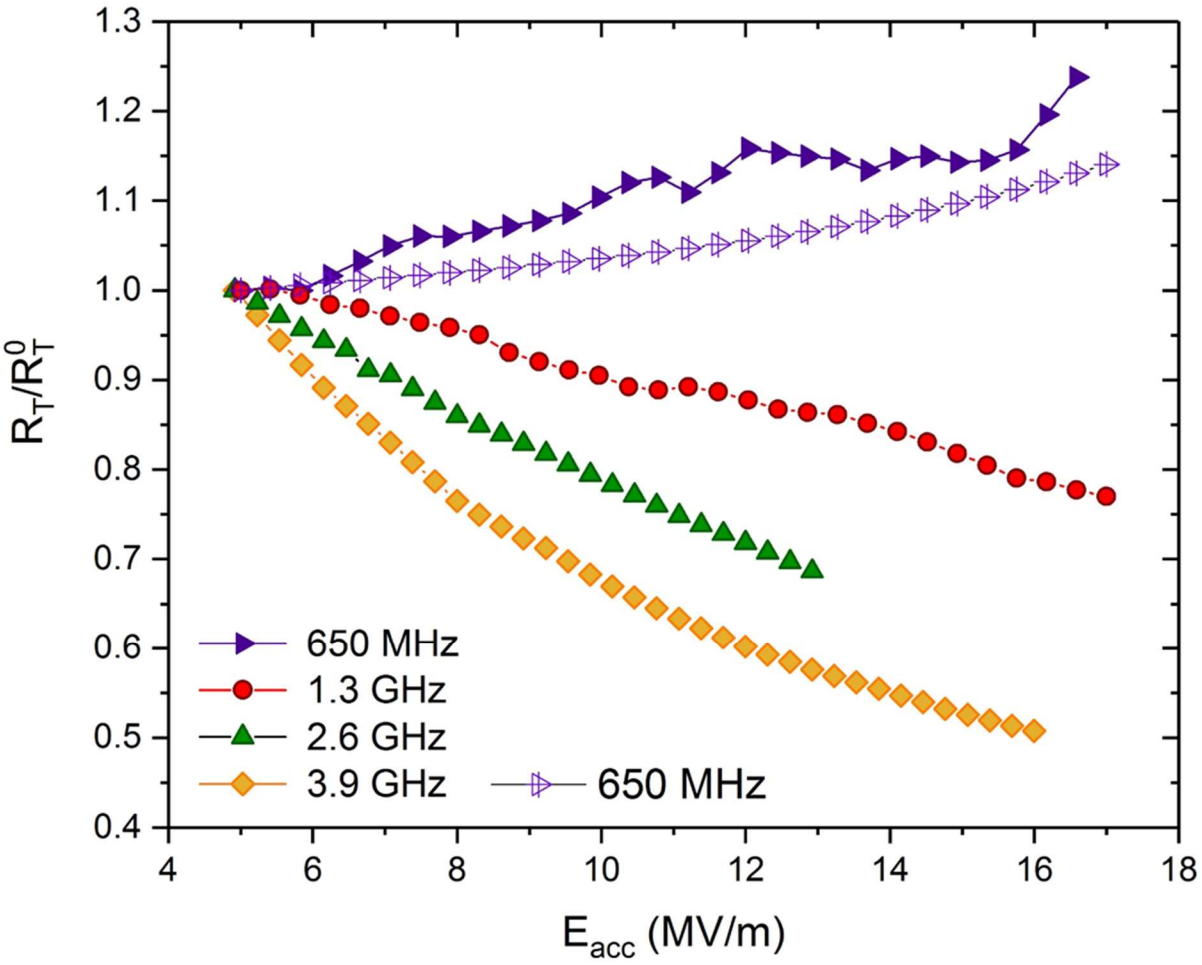

Figure 1.2: Normalized SRF cavity resistance versus accelerating electric field E_{acc} for different cavity frequencies. Plot Credit: Martina Martinello, Fermilab.

1.2 History of SRF technology

The first superconducting accelerating RF resonator was a lead (superconductor type I) electroplated cavity. W. Fairbank, A. Schwettman, and P. Wilson at Stanford University realized it in 1964, three years after W. Fairbank's proposal for a superconducting accelerator. This cavity was the first SRF application to electron accelerator. In 1970, J. Turneaure and N. Viet developed an 8.5 GHz SRF pillbox cavity made of niobium (superconductor type II). This cavity achieved a peak surface electric field of E_{pk} = 70

MV/m, a peak magnetic field of B_{pk} = 108 mT and a high intrinsic quality factor of Q_0 = 8 x10^9 at 1.25 K, which was very encouraging as a proof-of-principle for high accelerating electric field and high efficiency cavity. That led to the design and construction of the Superconducting Accelerator (SCA) at Stanford University in 1970s. SCA utilized SRF standing-wave elliptical accelerating cavities [4]. The elliptical shape of the cavity is advantageous because it suppresses the multipacting phenomenon in SRF cavities. The multipacting phenomenon can be explained as the multiple impact on cavity surface by the ejected electron from the surface due to the high magnetic field, which would lead to degradation in the cavity efficiency because part of the cavity energy would be spent to these ejected electrons. An elliptical cavity shape would make the ejected electrons hit different points on the cavity surface and eventually reside at the cavity equator at the low magnetic field region. In addition, the elliptical shape facilitates cavity preparations such as high purity niobium, cavity shape, cleanroom technology, chemical treatments and High-Pressure water Rinsing HPR to reduce particle contamination and result in high accelerating electric fields and high intrinsic quality factors. Figure 1.3 shows the history of cavity's performance improvement progress to develop a high gradient cavity in the past 4 decades. It shows the breakthroughs toward a high accelerating gradient cavity from the selection of the proper material of cavity, cavity processing and optimum cavity shape until it reached the limitation of the superconductivity critical magnetic field. Since then, the development and construction of SRF accelerators continued. Many SRF accelerators were built around the world for numerus projects and are being planned for future accelerators as well. One of the main advantages of SRF technology is that it enables a Continuous-Wave (CW) operation for high power accelerator.

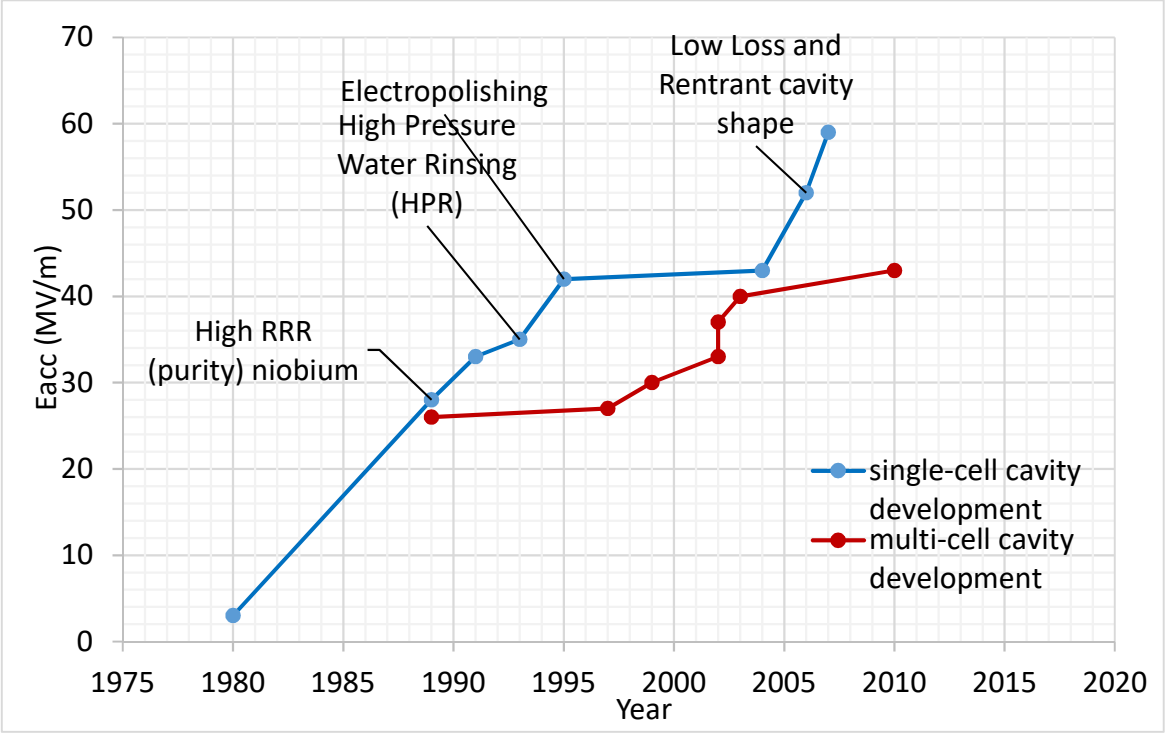

Figure 1.3: SRF cavity development in the past 4 decades for high cavity gradient.

2 The theory of accelerating radio frequency cavity

2.1 Lorentz force, Maxwell equations and wave equation

In the electromagnetism theory, if a charged particle, $\boldsymbol{q}$ moving with a velocity, $\vec{\boldsymbol{v}}$ in an electric field, $\vec{\boldsymbol{E}}$, then it will experience an electric force (acceleration) in the direction of the field. When it moves in a magnetic field, $\vec{\boldsymbol{B}}$ it will experience a magnetic force (change direction) perpendicular to the velocity vector and the applied magnetic field as described by Lorentz force equation (2.1).

$$\vec{\boldsymbol{F}} = \frac{d\vec{\boldsymbol{p}}}{\boldsymbol{dt}} = \boldsymbol{q}\left(\vec{\boldsymbol{E}} + \vec{\boldsymbol{v}} \times \vec{\boldsymbol{B}}\right) \tag{2.1}$$

To make use of Lorentz force equation, we introduce Maxwell equations, which govern the electromagnetic waves with the proper boundary conditions. The equation (2.2) says there is no electric charge source. The equation (2.3) says the change in the magnetic field, induces an electric field that curls around the magnetic field lines. The equation (2.4) says that is no magnetic field monopole source. The equation (2.5) says that the change in the electric field induces a magnetic field that curls around the electric field lines with the assumption that there is no current source. With the proper electric and magnetic boundary conditions on conductor surfaces, one can construct an electromagnetic energy tank (cavity) such that its energy can be used to accelerate or deflect particles depending on the purpose.

Maxwell equations in vacuum with no source (no electric charge):

$$\boldsymbol{\nabla} \cdot \vec{\boldsymbol{E}} = \boldsymbol{0}, \text{ (Gauss's Law)} \tag{2.2}$$

$$\boldsymbol{\nabla} \times \vec{\boldsymbol{E}} = -\frac{\boldsymbol{d}\vec{\boldsymbol{B}}}{\boldsymbol{dt}}, \text{ (Faraday's Law)} \tag{2.3}$$

$\boldsymbol{\nabla \cdot \vec{B} = 0}$, (Gauss's Law) (2.4)

$\boldsymbol{\nabla \times \vec{B} = \mu_0 \vec{J} + \frac{1}{c^2}\frac{d}{dt}\vec{E}}$, (Ampere's Law) (2.5)

Let us consider the interface between vacuum and a conductor as the electromagnetic fields inter from the vacuum to a conductor. For a perfect conductor (infinite conductivity), the boundary conditions of electric and magnetic fields can be expressed as the following:

1. The tangential component of the electric field of the conductor, $\boldsymbol{E_{t1}}$ is continuous at the conductor surface. This means, the tangential component of the conductor of the electric field, $\boldsymbol{E_{t1}}$ is equal to tangential component of the vacuum of the electric field, $\boldsymbol{E_{t2}}$ at the interface, i.e. $\boldsymbol{E_{t1} = E_{t2} = 0}$.
2. The normal component of the electric field of the conductor, $\boldsymbol{E_{n1}}$ is equal to the normal component of the electric field of the conductor, $\boldsymbol{E_{n2}}$. That means the electric field is orthogonal to the conductor surface. $\boldsymbol{E_{n1} = E_{n2}}$.
3. The tangential component of the magnetic field of the conductor, $\boldsymbol{B_{t1}}$ is equal to the tangential component of the vacuum of the magnetic field, $\boldsymbol{B_{t2}}$ at the interface, i.e. $\boldsymbol{B_{t1} = B_{t2}}$. This means the magnetic field is parallel to the conductor surface.
4. The tangential component of the magnetic field of the conductor, $\boldsymbol{B_{t1}}$ is continuous at the conductor surface. This means, the conductor tangential component of the magnetic field, $\boldsymbol{B_{t1}}$ is equal to vacuum tangential component of the magnetic field, $\boldsymbol{B_{t2}}$ at the interface, i.e. $\boldsymbol{B_{t1} = B_{t2} = 0}$.

If we take the curl of the equation (2.3) we get,

$$\boldsymbol{\nabla \times \nabla \times \vec{E} = -\nabla \times \frac{d\vec{B}}{dt}}$$

Using the identity $\boldsymbol{\nabla \times \nabla \times \vec{E} = \nabla(\nabla \cdot \vec{E}) - \nabla^2 \vec{E}}$

Then we obtain,

$$\boldsymbol{\nabla}\left(\boldsymbol{\nabla}\cdot\vec{\boldsymbol{E}}\right)-\ \boldsymbol{\nabla}^{\boldsymbol{2}}\vec{\boldsymbol{E}}=\ -\boldsymbol{\nabla}\times\frac{\boldsymbol{d}\vec{\boldsymbol{B}}}{\boldsymbol{dt}} \tag{2.6}$$

Then take the $\frac{\boldsymbol{d}}{\boldsymbol{dt}}$ of equation (2.5) and since there is not current source, i.e. $\vec{\boldsymbol{J}}=\mathbf{0}$,

$$\frac{\boldsymbol{d}}{\boldsymbol{dt}}(\boldsymbol{\nabla}\times\vec{\boldsymbol{B}})=\frac{\boldsymbol{d}}{\boldsymbol{dt}}\frac{\mathbf{1}}{\boldsymbol{c}^{\boldsymbol{2}}}\frac{\boldsymbol{d}}{\boldsymbol{dt}}\vec{\boldsymbol{E}}$$

$$\boldsymbol{\nabla}^{\boldsymbol{2}}\vec{\boldsymbol{E}}=\boldsymbol{\mu\varepsilon}\frac{\boldsymbol{d}^{\boldsymbol{2}}}{\boldsymbol{dt}^{\boldsymbol{2}}}\ \vec{\boldsymbol{E}} \tag{2.7}$$

Similarly, we can obtain similar results for the magnetic field,

$$\boldsymbol{\nabla}^{\boldsymbol{2}}\vec{\boldsymbol{B}}=\boldsymbol{\mu\varepsilon}\frac{\boldsymbol{d}^{\boldsymbol{2}}}{\boldsymbol{dt}^{\boldsymbol{2}}}\ \vec{\boldsymbol{B}} \tag{2.8}$$

For a compact form, we can write equation (2.7) and (2.8) as follows:

$$(\boldsymbol{\nabla}^{\boldsymbol{2}}-\ \boldsymbol{\mu\varepsilon}\frac{\boldsymbol{d}^{\boldsymbol{2}}}{\boldsymbol{dt}^{\boldsymbol{2}}})\begin{pmatrix}\vec{\boldsymbol{E}}(\vec{\boldsymbol{r}},\boldsymbol{t})\\ \vec{\boldsymbol{B}}(\vec{\boldsymbol{r}},\boldsymbol{t})\end{pmatrix}=0,\ \text{(The Wave Equation)} \tag{2.9}$$

The equation (2.9) is called the Wave Equation, which describes the electromagnetic wave.

The solution of the equation (2.9) is a plane wave. The electric field component of the plane wave can be expressed as in equation (2.10). The magnetic field component of the plane wave can be expressed as in equation (2.11).

$$\vec{\boldsymbol{E}}(\vec{\boldsymbol{r}},\boldsymbol{t})=\ \vec{\boldsymbol{E}}_{\mathbf{0}}(\vec{\boldsymbol{k}}\cdot\vec{\boldsymbol{r}}-\boldsymbol{\omega t}) \tag{2.10}$$

$$\vec{\boldsymbol{B}}(\vec{\boldsymbol{r}},\boldsymbol{t})=\ \vec{\boldsymbol{B}}_{\mathbf{0}}(\vec{\boldsymbol{k}}\cdot\vec{\boldsymbol{r}}-\boldsymbol{\omega t}+\boldsymbol{\varphi}) \tag{2.11}$$

Here $\vec{k}$ is the wave vector of the wave propagation and φ phase difference between the electric and magnetic fields. These equations, (2.10) and (2.11) must satisfy Maxwell equations.

This plane wave can be exploited with the proper boundary conditions to construct a resonant structure (standing wave structure). This resonant structure can be represented as a parallel LCR circuit as illustrated in figure 2.1. The impedance, Z of this circuit can be described by the equation (2.12), where R is the resistance, L is the inductance, C is the capacitance, and ω is the frequency of the electric current source.

$$Z = \frac{1}{\left[\frac{1}{R}+\frac{1}{iL\omega}+iC\omega\right]} \tag{2.12}$$

The resonant frequency, ω_0 of this circuit is expressed in equation (2.13),

$$\omega_0 = \frac{1}{\sqrt{LC}} \tag{2.13}$$

The stored energy in the capacitor, U_c of this circuit is expressed in equation (2.14)

$$U_c = \frac{CV^2}{2} \tag{2.14}$$

Here V, is the power source voltage.

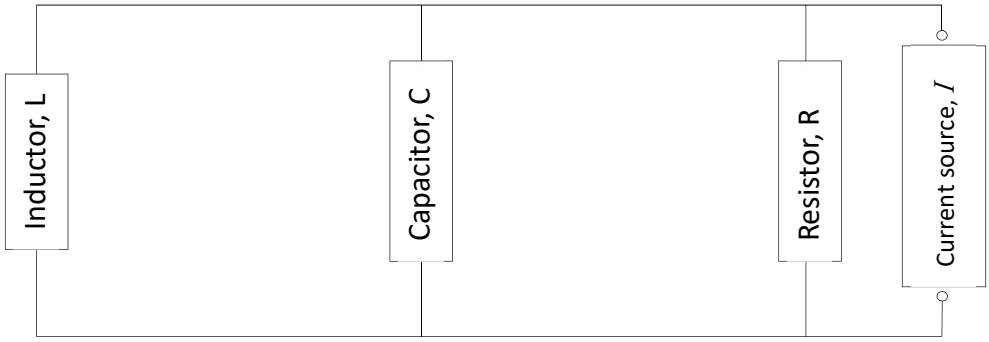

Figure 2.1: Parallel LCR resonant circuit schematics.

The equivalence here of LCR circuit to the resonant structure (cavity) is the following:

1. The inductance, L that stores the magnetic field is equivalent to cavity inner walls.
2. The capacitance, C that stores the electric field is equivalent to cavity ends.
3. The resistance, R of the circuit is equivalent to the resistance of the surface current of the resonant structure (cavity).

2.2 Pillbox cavity

Pillbox cavity is simply a hollow cylindrical resonant structure that stores the electromagnetic energy in a standing wave form that is subject to the conductor electromagnetic fields boundary conditions:

1. Zero tangential electric field component on the conductor wall surfaces, i.e. $\boldsymbol{n} \times \vec{\boldsymbol{E}} = \boldsymbol{0}$.
2. Zero orthogonal magnetic field component on the conductor wall surfaces, i.e. $\boldsymbol{n} \cdot \vec{\boldsymbol{E}} = \boldsymbol{0}$.

The general solution of the electric field can be expressed in terms of a longitudinal (parallel along the z-axis) field component, $\boldsymbol{E_l}$ and a transverse field component $\boldsymbol{E_t}$ as described by equation (2.15). Similarly, the general solution of magnetic field can be expressed as in equation (2.16) see reference [5].

$$\vec{\boldsymbol{E}} = \boldsymbol{E_l} + \boldsymbol{E_t} \tag{2.15}$$

$$\vec{\boldsymbol{B}} = \boldsymbol{B_l} + \boldsymbol{B_t} \tag{2.16}$$

The transverse component of the electric field, $\boldsymbol{E_t}$ can be written as in equation (2.17).

$$\boldsymbol{E_t} = \frac{\mathbf{1}}{(\mu\varepsilon\frac{\omega^2}{c^2} - \boldsymbol{k^2})}\left[\boldsymbol{\nabla_t}\left(\frac{\boldsymbol{dE_l}}{\boldsymbol{dz}}\right) - \boldsymbol{i}\frac{\boldsymbol{\omega}}{\boldsymbol{c}}\hat{\boldsymbol{e}}_{\boldsymbol{z}} \times \boldsymbol{\nabla_t B_l}\right] \tag{2.17}$$

The transverse component of the magnetic field, $\boldsymbol{B_t}$ can be written as in equation (2.18).

$$\boldsymbol{B_t} = \frac{\mathbf{1}}{(\mu\varepsilon\frac{\omega^2}{c^2} - \boldsymbol{k^2})}\left[\boldsymbol{\nabla_t}\left(\frac{\boldsymbol{dB_l}}{\boldsymbol{dz}}\right) + \boldsymbol{i\mu\varepsilon}\frac{\boldsymbol{\omega}}{\boldsymbol{c}}\hat{\boldsymbol{e}} \times \boldsymbol{\nabla_t E_l}\right] \tag{2.18}$$

Two sets of solutions can be obtained from equation (2.9) with infinite Eigen modes:

2.2.1 Transverse Magnetic field (TM)

This set of modes is for longitudinal electric fields and zero transverse electric fields. The solutions of the electric fields and the magnetic fields in the pillbox cavity can be described in cylindrical coordinates, which were taken from the reference [6] as follows:

$$\boldsymbol{E_z} = \boldsymbol{E_0}\mathbf{cos}\left(\frac{\boldsymbol{p\pi z}}{\boldsymbol{L}}\right)\boldsymbol{J_m}\left(\frac{\boldsymbol{x_{mn}r}}{\boldsymbol{R}}\right)\mathbf{cos}(\boldsymbol{m}\emptyset),$$

$$\boldsymbol{E_r} = -\boldsymbol{E_0}\frac{\boldsymbol{p\pi R}}{\boldsymbol{Lx_{mn}}}\mathbf{sin}\left(\frac{\boldsymbol{p\pi z}}{\boldsymbol{L}}\right)\boldsymbol{J'_m}\left(\frac{\boldsymbol{x_{mn}r}}{\boldsymbol{R}}\right)\mathbf{cos}(\boldsymbol{m}\emptyset),$$

$$\boldsymbol{E_\emptyset} = \boldsymbol{E_0}\frac{\boldsymbol{pxR^2}}{\boldsymbol{rLx_{mn}^2}}\mathbf{sin}\left(\frac{\boldsymbol{p\pi z}}{\boldsymbol{L}}\right)\boldsymbol{J_m}\left(\frac{\boldsymbol{x_{mn}r}}{\boldsymbol{R}}\right)\mathbf{sin}(\boldsymbol{m}\emptyset),$$

$$\boldsymbol{H_z} = \mathbf{0},$$

$$\boldsymbol{H_r} = \boldsymbol{iE_0}\frac{\boldsymbol{m\omega R^2}}{\boldsymbol{c}\sqrt{\frac{\mu_0}{\varepsilon_0}}\boldsymbol{rx_{mn}^2}}\mathbf{cos}\left(\frac{\boldsymbol{p\pi z}}{\boldsymbol{L}}\right)\boldsymbol{J_m}\left(\frac{\boldsymbol{x_{mn}r}}{\boldsymbol{R}}\right)\mathbf{sin}(\boldsymbol{m}\emptyset),$$

$$\boldsymbol{H_\emptyset} = \boldsymbol{iE_0}\frac{\boldsymbol{\omega R}}{\boldsymbol{c}\sqrt{\frac{\mu_0}{\varepsilon_0}}\boldsymbol{x_{mn}}}\mathbf{cos}\left(\frac{\boldsymbol{p\pi z}}{\boldsymbol{L}}\right)\boldsymbol{J'_m}\left(\frac{\boldsymbol{x_{mn}r}}{\boldsymbol{R}}\right)\mathbf{cos}(\boldsymbol{m}\emptyset),$$

Here, L is the cavity length, R is the cavity radius, $\boldsymbol{J_m}$ are the m[th] Bessel functions of the first kind, $\boldsymbol{x_{mn}}$ is the n[th] root of $\boldsymbol{J_m}$, and $\boldsymbol{J'_m}$ are the derivative of Bessel functions.

The resonant frequency of the TM Eigen modes solution can be described by the equation (2.19). The cavity radius is determined by the cavity frequency and the cavity length is determined by the mode of acceleration (determines the RF phase change between cavity cells).

$$\boldsymbol{\omega_{TM_{mnp}} = c\sqrt{\frac{x_{mn}^2}{R^2} + \frac{p^2\pi^2}{L^2}}} \qquad (2.19)$$

Here, $\boldsymbol{x_{mn}}$ is the $\boldsymbol{n}^{\text{th}}$ root of $\boldsymbol{J_m}$, $\boldsymbol{m}$ is an integer number of nodes of the field in the azimuthal direction $\emptyset$, $\boldsymbol{m = 0, 1, 2, 3}$ ... $\boldsymbol{n}$ is an integer number of nodes of the field in the radial direction $\boldsymbol{r}$, $\boldsymbol{n = 1, 2, 3}$ ... and $\boldsymbol{p}$ is an integer number of nodes of the field in the z–axis direction , $\boldsymbol{p = 0, 1, 2, 3}$ ... This mode is used for particle acceleration.

2.2.2 Transverse Electric field (TE)

This set of modes is for transverse electric fields and zero longitudinal electric fields. The solutions of the electric fields and the magnetic fields in the pillbox cavity obtained in cylindrical coordinates, which were taken from the reference [6] as follows:

$$\boldsymbol{E_z = 0},$$

$$\boldsymbol{E_r = iH_0 \frac{m\omega\sqrt{\frac{\mu_0}{\varepsilon_0}}R^2}{crx'^2_{mn}} \sin\left(\frac{p\pi z}{L}\right) J_m\left(\frac{x'_{mn}r}{R}\right) \sin(m\emptyset)},$$

$$\boldsymbol{E_\emptyset = iH_0 \frac{\omega\sqrt{\frac{\mu_0}{\varepsilon_0}}R}{cx'_{mn}} \sin\left(\frac{p\pi z}{L}\right) J'_m\left(\frac{x'_{mn}r}{R}\right) \cos(m\emptyset)},$$

$$H_z = H_0 \sin\left(\frac{p\pi z}{L}\right) J_m\left(\frac{x'_{mn} r}{R}\right) \cos(m\emptyset),$$

$$H_r = H_0 \frac{p\pi R}{L x'_{mn}} \cos\left(\frac{p\pi z}{L}\right) J'_m\left(\frac{x'_{mn} r}{R}\right) \cos(m\emptyset),$$

$$H_\emptyset = -H_0 \frac{mp\pi R^2}{rLx'^2_{mn}} \cos\left(\frac{p\pi z}{L}\right) J_m\left(\frac{x'_{mn} r}{R}\right) \sin(m\emptyset),$$

The resonant frequency of the TE Eigen modes solution can be described by the equation (2.20) [5].

$$\omega_{TE_{mnp}} = c\sqrt{\frac{x'^2_{mn}}{R^2} + \frac{p^2\pi^2}{L^2}} \qquad (2.20)$$

For purely longitudinal accelerating electric field, TM_{010} mode is used. The electric fields and magnetic fields solutions become:

$E_z = E_0 J_0\left(\frac{x_{01} r}{R}\right)$, here x_{01} is equal to 2.405.

$$E_r = 0,$$

$$E_\emptyset = 0,$$

$$H_z = 0,$$

$$H_r = 0,$$

$$H_\emptyset = -i\omega\varepsilon E_0 \frac{R}{x_{01}} J_1\left(\frac{x_{01} r}{R}\right),$$

The resonant frequency of the TM_{010} can expressed as in equation (2.21),

$$\omega_{010} = \frac{2.405c}{R} \qquad (2.21)$$

Then the equation (2.21) implies that the cavity radius, inversely proportional to the resonant frequency. That tells us that higher frequency cavities are more compact, i.e. less material use from linac structure point of view.

The figure 2.2 shows a pillbox cavity design was made via CST Suite Studio [7] and the cavity TM_{010} Mode magnetic fields and electric fields distribution. The length of cavity, L can be expressed as in equation (2.22).

$$\boldsymbol{L = \frac{\beta_g \lambda}{2}} \tag{2.22}$$

Here, $\boldsymbol{\beta_g}$ is the cavity beta geometry, which determines the cavity length along with the wavelength, $\boldsymbol{\lambda}$ of cavity resonant frequency.

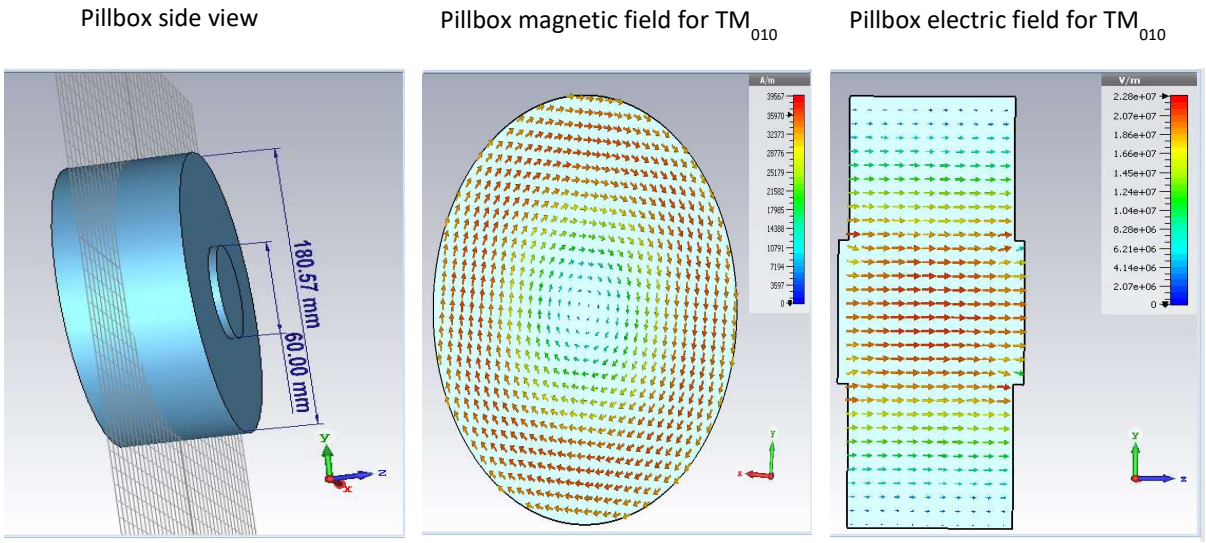

Figure 2.2: Pillbox cavity (mid-cell) designed on CST Suite Studio for 1288 MHz resonant frequency with beta geometry of 0.61. The magnetic fields and the electric fields shown for the cavity cross-sections.

The cavity accelerating voltage, $\boldsymbol{V_{acc}}$ is the integral of the electric field along the cavity length at the center and considering the variation of the field over time. $\boldsymbol{V_{acc}}$ is defined in equation (2.23).

$$\boldsymbol{V_{acc} = \int_{-\infty}^{\infty} E_z(r = 0, z) e^{\frac{i\omega_0 z}{\beta c}} dz} \tag{2.23}$$

$\boldsymbol{V_{acc}}$ for pillbox cavity:

$$\boldsymbol{V_{acc} = \int_{0}^{L} E_z(r = 0, z) e^{\frac{i\omega_0 z}{\beta c}} dz = E_0 T L}$$

Where $\boldsymbol{E_0}$ is the electric field strength at DC, T is the transit time factor which is defined as the reduction in the energy gain due to the time varying electric field, it is also defined as the of the cavity voltage gain of RF wave over cavity energy gain in DC is described in equation (2.24).

$$\boldsymbol{T = \frac{\int_{-\infty}^{\infty} E_z e^{\frac{i\omega_0 z}{\beta c}} dz}{\int_{-\infty}^{\infty} |E_z| dz}} \tag{2.24}$$

The parameters of this cavity were chosen to be suitable for the proposed medium beta multi-charge-state linac. The accelerating mode of the cavity is π-mode. The π-mode means the RF wave phase shift is 180 degrees between cavity-cells for particle synchronicity with the RF wave when it passes through the cavity cells as shown in figure 2.3.

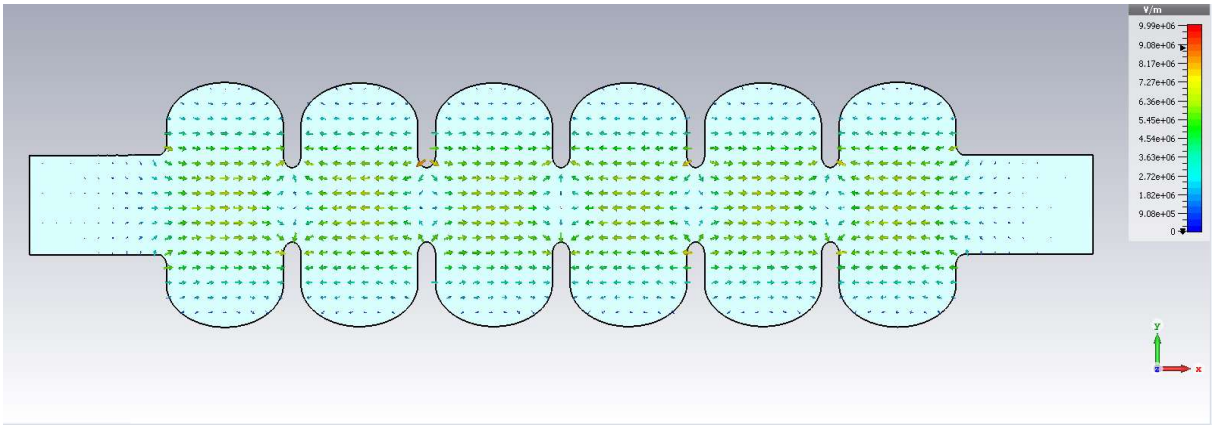

Figure 2.3: π -mode 6-cell cavity accelerating electric field profile.

For a multi-cell cavity, the transit time factor, $\boldsymbol{T}$ can be obtained by the equation (2.25) for an even number of cells and the equation (2.26) for an odd number of cells [8].

$$\boldsymbol{T} = \left(\frac{\boldsymbol{\beta}}{\boldsymbol{\beta_g}}\right)^{\boldsymbol{2}} \boldsymbol{sin}\left(\frac{\boldsymbol{\pi N}}{\boldsymbol{2\beta/\beta_g}}\right) \frac{\boldsymbol{(-1)^{(N+2)/2}}}{\boldsymbol{N((\beta/\beta_g)^2-1)}} \tag{2.25}$$

$$\boldsymbol{T} = \left(\frac{\boldsymbol{\beta}}{\boldsymbol{\beta_g}}\right)^{\boldsymbol{2}} \boldsymbol{cos}\left(\frac{\boldsymbol{\pi N}}{\boldsymbol{2\beta/\beta_g}}\right) \frac{\boldsymbol{(-1)^{(N-1)/2}}}{\boldsymbol{N((\beta/\beta_g)^2-1)}} \tag{2.26}$$

Here, N is the number of cavity-cells, β is the particle velocity and $\boldsymbol{\beta_g}$ is the cavity beta geometry.

The accelerating field, $\boldsymbol{E_{acc}}$ (gradient) of the cavity is defined as the cavity voltage, $\boldsymbol{V_{acc}}$ over the cavity length, L as seen in equation (2.27).

$$\boldsymbol{E_{acc}} = \frac{\boldsymbol{V_{acc}}}{\boldsymbol{L}} \tag{2.27}$$

Since the total stored energy density in the electromagnetic field is defined as the sum of the stored energy in the electric field and in magnetic field as descried in equation (2.28).

$$\boldsymbol{u = \frac{1}{2}\int\left(\varepsilon_0 \vec{E}^2 + \mu_0 \vec{H}^2\right) dv} \quad (2.28)$$

Since the energy oscillates between the magnetic field and the electric field sinusoidally with a phase shift of $\mathbf{90}^{\circ}$ then one can use either the electric field or the magnetic field to obtain the total energy. The cavity is stored energy, $\boldsymbol{U}$ is defined as in equation (2.29).

$$\boldsymbol{U = \frac{\varepsilon_0}{2}\int_V \vec{E}^2 dv = \frac{\mu_0}{2}\int_V \vec{H}^2 dv} \quad (2.29)$$

2.3 Real cavity shape

In practice, the pillbox shape of the cavity is problematic from cavity efficiency and accelerating electric field strength points of views. As shown in figure 2.2 the magnetic fields are concentrated at the cavity outer walls, which can potentially eject electrons from the cavity surface and then make these ejected electrons hit the surface again. If the impact energy of the ejected electron is above the threshold of the Secondary Electron Yield (SEY), then that would lead to an avalanche of the secondary electrons emission and that degrades cavity performance. This is called multiple impact of electrons (multipacting). Figure 2.4 shows a pillbox cavity with multipacting. Thus, the peak surface magnetic fields, $\boldsymbol{B_{pk}}$ at cavity walls should be minimized. The convention is to minimize the ratio of the peak surface magnetic fields to the accelerating electric fields, $\frac{\boldsymbol{B_{pk}}}{\boldsymbol{E_{acc}}}$. The cavity shape is crucial in cavity performance. It would be advantageous if the cavity outer walls were modified in such a way that make the impacted electron hit other points, and then eventually reside at the cavity equator (lower magnetic field region). In addition, the cavity should not have sharp edges due to it can enhance the fields at the edge which causes electrons emission and that degrades cavity performance.

This electron emission is called field emission. Thus, cavity edges should be blended which lowers the peak surface electric field, $\boldsymbol{E_{pk}}$ as shown in figure 2.5. The convention is to minimize the ratio of the peak surface electric fields to the accelerating electric fields, $\frac{\boldsymbol{E_{pk}}}{\boldsymbol{E_{acc}}}$.

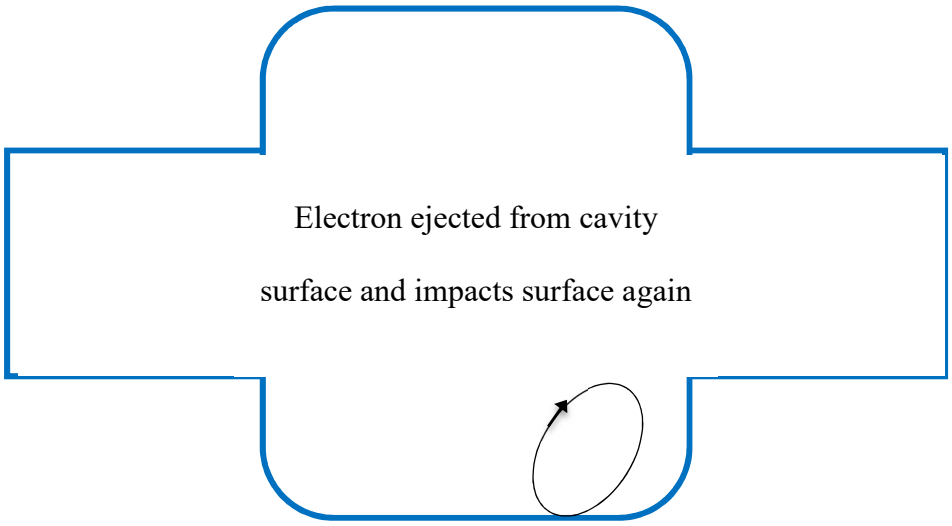

Figure 2.4: Pillbox cavity with multipacting.

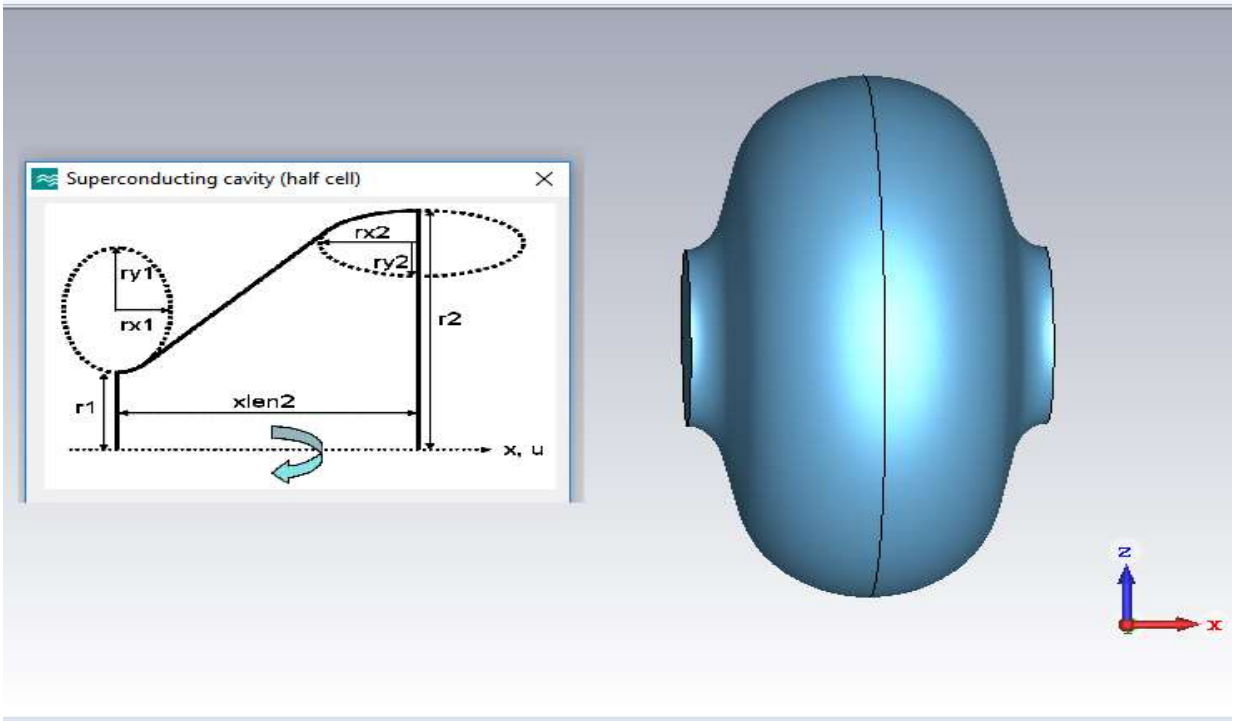

Figure 2.5: Real elliptical cavity design on CST Suite Studio.

2.4 Cavity parameters

2.4.1 Power dissipation

In SRF cavities, there is non-negligible power dissipation, $\boldsymbol{P_{loss}}$ on cavities walls due to surface resistance, $\boldsymbol{R_s}$. Although, the cavity is superconducting, there will still be power dissipation because the surface electric current is RF (oscillatory), which means that the electrons cannot synchronize with the RF wave because the electron has mass. That results lagging of electrons with the RF wave which does not screen all electric fields, i.e. normal conducting electrons will experience electric fields and that results power dissipation. The RF magnetic field penetrates the cavity (conductor) surface with a thin depth called the skin depth, $\boldsymbol{\delta}$. The majority of power is dissipated in this thin layer

skin depth due cavity surface current resulted from the change in the magnetic field of the RF wave. For a good conductor, the skin depth, $\boldsymbol{\delta}$ is calculated as in equation (2.30). The cavity surface resistance is calculated as in equation (2.31). The power dissipation on the cavity walls due to surface resistance can be expressed as the sum of square of the magnetic fields over the cavity surface multiplied by the cavity surface resistance as seen in equation (2.32). For a normal conducting cavity, the surface resistance is proportional to the square root of the cavity frequency. For a superconducting cavity, the surface resistance, $\boldsymbol{R_s}$ is proportional to the square of the frequency. In chapter 7, the SRF cavity surface resistance and the skin depth are discussed in more details.

$$\boldsymbol{\delta} = \sqrt{\frac{2}{\sigma\omega\mu_0}} \tag{2.30}$$

$$\boldsymbol{R_s} = \sqrt{\frac{\omega\mu_0}{2\sigma}} = \frac{\mathbf{1}}{\boldsymbol{\delta\sigma}} \tag{2.31}$$

$$\boldsymbol{P_{loss}} = \frac{\boldsymbol{R_s}}{\mathbf{2}} \int_A \left|\vec{\boldsymbol{H}}\right|^2 \boldsymbol{da} \tag{2.32}$$

2.4.2 Cavity intrinsic quality factor

The intrinsic quality factor, $\boldsymbol{Q_0}$ determines the cavity efficiency. It measures how efficient is the cavity in storing the electromagnetic energy. It is defined as the stored energy in cavity over power loss on cavity walls per radian as described in equation (2.33). It also, can be defined as the frequency times the volume integral of the magnetic field squared divided by the surface resistance times the surface integral of the magnetic field squared as described in equation (2.34).

$$\boldsymbol{Q_0} = \frac{\boldsymbol{\omega U}}{\boldsymbol{P_{loss}}} \tag{2.33}$$

$$\boldsymbol{Q_0 = \frac{\omega \mu_0}{R_s} \frac{\int_V |\vec{H}|^2 dv}{\int_A |\vec{H}|^2 da}} \quad (2.34)$$

2.4.3 Geometrical factor

The geometrical factor, $\boldsymbol{G}$ is defined as the frequency times the volume integral of the magnetic field squared divided by the surface resistance times the surface integral of the magnetic field squared as described in equation (2.35). It depends on cavity shape. It also can be defined as the cavity intrinsic quality factor multiplied by the cavity surface resistance. This parameter should to be maximized for higher efficiency cavity. It can be also defined as the cavity intrinsic quality factor and the surface resistance as expressed in equation (2.36).

$$\boldsymbol{G = \omega \mu_0 \frac{\int_V |\vec{H}|^2 dv}{\int_A |\vec{H}|^2 da} = Q_0 R_s} \quad (2.35)$$

$$\boldsymbol{G = Q_0 R_s} \quad (2.36)$$

2.4.4 Shunt impedance

Shunt impedance, $\boldsymbol{R_{sh}}$ determines how efficient the cavity in delivering the maximum acceleration is. It is also defined as the cavity voltage squared divided by the cavity power loss as illustrated in equation (2.37) and its unit is Ohm. It is an important cavity parameter and it should be maximized.

$$\boldsymbol{R_{sh} = \frac{V_{acc}^2}{P_{loss}}} \quad (2.37)$$

2.4.5 R/Q

R/Q is a measure of efficiency of the cavity in delivering the maximum acceleration per cavity stored energy as described in equation (2.38). This parameter does not depend on cavity material and it should be maximized for maximum cavity efficiency. It means how concentrated is the electric field (accelerating energy) on beam axis. It means also how cavity shape is good in delivering maximum

$$\frac{R}{Q} = \frac{V^2}{\omega U} \tag{2.38}$$

2.4.5 Cell to cell coupling

For a multi-cell cavity case, the cell-to-cell coupling, k_{cc} is a measure of the energy flow between neighboring cells of the cavity. It depends on the cavity aperture radius. The larger the cell aperture the more power flows to neighboring cavity-cells from the RF power source coupler. The cell-to-cell coupling, k_{cc} is a measure of the energy flow between neighboring cells of the cavity. This is an important cavity parameter for high current accelerating cavities. It is defined as the difference of the frequencies of π -mode (180 degrees phase shift between cells) and the 0-mode (zero phase shift between cells) divided by the average of the two frequencies as described by the equation (2.39). For a heavy ion linac, the beam current is low and it is in the order of (~mA) linac, thus a small cell-to-cell coupling is not an issue.

$$k_{cc} = \frac{\omega_\pi - \omega_0}{\frac{\omega_\pi + \omega_0}{2}} \tag{2.39}$$

3 The theory of focusing magnetic quadrupole

3.1 Principle of magnetic quadrupole focusing

According to Lorentz force equation (2.1) the magnetic field changes direction of charged particles, thus one can exploit this dynamic to focus particles along the linac. The magnetic quadrupole has four poles that focuses the beam in one plane while defocuses the beam in the other transverse plane. According to the right-hand rule of cross product of the velocity with the magnetic field in equation (2.1), if a positively charged particle moves into the page in a magnetic field region and the magnetic field direction is downward, then it will experience a force to the left. The principle of magnetic quadrupole focusing is very similar to lenses focusing rays in optics. The focal length strength of the lens is analogous to the strength of the magnetic field times its length. The magnetic quadrupole focusing relies on linear increase in the magnetic field as described in equations (3.1) and (3.2) where the z-axis is the beam direction [9].

$$\boldsymbol{B_y = g \cdot x} \tag{3.1}$$

$$\boldsymbol{B_x = g \cdot y} \tag{3.2}$$

Here, $\boldsymbol{g}$ is called the gradient of the magnetic quadrupole field. It is defined as the magnetic field over the radius, R of the path length as described in equation (3.3). $\boldsymbol{n}$ is the density of number of turns of the coil and $\boldsymbol{I}$ is the coil electric current.

$$\boldsymbol{g = \frac{2\mu_0 nI}{R^2}} \tag{3.3}$$

Then the focal length, $\boldsymbol{f}$ of the magnetic quadrupole is defined as in equation (3.4).

$$f = \frac{p}{egl} \tag{3.4}$$

Here, p is the particle momentum, e is the electron charge and l is the magnetic quadrupole length. To increase the focusing strength of the quadrupole, an iron yoke is utilized with high magnetic field saturation and relatively high magnetic permeability to strengthen the magnetic field in the gap (beam tube), i.e. it concentrates the field lines in the gap as shown in figure 3.1.

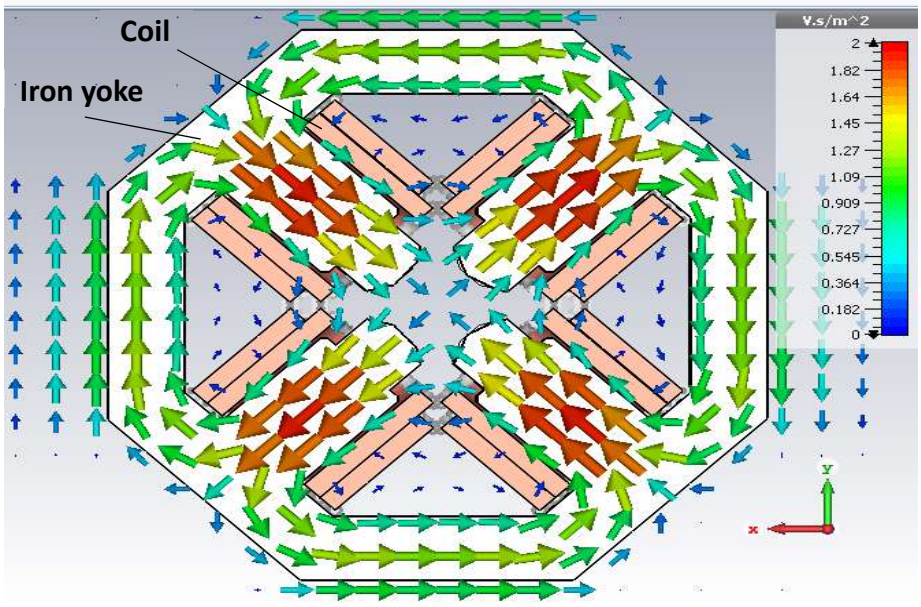

Figure 3.1: A magnetic quadrupole with iron yoke magnetic field profile on CST Suite Studio. Note: the magnetic poles were tilted by **45°** around the z-axis to align the focusing and the defocusing planes in the X (Horizontal) and Y (Vertical) axes respectively.

3.2 FODO lattice focusing

As we mentioned in section 3.1, the magnetic quadrupole focuses the beam in one transverse direction, while it defocuses the beam in the other transverse direction. Thus,

one can add another magnetic quadrupole to focus the defocused beam and defocuses the beam in the other transverse direction. With this method, one can maintain the beam in the beam line. This idea is the simplest method of beam focusing and it is called as a Focusing and Defocusing (FODO) cell. It means that two quadrupoles are placed at a distance from each other to focus the beam along the linac lattice. One quadrupole focuses the beam in one transverse direction and defocuses the beam in the other direction. Second quadrupole focuses the defocused beam direction and defocuses the focused beam in the other direction. The horizontal focusing and vertical defocusing quadrupole of the FODO cell can be represented as in matrices (3.1) and (3.2) respectively. The horizontal defocusing and vertical focusing quadrupole of the FODO cell can be represented as in matrices (3.3) and (3.4) respectively [9].

$$\boldsymbol{M_{xfocusing}} = \begin{pmatrix} \mathbf{cos}(\boldsymbol{l}\sqrt{\frac{\boldsymbol{g}}{\boldsymbol{B\rho}}}) & \frac{\mathbf{1}}{\sqrt{\boldsymbol{g}}}\mathbf{sin}(\boldsymbol{l}\sqrt{\frac{\boldsymbol{g}}{\boldsymbol{B\rho}}}) \\ -\sqrt{\frac{\boldsymbol{g}}{\boldsymbol{B\rho}}}\mathbf{sin}(\boldsymbol{l}\sqrt{\frac{\boldsymbol{g}}{\boldsymbol{B\rho}}}) & \mathbf{cos}(\boldsymbol{l}\sqrt{\frac{\boldsymbol{g}}{\boldsymbol{B\rho}}}) \end{pmatrix}, \text{for } \frac{\boldsymbol{g}}{\boldsymbol{B\rho}} > \mathbf{0} \tag{3.1}$$

$$\boldsymbol{M_{ydefocusing}} = \begin{pmatrix} \mathbf{cosh}(\boldsymbol{l}\sqrt{\frac{\boldsymbol{g}}{\boldsymbol{B\rho}}}) & \frac{\mathbf{1}}{\sqrt{\boldsymbol{g}}}\mathbf{sinh}(\boldsymbol{l}\sqrt{\frac{\boldsymbol{g}}{\boldsymbol{B\rho}}}) \\ -\sqrt{\frac{\boldsymbol{g}}{\boldsymbol{B\rho}}}\mathbf{sinh}(\boldsymbol{l}\sqrt{\frac{\boldsymbol{g}}{\boldsymbol{B\rho}}}) & \mathbf{cosh}(\boldsymbol{l}\sqrt{\frac{\boldsymbol{g}}{\boldsymbol{B\rho}}}) \end{pmatrix}, \text{for } \frac{\boldsymbol{g}}{\boldsymbol{B\rho}} > \mathbf{0} \tag{3.2}$$

$$\boldsymbol{M_{xdefocusing}} = \begin{pmatrix} \mathbf{cosh}(\boldsymbol{l}\sqrt{\frac{\boldsymbol{g}}{\boldsymbol{B\rho}}}) & \frac{\mathbf{1}}{\sqrt{\boldsymbol{g}}}\mathbf{sinh}(\boldsymbol{l}\sqrt{\frac{\boldsymbol{g}}{\boldsymbol{B\rho}}}) \\ -\sqrt{\frac{\boldsymbol{g}}{\boldsymbol{B\rho}}}\mathbf{sinh}(\boldsymbol{l}\sqrt{\frac{\boldsymbol{g}}{\boldsymbol{B\rho}}}) & \mathbf{cosh}(\boldsymbol{l}\sqrt{\frac{\boldsymbol{g}}{\boldsymbol{B\rho}}}) \end{pmatrix}, \text{for } \frac{\boldsymbol{g}}{\boldsymbol{B\rho}} < \mathbf{0} \tag{3.3}$$

$$\boldsymbol{M_{yfocusing}} = \begin{pmatrix} \boldsymbol{\cos(l\sqrt{\frac{g}{B\rho}})} & \boldsymbol{\frac{1}{\sqrt{g}}\sin(l\sqrt{\frac{g}{B\rho}})} \\ \boldsymbol{-\sqrt{\frac{g}{B\rho}}\sin(l\sqrt{\frac{g}{B\rho}})} & \boldsymbol{\cos(l\sqrt{\frac{g}{B\rho}})} \end{pmatrix}, \text{ for } \boldsymbol{\frac{g}{B\rho} < 0} \quad (3.4)$$

Here, in the matrix (3.1), $\boldsymbol{g}$ is the gradient of the magnetic quadrupole field, $\boldsymbol{B}$ is the magnetic field, and $\boldsymbol{\rho}$ is the magnetic rigidity.

4 Beam dynamics

4.1 Longitudinal dynamics

Conventionally, the longitudinal motion of the ion beam in a linac is defined in the z-axis direction and that is the direction of accelerating electric force in the linac. That means in this direction, the ion's energy will increase as it passes through the cavities, i.e. the ion velocity will change. Thus, it is convenient to describe the motion of the ions in terms of energy and position in the longitudinal phase-space. Since the electric field of the accelerating cavities is sinusoidal as illustrated in section 2.2.1, the cavity RF phase is synchronized with the reference ion (synchronous ion). The rise of the accelerating electric field will cause a focusing effect (restoring force) to the ions that have energy and position close to the synchronous ion in the RF wave. This is called synchronous oscillations. Let us consider a sinusoidal electric field as in figure 4.1, the synchronous phase, $\boldsymbol{\varphi_s}$ of the cavity is tuned to synchronous ion in the RF wave. The late ion will experience higher accelerating electric field than the synchronous ion, so it catches up with the synchronous ion and the early ion will experience lower accelerating electric field than the synchronous ion, so it will bunch closer to the synchronous ion. This makes the beam bunched in a single bunch. Here, we considered ions with only a single charge state ($\boldsymbol{q_1}$/e). This bunch has a centroid, which is the synchronous ion, a bunch length ($\Delta\boldsymbol{\varphi}$) and an energy of bunch ions deviation from the synchronous ion ($\Delta\boldsymbol{E}$). For convenience, the ions position in the z-axis can be converted to cavity phase as illustrated in equation (4.1).

$$(\boldsymbol{z - z_s}) = -\frac{\boldsymbol{\beta_s \lambda}}{\boldsymbol{2\pi}}(\boldsymbol{\varphi - \varphi_s}), \tag{4.1}$$

Here, $(\boldsymbol{z - z_s})$ is the deviation of an arbitrary ion from the synchronous ion in z-axis, $\boldsymbol{\beta_s}$ is the synchronous ion velocity, $\boldsymbol{\lambda}$ is the wavelength of the cavity frequency and $(\boldsymbol{\varphi - \varphi_s})$ is the deviation of an arbitrary ion phase from the synchronous ion phase.

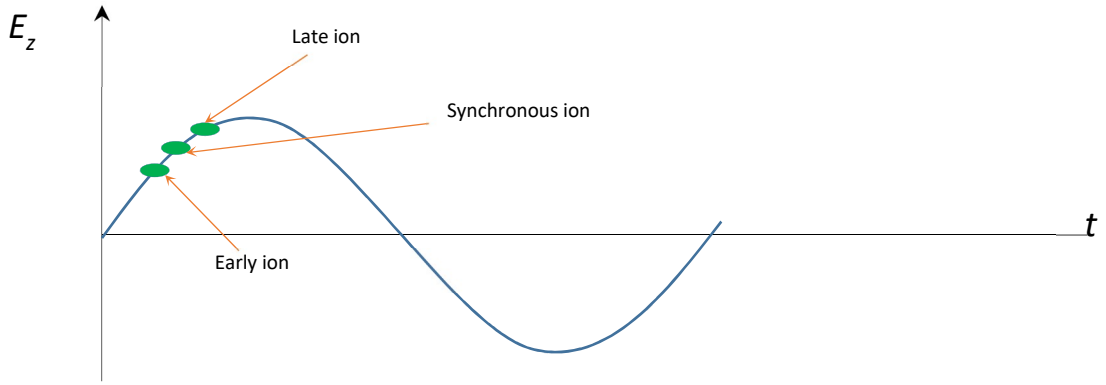

Figure 4.1: Cavity RF accelerating electric field plot illustrates the longitudinal dynamic of the ion bunch.

From the difference equations of an arbitrary ion phase to the synchronous ion phase and difference equations of an arbitrary ion's energy gain as it passes through cavities, one can write the longitudinal dynamic in terms continues of two coupled equations. The equation (4.2) describes the change of the ion phase with respect to the synchronous ion's phase for ions particular energies. The equation (4.3) describes the change of an arbitrary ion energy with respect to the synchronous ion's energy for ions with particular phase with the assumption that the rate of acceleration is small, i.e. small change in ion's velocity.

$$\frac{\boldsymbol{d(\varphi-\varphi_s)}}{\boldsymbol{ds}} = \boldsymbol{-2\pi \frac{(w-w_s)}{\gamma_s^3 \beta_s^3 mc^2 \lambda}}, \tag{4.2}$$

$$\frac{\boldsymbol{d(w-w_s)}}{\boldsymbol{ds}} = \boldsymbol{qE_0T(cos\varphi - cos\varphi_s)}, \tag{4.3}$$

Here, $(\boldsymbol{w-w_s})$ is the deviation of an arbitrary ion energy gain from the synchronous ion gain, ds is a differential of the axial distance along the accelerating direction and it is defined as $\boldsymbol{ds=\frac{\beta_s\lambda}{2}dn}$, $\boldsymbol{n}$ is the nth cell number. Simply, the discrete differential, $\boldsymbol{dn}$ is converted to a continues differential, $\boldsymbol{ds}$.

If we differentiate eqaution (4.2) then we obtain the eqaution (4.4),

$$\boldsymbol{\frac{d}{ds}\left[\frac{d(\varphi-\varphi_s)}{ds}\right]=\frac{d}{ds}\left[-2\pi\frac{(w-w_s)}{\gamma_s^3\beta_s^3mc^2\lambda}\right]}, \tag{4.4}$$

Then we subtitute equation (4.3) in equation (4.4).

We obtain a second order nonlinear differential equation (4.5) and it is very difficult to solve, unless we make some simplifcations as follows; the rate of acceleration is small and the parameters, $\boldsymbol{E_0, T\ and\ \varphi_s}$ are constant then the hamiltionion of the differential equation (4.5) can be written as in equation (4.6). This hamiltionion is constant under the law of converstion of energy in the longitudnal motion. In the hamiltionion equation (4.6), we can notice that the first term is the kinetic energy term and the second term is the potiential energy term [9].

$$\boldsymbol{\frac{d^2(\varphi-\varphi_s)}{d^2s}+\frac{3}{\gamma_s^2\beta_s^2}\left[\frac{d}{ds}(\gamma_s\beta_s\right]\left[\frac{d(\varphi-\varphi_s)}{ds}\right]+2\pi\frac{qE_0T}{\gamma_s^3\beta_s^3mc^2\lambda}(\cos\varphi-cos\varphi_s)=0}, \tag{4.5}$$

$$\boldsymbol{H_\emptyset=\frac{\pi(w-w_s)^2}{\gamma_s^3\beta_s^3\lambda(mc^3)^2}+\frac{qE_0T}{mc^2}(sin\varphi-\varphi cos\varphi_s)}, \tag{4.6}$$

The potential energy can be written as in equation (4.7).

$$\boldsymbol{U_\emptyset=\frac{qE_0T}{mc^2}(sin\varphi-\varphi cos\varphi_s)}, \tag{4.7}$$

4.2 Acceptance

The definition of acceptance is the area in the longitudinal phase-space at which the transported ion trajectory is in stable motion. From the sinusoidal nature of the cavity accelerating electric field as shown in figure 4.2.a, one can plot the cavity potential energy profile from equation (4.7) as shown in figure 4.2.b, we can identify a potential well in the stable phase region of $\boldsymbol{\varphi_2} < \boldsymbol{\varphi_s} < -\boldsymbol{\varphi_s}$. From the cavity potential energy plot in figure 4.2.a, we can identify the maximum potential well, which defines the stable region. The maximum potential well boundaries, is called the separatrix. The separatrix separates the stable region from the unstable one as shown in figure 4.2.c. In other words, if an ion is in the stable region, then its trajectory is a stable motion, i.e. the ion experiences a restoring force. If an ion is in the unstable region, then its trajectory is an unstable motion, i.e. there is not restoring force to make the ions oscillate around the synchronous ion, i.e. the ions would be eventually over or under focused and then they would hit the beam aperture and be considered lost. The separatrix has a maximum deviation energy width and a maximum phase width. These points can be obtained as follows: at the phase $-\boldsymbol{\varphi_s}$ and $\boldsymbol{\varphi_2}$ the energy width, $\boldsymbol{w = 0}$ and at the synchronous phase, $\boldsymbol{\varphi_s}$ the energy width is at maximum, $\boldsymbol{w_{max}}$. The longitudinal acceptance is defined as the area inside the separatrix, which can be expressed by $\boldsymbol{\pi . w_{max} . \varphi_{max}}$. It is estimated via the equation (4.8) for the maximum energy half width, $\boldsymbol{w_{max}}$ and the maximum phase width $\boldsymbol{\varphi_{max}}$ is determined via the sum of the two solutions the first one, when $\boldsymbol{w = 0}$, which gives us $\boldsymbol{\phi_1}$, i.e. $\boldsymbol{\varphi_1 = -\varphi_s}$ and the second one gives us $\boldsymbol{\varphi_2}$ as shown in equation (4.9). Often $\boldsymbol{\phi_2}$ is approximated to $\boldsymbol{\varphi_2 \approx 3\varphi_s}$. If we assume a small rate of acceleration, then the separatrix shape becomes fish as shown in the figure 4.2.b. However, if the rate of acceleration is large, then the separatrix shape becomes golf-club shape, which

reduces the stable region area by an amount. TRACK code was utilized to estimate the longitudinal acceptance as will see in chapter 6.2.2. In the appendix, the longitudinal acceptance calculations in TRACK code is explained.

$$\boldsymbol{w_{max}} = \frac{\boldsymbol{\Delta W_{max}}}{\boldsymbol{mc^2}} = \sqrt{(\boldsymbol{\varphi_s cos\varphi_s - sin\varphi_s})\frac{\boldsymbol{2qE_0 T\beta_s^3\gamma_s^3\lambda}}{\boldsymbol{\pi mc^2}}} \tag{4.8}$$

$$\boldsymbol{sin\varphi_2 - \varphi_2 cos\varphi_s = \varphi_s cos\varphi_s - sin\varphi_s} \tag{4.9}$$

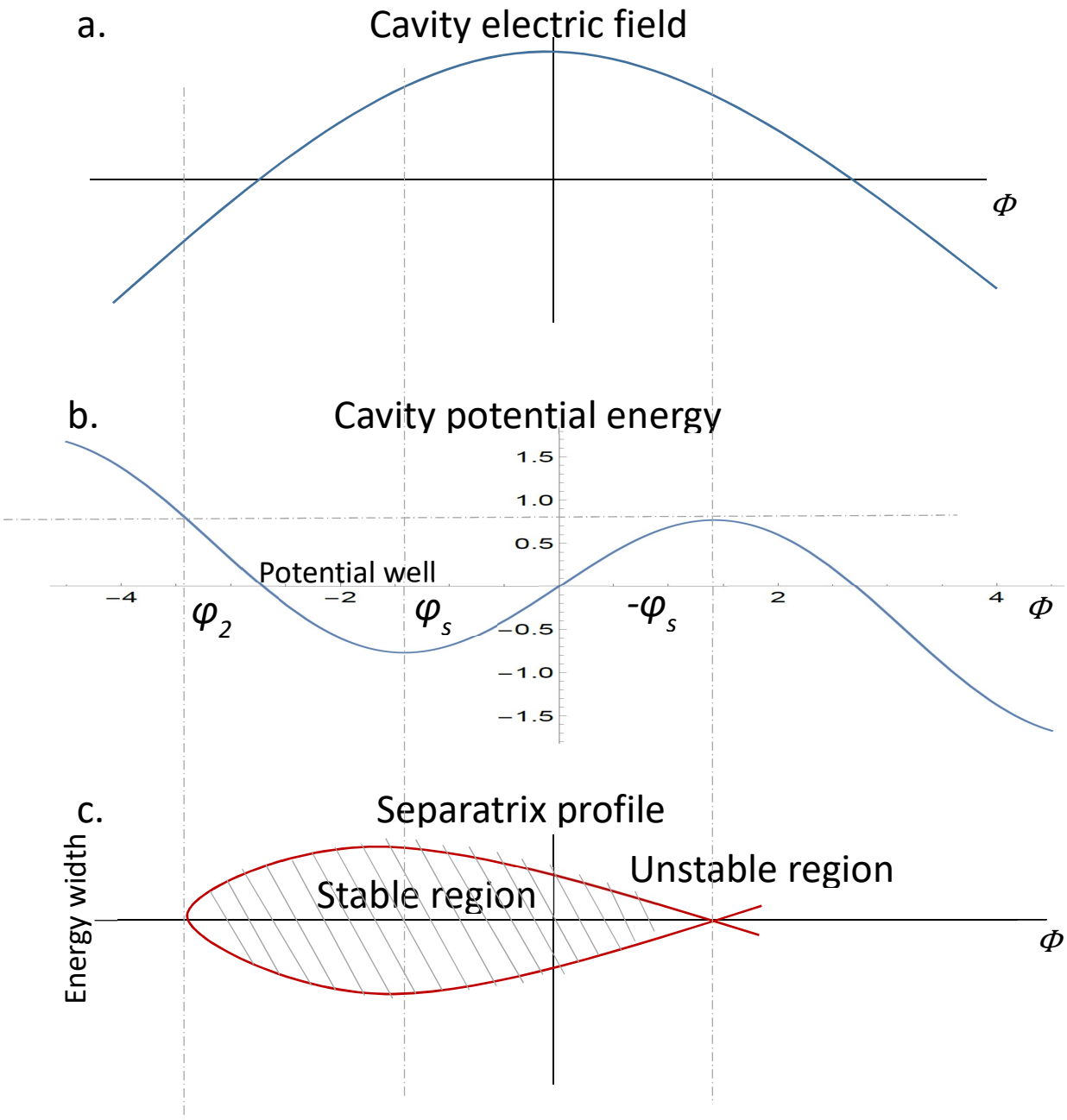

Figure 4.2: a. cavity electric field profile versus cavity phase. b. the cavity potential energy profile. c. the separatrix profile (shaded region) which separates the stable region from the unstable one where small acceleration rate is assumed.

4.3 Emittance

The size of the distribution of ions with a single charge state in 6-dimensions phase-spaces is defined as emittance. The 2-dimensional phase-space projections are described by the transverse phase-space denoted by $(\boldsymbol{x} - \boldsymbol{x}')$ phase space for the x-axis where $\boldsymbol{x}$ the ion position is and $\boldsymbol{x}'$ is the ion velocity. $(\boldsymbol{y} - \boldsymbol{y}')$ phase space for the y-axis where $\boldsymbol{y}$ is the ion position and $\boldsymbol{y}'$ is the ion velocity and for the longitudinal phase-space is denoted by $(\emptyset - \Delta \boldsymbol{w})$ for the z-axis where $\emptyset$ is the ion phase with respect to the synchronous ion phase and $\Delta \boldsymbol{w}$ is the deviation in energy gain from the synchronous ion. The emittance should be minimized as much as possible for better beam quality, i.e. the distribution of the ions in the phase-space is close to the synchronous ion in the bunch. The transverse emittance which is the size of the distribution of the ions in the x-phase-space, $\boldsymbol{\varepsilon_x}$ can be expressed by the ellipse equation (4.10) and for the emittance of y-phase-space by $\boldsymbol{\varepsilon_y}$ can be expressed the ellipse equation (4.11).

$$\boldsymbol{\varepsilon_x = \gamma x^2 + 2\alpha x x' + \beta x'^2} \tag{4.10}$$

$$\boldsymbol{\varepsilon_y = \gamma y^2 + 2\alpha y y' + \beta y y'^2} \tag{4.11}$$

Here, $\boldsymbol{\gamma, \alpha}$ **and** $\boldsymbol{\beta}$ are twiss parameters.

Due to the nonlinearity of ion dynamics in the phase-space, it is better to introduce the Root Mean Squared (RMS) emittance for the ion linac. Since the beam is multi-charge state then each charge state will have its own centroid and bunch. As those bunches accelerate they will oscillate around the synchronous ion in the phase-space. The RMS emittance (effective emittance) is defined as in equations; (4.12) for $(\boldsymbol{x} - \boldsymbol{x}')$ phase-space, (4.13) for $(\boldsymbol{y} - \boldsymbol{y}')$ phase-space and (4.14) for $(\emptyset - \Delta \boldsymbol{w})$ phase-space [9].

$$\varepsilon_{x_{rms}} = \sqrt{\overline{x^2 x'^2} - \overline{xx'}^2} \tag{4.12}$$

$$\varepsilon_{y_{rms}} = \sqrt{\overline{y^2 y'^2} - \overline{yy'}^2} \tag{4.13}$$

$$\varepsilon_{z_{rms}} = \sqrt{\overline{\Delta\emptyset^2 \Delta w^2} - (\overline{\Delta\emptyset \Delta w})^2} \tag{4.14}$$

4.3.1 Longitudinal emittance

As mentioned in the previous section, the longitudinal emittance can be expressed by the equation (4.14). The unit of the longitudinal emittance for an ion linac is often expressed in terms of π-ns-keV/nucleon, π-ns-keV/u or π-degrees-keV/u. Figure 4.3 shows the longitudinal acceptance of L-band 1288 MHz linac and the beam initial distribution. The beam initial distribution was taken from FRIB linac output at an energy of 200 MeV/u for uranium-238 with five charge states (76, 77, 78, 79, and 80) [10]. The blue ellipse contains RMS longitudinal emittance is about 26.3-ns-keV/u and the red ellipse contains 100% longitudinal emittance is about 104.1 π-ns-keV/u. The total number of the simulated ions is 20649.

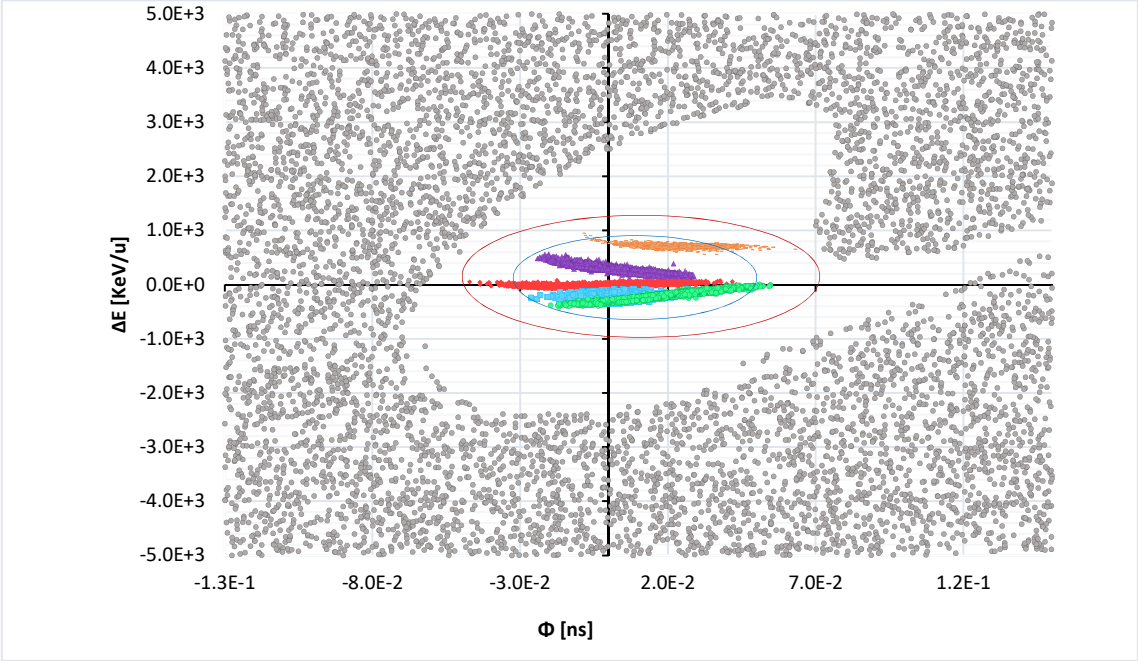

Figure 4.3: The longitudinal acceptance (white area) calculated via TRACK code and the beam initial distribution for uranium-238 with five charge states.

4.3.1.1 Tuning the longitudinal emittance

For a multi-charge-state linac, it is important to tune the longitudinal emittance such that it minimizes any beam losses for accelerator hands-on maintenance. That is due to each charge state bunch has its own centroid that evolves around the synchronous ion. To do this, one should track the centroid of each charge state and tune the cavities synchronous phase such that the synchronous oscillations of the charge states bunches' centroids is minimized and maintain the desired beam energy. In this work, the cavities' synchronous phase was tuned manually, simply it was done by tracking the beam bunches' centroids and minimize their amplitude of oscillations. In addition, there is a feature in TRACK code package named "OPTIM" that can minimize the multi-charge-bunch centroids automatically. Figure 4.4 shows a comparison of tuned and fixed

synchronous phases of a linac. In this figure, A is the distribution of 5 charge states uranium-238 beam with a fixed synchronous phase at an energy of 200 MeV/u, B is a five charge states beam distribution was obtained by Qiang Zhao [11] at a FRIB and C is a distribution of tuned five charge states beam emittance in the longitudinal phase-space plotted with the longitudinal acceptance.

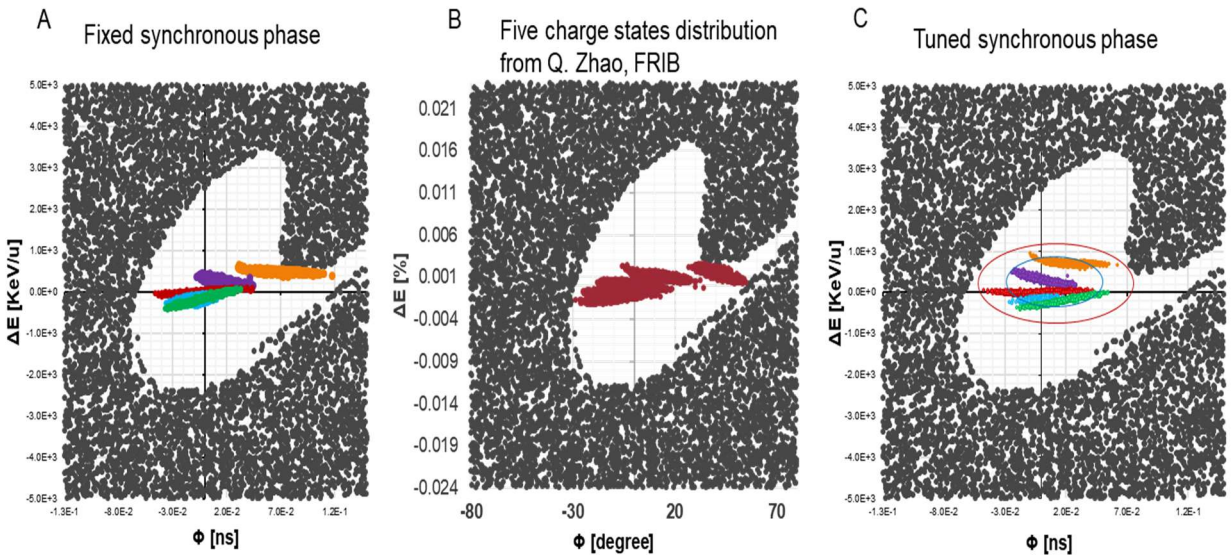

Figure 4.4: A is the distribution of five charge states uranium-238 beam with a fixed synchronous phase at an energy of 200 MeV/u, B is a five charge states beam distribution was obtained by Qiang Zhao, FRIB and C is a distribution of tuned five charge states beam emittance in the longitudinal phase-space.

4.3.2 Transverse emittance

The size of distribution of the beam ions in the transverse plane of phase-space is called transverse emittance. The transverse emittance can be expressed by the equations; (4.15) for $\boldsymbol{x} - \boldsymbol{x}'$ phase-space, (4.16) for $\boldsymbol{y} - \boldsymbol{y}'$ phase-space.

$$\boldsymbol{\varepsilon_x = \Delta x \Delta x'} \tag{4.15}$$

$$\boldsymbol{\varepsilon_y = \Delta y \Delta y'} \tag{4.16}$$

The normalized transverse emittance for x and y can be expressed as $\boldsymbol{\varepsilon_{n_x} = \beta\gamma\varepsilon_x}$ and $\boldsymbol{\varepsilon_{n_y} = \beta\gamma\varepsilon_y}$ respectively.

4.4 Transverse dynamics

Due to the beam tube of the cavity there will be radial electric fields that kick the beam transversely as shown in figure 4.5. At the entrance the ions will experience inward (focusing) radial electric fields and as the ion is accelerated its velocity will increase and when it reaches the end of the cavity, it will experience outward (defocusing) electric fields that will not be compensated by the inward electric fields at the entrance. Thus, there will be a net radial electric field. As a result, the beam will receive transverse kicks as it passes through cavities. That means one needs to utilize a focusing method to compensate for these transverse kicks. As we discussed in chapter 3, FODO cell focusing magnetic quadrupoles can be employed in order to maintain the beam within the beamline and minimize beam losses.

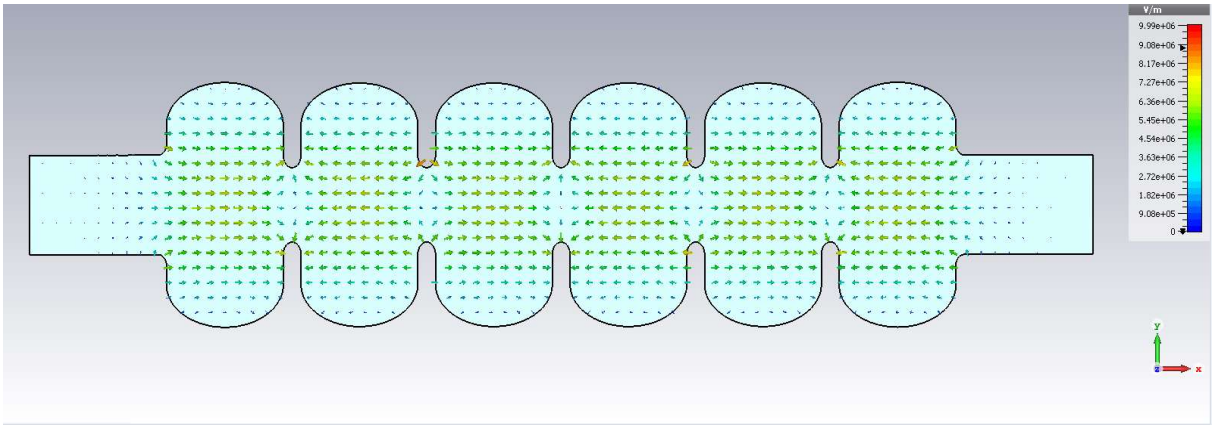

Figure 4.5: 6-cell cavity electric field profile. As shown in this figure, there are radial electric fields at the cell aperture, which kick the beam transversely.

5 Heavy ion medium beta linac structure

5.1 Heavy ion linac typical structure

A typical heavy ion linac consists of ion source to produce ions, a charge stripper system to increase the charge state of the beam for higher acceleration, accelerating cavities for beam acceleration, focusing and steering elements for beam focusing and steering, and a target to produce rare isotope ion fragmentations. In this work, we used the Facility for Rare Isotope Beams (FRIB) beam energy and beam distribution output as an example of heavy ion linac for more realistic simulations. An overview of FRIB baseline linac layout in figure 5.1 is described below.

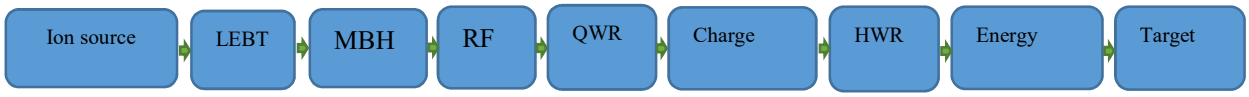

Figure 5.1: The Facility for Rare Isotope Beams (FRIB) Driver Linac.

FRIB baseline consists of:

1. Ion Source: Electron Cyclotron Resonance (ECR) to produce ions
    1. Versatile Electron Cyclotron resonance ion source for Nuclear Science (VENUS) ECR (superconducting ion source) 28 GHz with 50 kV HV platform
    2. Advanced Room-TEMperature Ion Source (ARTEMIS) ECR (Room temperature ion source) at 14 GHz with 100 kV HV platform.

In the ECR, the ion charge state distribution can be described as a 0-Dimension model with a set of balanced equations as shown in equation (5.1) [13].

$$\frac{dn_i}{dt} = \sum_{j=j_{min}}^{i-1} n_e n_j < \sigma_{j\to i}^{EI} v_e > + n_0 n_{i+1} < \sigma_{i+1\to i}^{CE} v_{i+1} > - n_0 n_i < \sigma_{i\to i-1}^{CE} v_i > - \sum_{j=i+1}^{j_{max}} n_e n_j < \sigma_{i\to j}^{EI} v_e > - \frac{n_i}{\tau_i} \quad (5.1)$$

Where $\frac{dn_i}{dt}$ is the growth rate of the ith changed ion state, n_e is ion density with charge state i, σ is the cross-section of microscopic process, τ_i is the confinement time of ion in the plasma, v_e is the electron energy distribution, n_0 is neutral density, and v_i is ion energy distribution. In the equation (5.1), the term $n_e n_j < \sigma_{j\to i}^{EI} v_e >$ is the ion ionization, $n_0 n_{i+1} < \sigma_{i+1\to i}^{CE} v_{i+1} > - n_0 n_i < \sigma_{i\to i-1}^{CE} v_i >$ term is the charge exchange with neutral atoms, $\sum_{j=i+1}^{j_{max}} n_e n_j < \sigma_{i\to j}^{EI} v_e > - \frac{n_i}{\tau_i}$ term is the ion-ion exchange charge, and finally the last term $\frac{n_i}{\tau_i}$ is the lost ions in the ECR chamber walls.

2. Low Energy Beam Transport (LEBT)

This section of the linac purpose is to transport two charge states simultaneously. In addition, in this section collimation channels are implemented to collimate beam halo. Electrostatic dipoles and quadrupoles are utilized to focus the beam.

3. Multi-Harmonic Buncher (MHB) is utilized to pre-bunch the DC beam from the ECR ion source. It operates with three frequencies of 40.25, 80.50 and 120.75 MHz to produce a sawtooth voltage to pre-bunch the DC beam.
4. 80.5 MHz Radio Frequency Quadrupole (RFQ) itself is a linear accelerator. It mainly focuses the beam via Transverse Electric field TE_{210} (quadrupole mode) and uses the perturbation in the electric field between the vane tips to accelerate the beam, i.e. it focuses the beam as it accelerates through the RFQ with an efficiency above 90%. The electric potential expansion in the regular RFQ cell up to 7 orders can be expressed as in equation (5.2) [3].

$$U(r,\theta,z) \approx \frac{V}{2}\left[A_{01}\left(\frac{r}{r_0}\right)^2 cos(2\theta) + A_{10}I_0(kr)\,cos(kz)\right] + \frac{V}{2}\left[A_{03}\left(\frac{r}{r_0}\right)^6 cos(6\theta) + A_{12}I_4(kr)\,cos(4\theta)\,cos(kz) + A_{21}I_2(2kr)\,cos(2\theta)\,cos(2kz) + A_{23}I_6(2kr)\,cos(6\theta)\,cos(2kz) + A_{30}I_0(3kr)\,cos(3kr)\,cos(3kz) + A_{32}I_4(3kr)\cos(4\theta)\cos(3kz)\right] \quad (5.2)$$

Here, V is the tip voltage, r is the particle distance from the RFQ center, r_0 is the vane tip radius, A_{nm} are multipole coefficients related to the tip modulations, k is π/length of modulation cell, I_n is Bessel function and z is the particle position in the beam direction.

5. Bunching cavities

   Normal conducting quarter-wave cavities operate 80.5 MHz to bunch the beam, i.e. without beam acceleration. They operate at a synchronous phase of $-\mathbf{90}°$.

6. Beam focusing elements, normal conducting electro-static and magnetic quadrupole and 8-Tesla superconducting solenoids were utilized to focus and steer the beam.

7. Bending magnets to bend the beam since FRIB is a folded linac.

8. Superconducting accelerating Linac Section

   - 330 Superconducting Radio Frequency (SRF) cavities with two operating frequencies (80.50 MHz and 322 MHz) and 4 beta classes (0.041, 0.085, 0.29, 0.53) for beam acceleration. For the operating frequency, 80.5 MHz section, the linac consists of three ($\boldsymbol{\beta = 0.041}$) cryomodules each contains 4 quarter-wave resonators (QWRs) for beam acceleration and two 8-Tesla 25-cm superconducting solenoid packages for beam focusing and two sets of steering coils and 11 ($\boldsymbol{\beta = 0.085}$) cryomodules each contains 8 QWRs and 3 8-Tesla 50-cm superconducting solenoid packages. For the operating frequency, 322 MHz section, the linac consist of 12 ($\boldsymbol{\beta = 0.29}$) cryomodules each contains 6 Half-Wave-Resonators (HWRs) and one 8-Tesla 50-cm superconducting solenoid

package and 18 ($\boldsymbol{\beta = 0.53}$) cryomodules each contains 8 HWRs and one 8 Tesla 50-cm superconducting solenoid package.

- Reaches 200 MeV/u for uranium-238.

9. Charge stripper to increase ion charge states.
    - Liquid lithium charge stripper

      It utilizes a moving thin film (~10μm) of liquid lithium to remove electrons from the beam ions for higher charge states. Solid charge stripers such as carbon foils cannot sustain a high-power and Continues-Wave (CW) beam operation.
    - Helium gas charge stripper

      It utilizes a helium gas cell confined between two plasma windows to strip electrons from the beam ions. This stripper is a backup plan.
10. Target
    - Rotating metal disk

      Due to the high-power and the continues-wave operation of the beam, a fast-rotating disk is utilized as a target to produce isotopes.
    - Liquid lithium

      It is considered as beam target as well.
11. FRIB cryogenic systems
    - SRF cavities operate at 2 Kelvin
    - SC solenoids operate at 4.5 Kelvin.
12. FRIB energy upgrade:
    - Energy upgrade to ≥ 400 MeV/u for U-238 and maintain a sufficient velocity acceptance for lighter ions and protons
    - High efficiency linac

5.2 Possible SRF cavity classes for medium Beta heavy ion linac

In our heavy ion linac example, a FRIB energy upgrade linac design has to choose an optimized cavity class: cavity type, cavity frequency, number of cells for the cavity, and beta geometry for multi-specie linac in order to maximize the benefits for FRIB energy upgrade. Table 5.1 compares potential cavity classes where the crucial cavity parameters are quantitatively presented. One can note that the higher operating frequency can allow the higher accelerating gradient. In contrast, compared to elliptical cavities the FRIB beta=0.53 Half Wave Resonator (HWR) has higher transit time factor at beta optimum. Whereas, elliptical cavity has higher acceleration efficiency (R/Q). For elliptical cavity classes, a small aperture lowers cell-to-cell coupling. FRIB beam current is very low (several mA). This parameter will not play an important role in the energy upgrade plan. An overview of potential cavity classes for FRIB energy upgrade are discussed below to see their advantages and disadvantages.

1.FRIB beta = 0.53 Half Wave Resonator (HWR)

FRIB already uses the 0.53 HWR [12]. Ninety-six 0.53 HWR cavities will be required to reach 400 MeV/u for uranium.

2.Spoke cavity

Spoke cavity such as the European Spallation Source's (ESS) double spoke cavity can be a suitable for medium beta section [14]. ESS double spoke cavity parameters are summarized in Table 5.1. It has benefits for low frequency and heavy beam loaded cavities; however, these benefits are not so important for FRIB energy upgrade because of the low current machine. Due to the complexity of the cavity shape, i.e. so

many electron beam weldings will be required, thus the cavity production cost is a concern.

3.Elliptical cavity

Elliptical cavity is much simple compared to other HWR or spoke cavity. The technology is well established. It would be a higher potential for FRIB energy upgrade. There is two potential choices of frequencies; 644 MHz and 1288 MHz. Table 5.1 summarizes 644 MHz [15] and 1288 MHz cavities parameters and ion final energy comparisons.

Parameter	HWR FRIB	Double Spoke ESS	Elliptical	Elliptical
Frequency [MHz]	322	322	644	1288
β_g	0.53	0.5(?)	0.61	0.61
Number of cells/gaps	2	2	5	6
Number of Cavities	96		55	99
E_{acc} [MV/m]	10	8	12.4	25
Energy Gain per cavity [MV]	5	5.76	12.4	10.6
Q_0	7.6×10^9		1.0×10^{10}	1.0×10^{10}
R/Q [Ω]	229.5	425	368	262.6
G [Ω]	107.4	131	188	217
Aperture diameter [mm]	40	50	83	60
Cell to cell coupling [%]			0.71	1.34
High field Q-slope	Yes	Yes	No	No
Shape complexity	No	Yes	No	No
Final energy for 238U, q = 78, and E_i= 200 [MeV/u]	400		400	400

Table 5.1: Potential Cavities for FRIB Energy Upgrade Plan

5.3 Possibility of L-band (1288 MHz) SRF cavity for medium-beta heavy ion linac

5.3.1 Choice of operating frequency

Too large frequency jump in linac is not desired. It produces an emittance growth and causes mismatch in beams. The longitudinal acceptance is an important parameter for frequency choice.

5.3.2 Choice of number of cells per cavity

Usually choosing higher number of cells in a cavity is advantageous from the cost point of view. It makes the linac compact and minimizes cost. In our example, FRIB linac, the beam current is low (< 1 mA), i.e. Higher Order Modes (HOM) are not a concern that means increasing number of cells won't affect cavity performance by HOM trapping. However, for multi-specie accelerators such as FRIB, a smaller number of cells increases velocity acceptance as seen in figure 5.2 where Transit Time Factor (TTF) versus beta geometry is plotted for varies number of cells for elliptical cavity. For instance, elliptical cavities with high number of acceleration gaps will be inefficient for protons due to the proton's beta will fall in the transit time factor's curve tail.

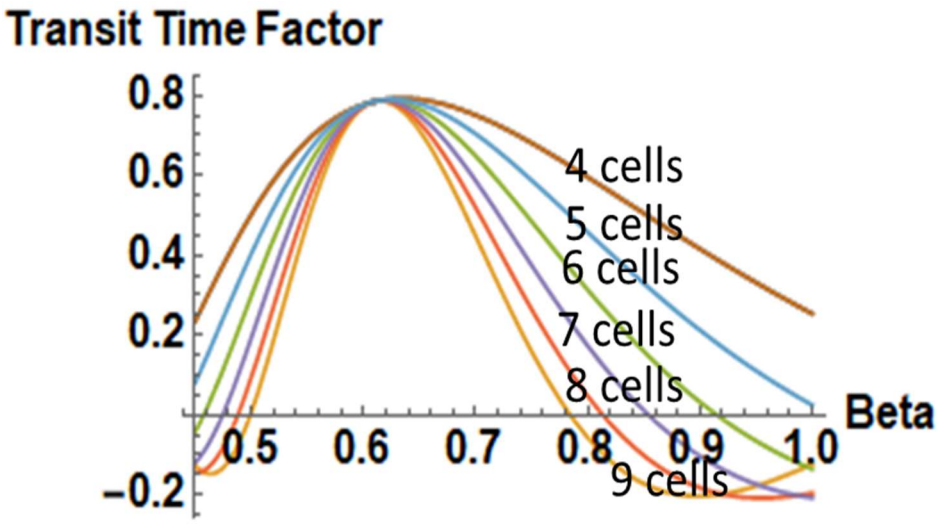

Figure 5.2: Transit Time Factor (TTF) vs. beta with varying number of cells (gaps) for elliptical cavities.

5.3.3 Choice of beta geometry

Since the heavy ion linac is a multi-specie linac, the beta geometry should be optimized such that it accelerates heavy ions such as unranium-238 to 0.71 speed of light (400 MeV/u) and maintain sufficient range of velocity acceptance for other lighter species.

5.3.4 Combination of betas option

To investigate whether or not the energy gain increases significantly, if two beta geometries were utilized in FRIB upgrade linac. We optimized two betas scheme and concluded that the two betas combination scheme would not be efficient due to the insignificant final energy gain (about 4.5%) difference compared with one beta scheme. Moreover, two betas scheme requires more work than one beta scheme. As a result, the

benefit of the two-beta configuration is not attractive. Therefore, one beta geometry scheme is given the preference.

5.4 Cryomodule options

Again, since we used FRIB linac as an example in this work, we learned that due to the limitation in FRIB tunnel entrance which limits the cryomodule length so that it does not exceed the hatch length, which is 6.7 meters. Anything that is needed to be loaded into the tunnel cannot exceed 6.7 meters [11]. Economic cryogenic options such as maximizing number of cavities in the cryomodule and choosing either room temperature or superconducting quadruples for beam focusing were investigated. It concluded that room temperature quadruples for beam focusing for our example for a FRIB case is more efficient if we considered maximizing number of cavities in a cryomodule due to the cryomodule length constraint. In addition, utilizing room temperature quadruples make it easier for correcting misalignment whenever it is needed, however in the case of superconducting quadrupoles, it will be difficult to access the cryomodule and make any adjustment when it is needed. In addition, superconducting quadrupoles need their own cooling-bath that will put an additional static heat load in the cryomodule. In addition, the medium energy does not require high magnetic fields to focusing the beam, i.e. normal conducting magnetic quadrupoles will be more efficient and adequate.

6 High frequency cavity L-band possibility for medium beta heavy ion linac

6.1 High frequency linac structure for medium beta section

6.1.1 1288 MHz elliptical cavity linac layout

The proposed 1288 MHz linac layout consists of eleven cryomodules, each includes nine 6-cell 1288 MHz SRF cavities for beam acceleration and 22 room temperature magnetic quadrupoles for beam focusing. The linac parameters are summarized in Table 6.1. Bellows with a length of 7.10 cm connect the cavities. The cavity beta optimum is 0.65 that is suitable for a potential energy upgrade for heavy ion multi-charge-state linacs such as the Facility for Rare Isotope Beams (FRIB) in the USA [15] and Rare Isotope Science Project (RISP) in Korea [16]. The linac total length is about eighty meters; the cryomodule length is 6.33 meters as shown in figure 6.1 and about one meter, space between cryomodules consists of two 25-cm magnetic quadrupoles and a Beam Position Monitor (BPM).

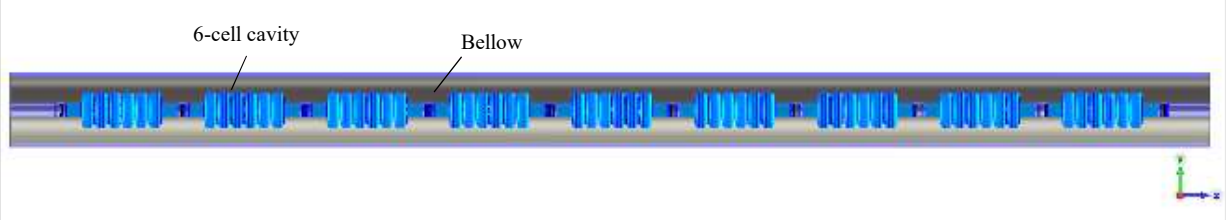

Figure 6.1: 1288 MHz elliptical cavity cryomodule layout with nine 6-cell cavities in CST Studio Suite.

Parameter	Unit	Value
Number of Cryomodules		11
Number of Cavities		99
Number of Cells per Cavity		6
Number of Cavities per Cryomodule		9
Number of Quadrupoles		22
Operating Frequency	[MHz]	1288
Beta Geometry β_g		0.61
Cryomodule Length	[cm]	633.0
Bellow Length	[cm]	7.1
Linac Total Length	[cm]	7933.0

Table 6.1: The linac parameters

6.1.2 1288 MHz cavity parameters

The number of cells of the cavity was chosen to be six, such that it boosts a uranium-238 beam with an average charge state of 78 from an initial energy of 200 MeV/u to ≥ 400 MeV/u and maintain a sufficient velocity acceptance for lighter ions and protons. The length of the accelerating cell is $\boldsymbol{\beta_g \lambda/2}$ and the total length of the cavity is 58.59 cm including beam pipes at both ends with $\boldsymbol{\beta_g = 0.61}$ and a bore radius of 3.0 cm. The electromagnetic design and optimization were performed via the code SUPERFISH [17] as shown in figure 6.2 the peak surface electric field of 76 MV/m can be further optimized via an automatic optimizer such as the one in the software CST Studio Suite. The choice of the cavity bore radius to be 3.0 cm is advantageous due to the smaller

cavity radius the more uniform accelerating fields the ions will experience, i.e. smaller transverse kicks when ions pass through cavities which minimizes the beam centroid oscillations in the space-phase plane. Specially, there were not beam correctors utilized in the 1288 MHz linac structure. In addition, a smaller radius cavity lowers the E_{pk}/E_{acc} that is due to the smaller radius adds more electric volume in the high electric field region of the cavity, i.e. cavity ends.

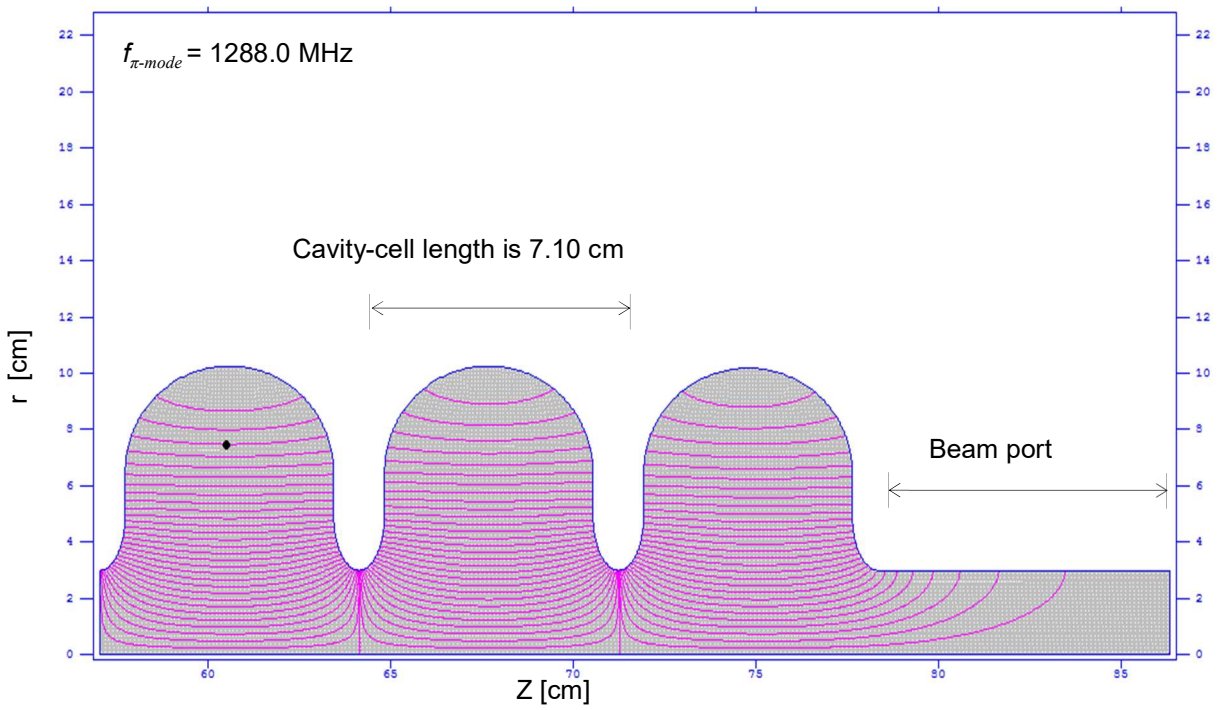

Figure 6.2: 1288 MHz 6-cell half cavity with beta geometry of 0.61 optimized via SUPERFISH code.

The cavity accelerating electric field assumes 25 MV/m at a Continues-Wave (CW) operation, which can be achieved for 1300 MHz cavity [18]. The cavity surface peak magnetic field, H_{pk} is 94.81 mT at 25 MV/m, which is still below the critical magnetic field, H_{c1} for niobium (H_{c1} = ~180.0 mT) [19]. The cavity accelerating voltage is 10.6 MV.

In figure 6.3, the absolute value of electric field along the z-axis is plotted and the field uniformity is > 98%. The cavity parameters are summarized in Table 6.2. The Higher Order Modes (HOM) are not serious for this cavity design because the beam current is less than 1 mA even the high intensity linac for heavy ions, thus the small cell-to-cell coupling factor (1.34%) is not an issue.

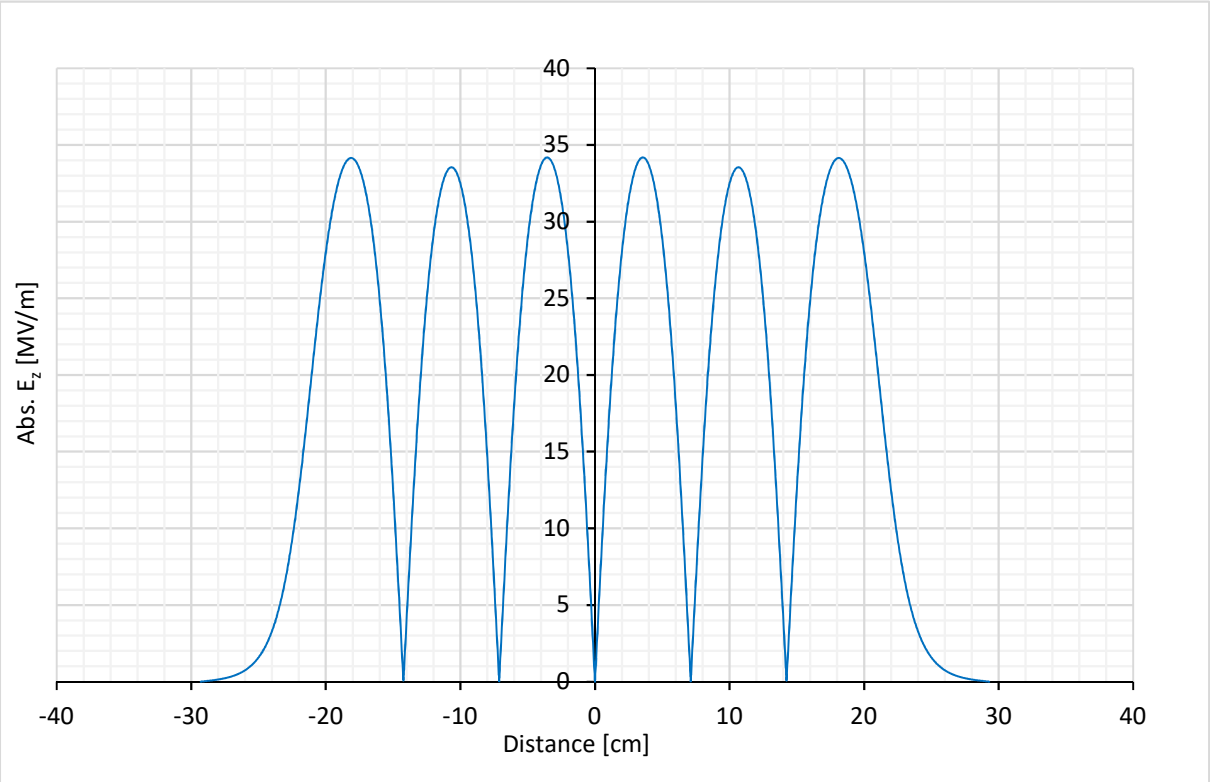

Figure 6.3: The absolute value of the E_z is plotted along the center of the cavity.

Parameter	Unit	Value
Cavity total length (Flange to Flange)	[cm]	58.59
Number of Cells per Cavity		6
E_{acc}	[MV/m]	25
Cavity Voltage	[MV]	10.6
H_{pk}	[mT]	94.81
Operating Frequency	[MHz]	1288
Beta Geometry β_g		0.61
E_{pk}	[MV/m]	76.0
E_{pk}/E_{acc}		3.0
H_{pk}/E_{acc}	[mT/MV/m]	3.8
Cell-to-Cell Coupling	[%]	1.34
Quality Factor Q_0		> 1 x 10^{10}
Geometry Factor G	[Ohm]	217
R/Q	[Ohm]	262.6

Table 6.2: Summary of 1288 MHz cavity parameters

6.1.3 Focusing magnetic quadrupole parameters

A 25-cm magnetic quadrupole with a beam bore radius of 3.0 cm was utilized to focus heavy ion multi-charge-state beams along the linac. The magnetic quadrupole radius at the tip of the iron yoke poles is 3.25 cm, which allows for about 2.0 mm for the beam pipe thickness. As shown in figure 6.4 a 3D model of magnetic quadrupole was

made in CST Studio Suite to obtain 3D magnetic fields for more realistic beam focusing, i.e. including fringe field effect from the magnetic quadrupole. The iron yoke was scaled from Quadrupole #8 (Q8) in FRIB lattice [20].

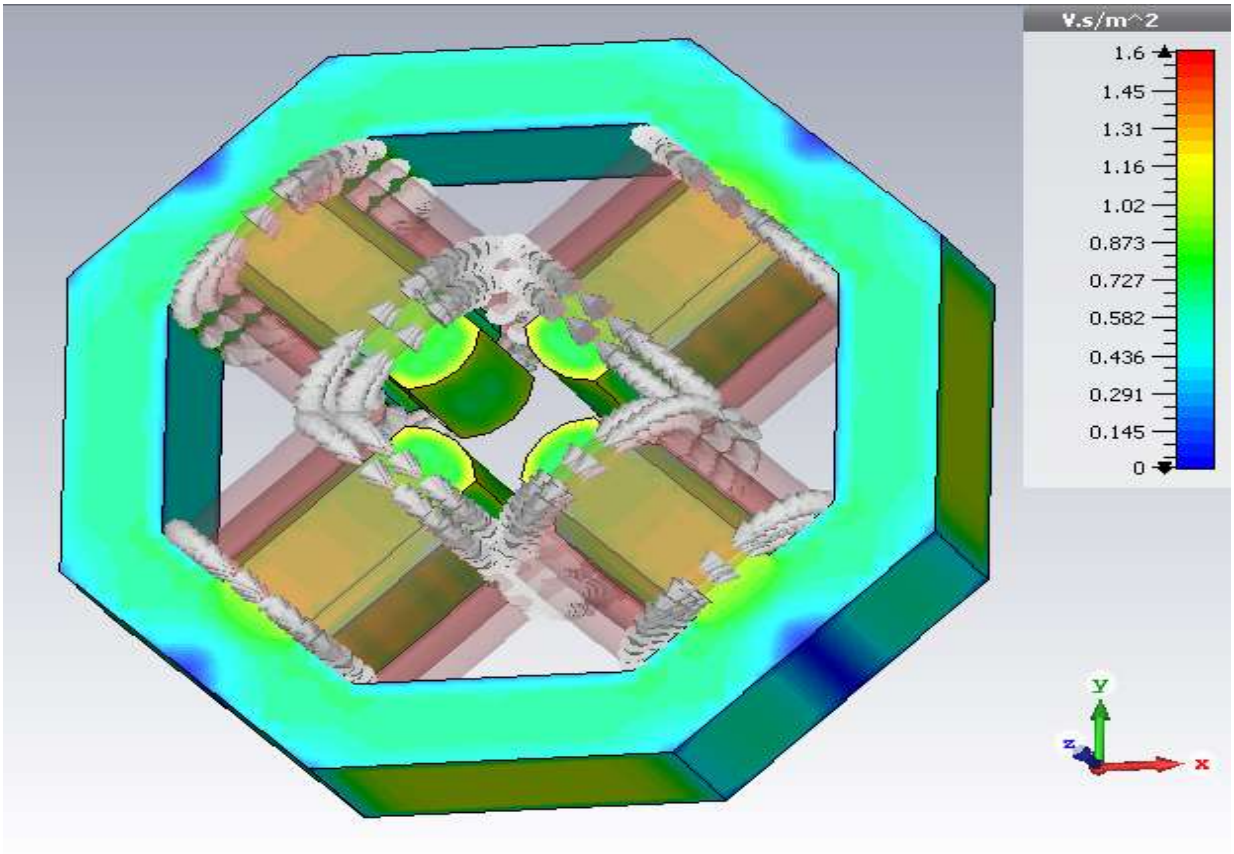

Figure 6.4: 25-cm magnetic quadrupole model in CST Studio Suite.

In figure 6.5 the 3D magnetic quadrupole field profiles are plotted at transverse component (X= Y = 1.50 cm) along z-axis. In figure 6.5 the transverse-component of the magnetic field is in red of the magnetic field and the longitudinal-component of the magnetic field is in green.

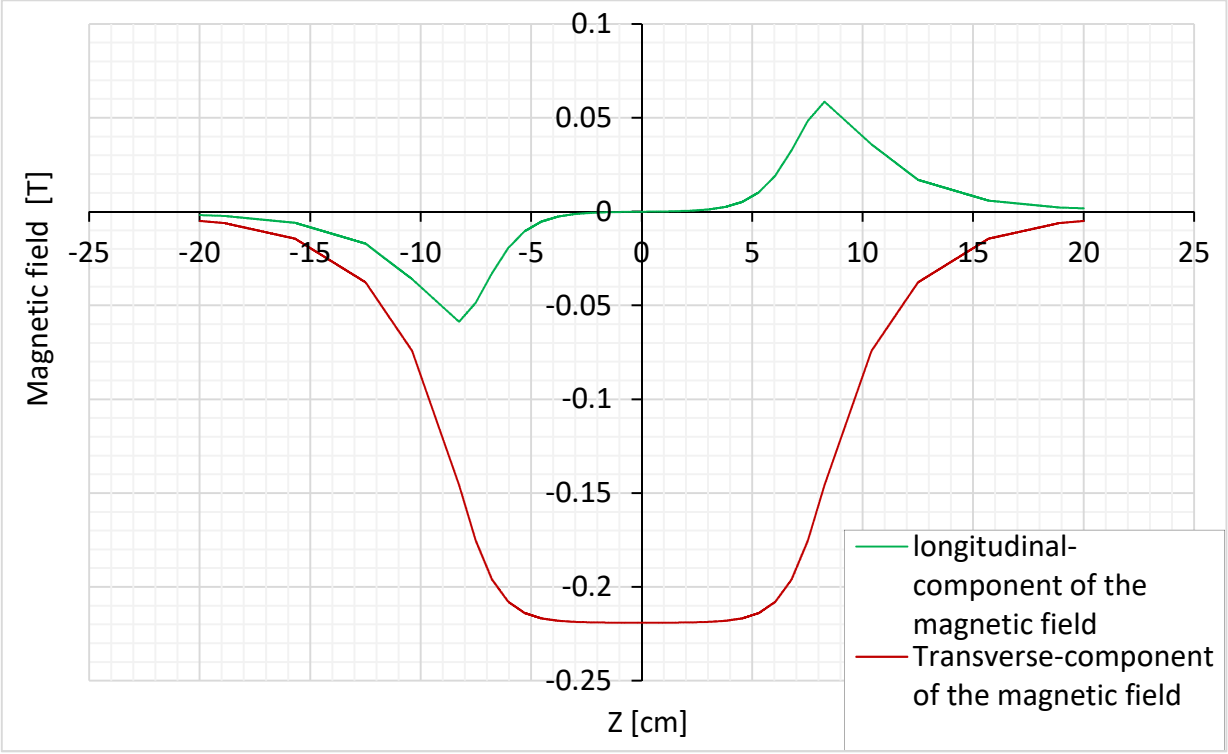

Figure 6.5: 25-cm magnetic quadrupole field profiles at X =Y = 1.50 cm along z-axis.

6.2 Longitudinal and transverse beam dynamics studies for the proposed linac

6.2.1 Initial beam distribution

The initial beam distribution was taken from FRIB linac output at an energy of 200 MeV/u for uranium-238 with five charge states (76, 77, 78, 79, and 80). In TRACK code, the longitudinal emittance is defined by the area of an ellipse that contains a certain number of ions given by the input of the TRACK code file made by the user. The Root Mean Squared (RMS) emittance is calculated by Track code from the input data above. The longitudinal phase-space distribution of the beam of the five charge states at the linac entrance (at a beam energy of 200 MeV/u) is plotted in figure 6.6. The blue ellipse shows RMS longitudinal emittance ellipse as calculated above of about 26.3 π -ns-keV/u

and the red ellipse contains the 100% longitudinal emittance of about 104.1 π-ns-keV/u. The 100% beam emittance can be sometimes misleading. Suppose that one ion is much far from the beam centroid from one side and there is another ion far from the beam centroid at the other side. Those ions will still be counted in the 100% beam emittance ellipse. That would give the impression that the beam emittance is larger than what actually is. In other words, the 100 % emittance cannot be a good measure for the beam quality. On the other hand, the RMS longitudinal emittance is sufficient for mapping the distribution of ions in the longitudinal phase-space, especially, for multi-charge-state beams. If this emittance is not constant along the linac, it indicates the centroids of the beam bunches are oscillating, i.e. the beam quality is degraded.

For the space charge dominated beams like high intensity proton linacs at SNS, J-PARC and others, the RMS emittance cannot be a good measure, since halos and tails grow beyond the RMS ellipse. However, the heavy ion CW linac here has still very low peak current without any space charge force practically speaking. In this case, the RMS emittance can be a good measure.

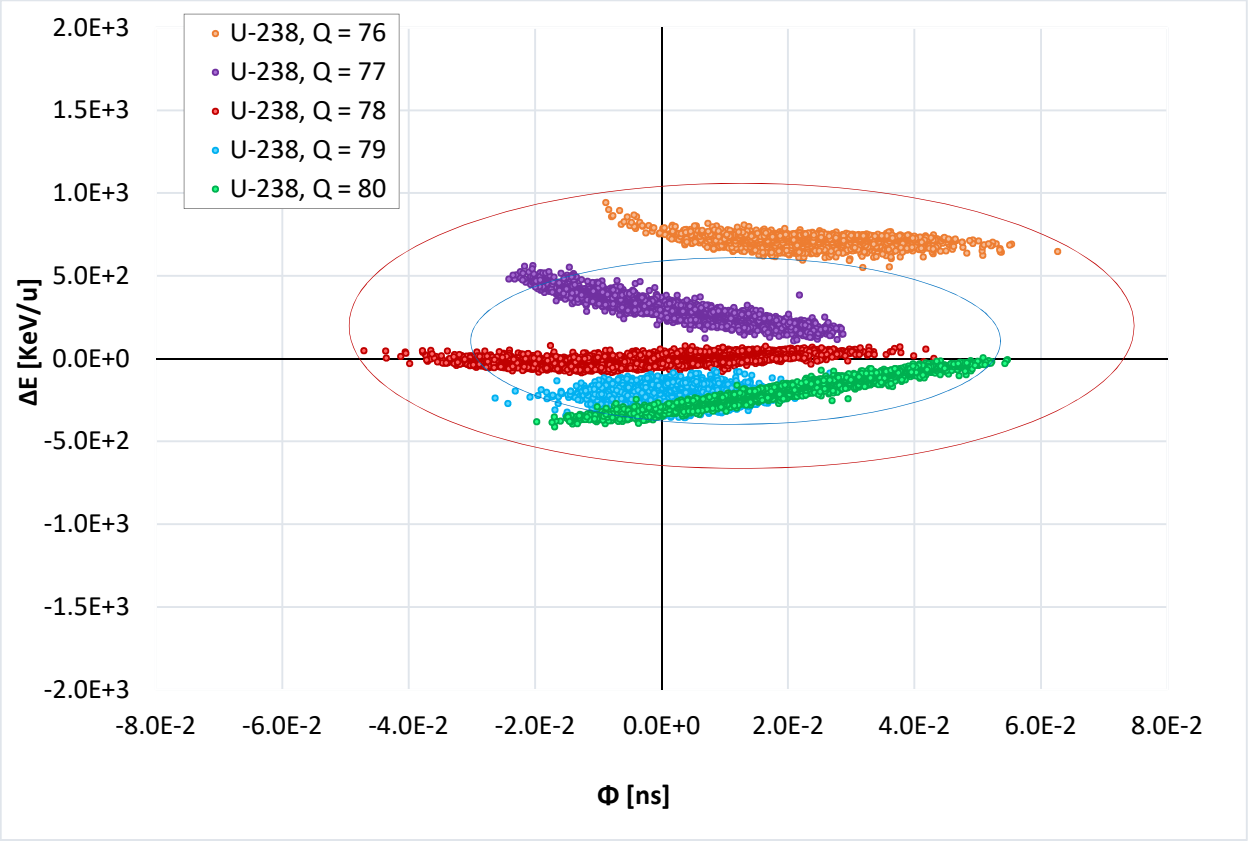

Figure 6.6: The beam distribution in the longitudinal phase-space of the five charge states at the entrance of the linac.

As we discussed in chapter 4, the cavity electric field is sinusoidal. Half period of the cavity electric field is plotted in figure 6.7.a to show that there is a potential well in the phase interval ($-\pi < \boldsymbol{\phi_s} < 0$) in cavity potential energy profile, $\boldsymbol{E_0}$ is defined as in equation (6.1) and as illustrated in figure 6.7. b.

$$\boldsymbol{E_0 = B(sin\phi - \phi cos\phi_s)} \tag{6.1}$$

Here, B is a constant.

The separatrix which separates the stable region from the unstable one is defined in the region of stable phase motion in potential well $\boldsymbol{\phi_2 < \phi_s < -\phi_s}$. In figure 6.7. c. If we assume a small rate of acceleration, then the separatrix profile becomes a fish shape, whereas if we assume a large acceleration rate the shape of the separatrix becomes a golf club shape, which reduces the stable region size in the longitudinal phase-space.

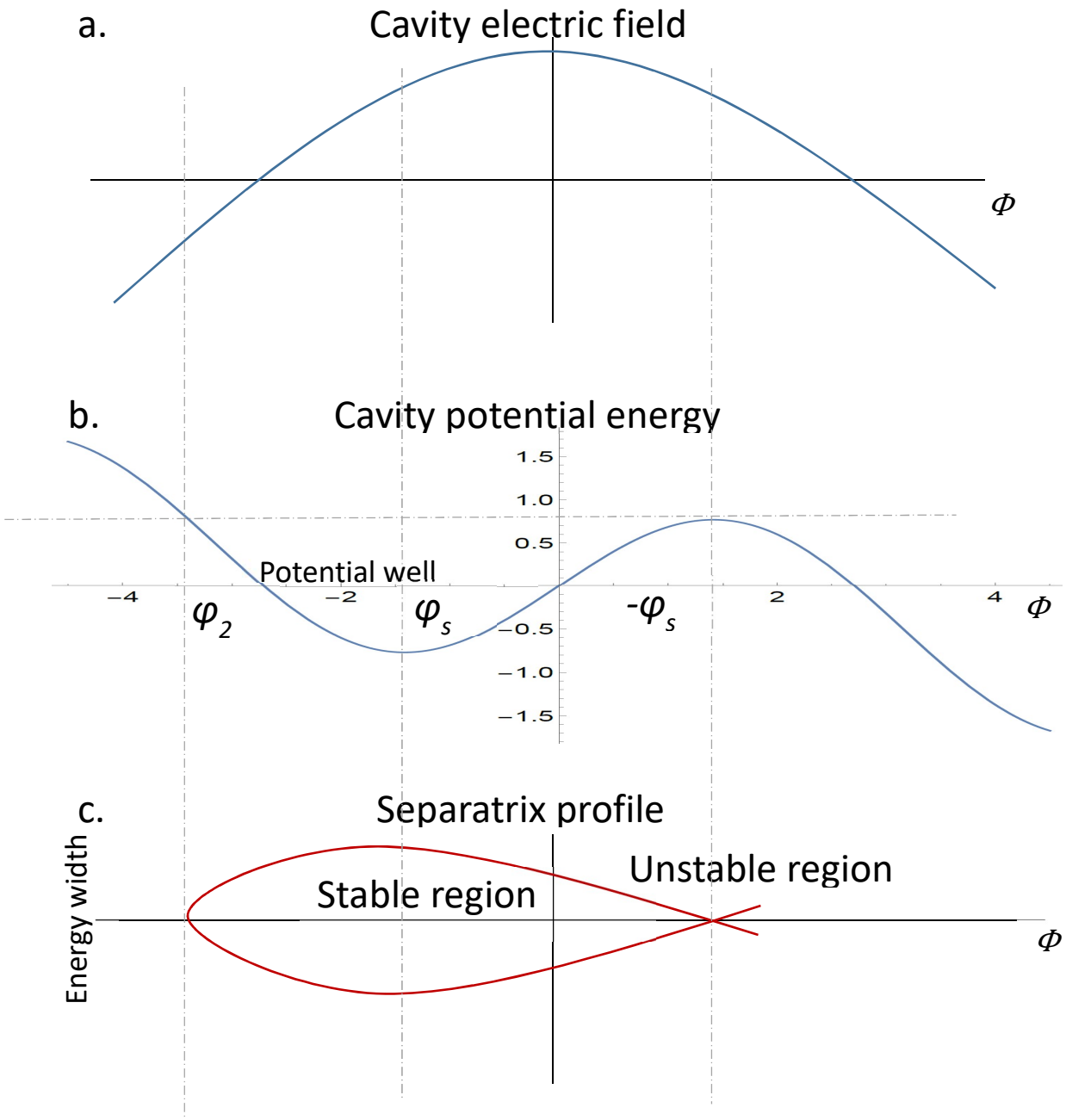

Figure 6.7: a. cavity electric field profile versus cavity phase. b. the cavity potential energy profile. c. the separatrix profile which separates the stable region from the unstable one where small acceleration rate is assumed.

6.2.2 Longitudinal acceptance of the linac and beam emittance

The analytically calculated initial longitudinal acceptance is 141.3 π -ns-keV/u at a synchronous phase of $-\mathbf{30}°$. The longitudinal acceptance is defined as $\boldsymbol{\pi . w_{max} . \phi_{max}}$. It is estimated using the following equation (6.2) for the maximum energy deviation half width and the maximum phase width $\boldsymbol{\phi_{max}}$ is determined from the equation (6.3) see reference [9].

$$w_{max} = \frac{\Delta W_{max}}{mc^2} = \sqrt{(\phi_s cos\phi_s - sin\phi_s)\frac{2qE_0 T\beta_s^3\gamma_s^3\lambda}{\pi m^{\ 2}}} \tag{6.2}$$

$$sin\phi_2 - \phi_2 cos\phi_s = \phi_s cos\phi_s - sin\phi_s \tag{6.3}$$

where $\boldsymbol{w_{max}}$ is the maximum energy half width normalized by the rest mass energy, $\boldsymbol{mc^2}$, $\boldsymbol{\phi_s}$ is the synchronous phase, q is the ion charge state, $\boldsymbol{E_0}$ is the cavity potential, T is the transit time factor, $\boldsymbol{\beta_s}$ is the velocity of the synchronous ion, and $\boldsymbol{\lambda}$ is the RF wavelength. The calculated longitudinal acceptance via TRACK code is about 139.6 π -ns-keV/u that is comparable to the value that was calculated analytically. Figure 6.8 shows the longitudinal acceptance calculated via TRACK code and the initial beam distribution in the longitudinal phase-space for uranium-238 with five charge states (76, 77, 78, 79, and 80). The total number of ions is 20649 distributed as follows: 2549 ions for q= 76, 4365 ions for q= 77, 5321 ions for q= 78, 5061 ions for q= 79, 3353 ions for q= 80.

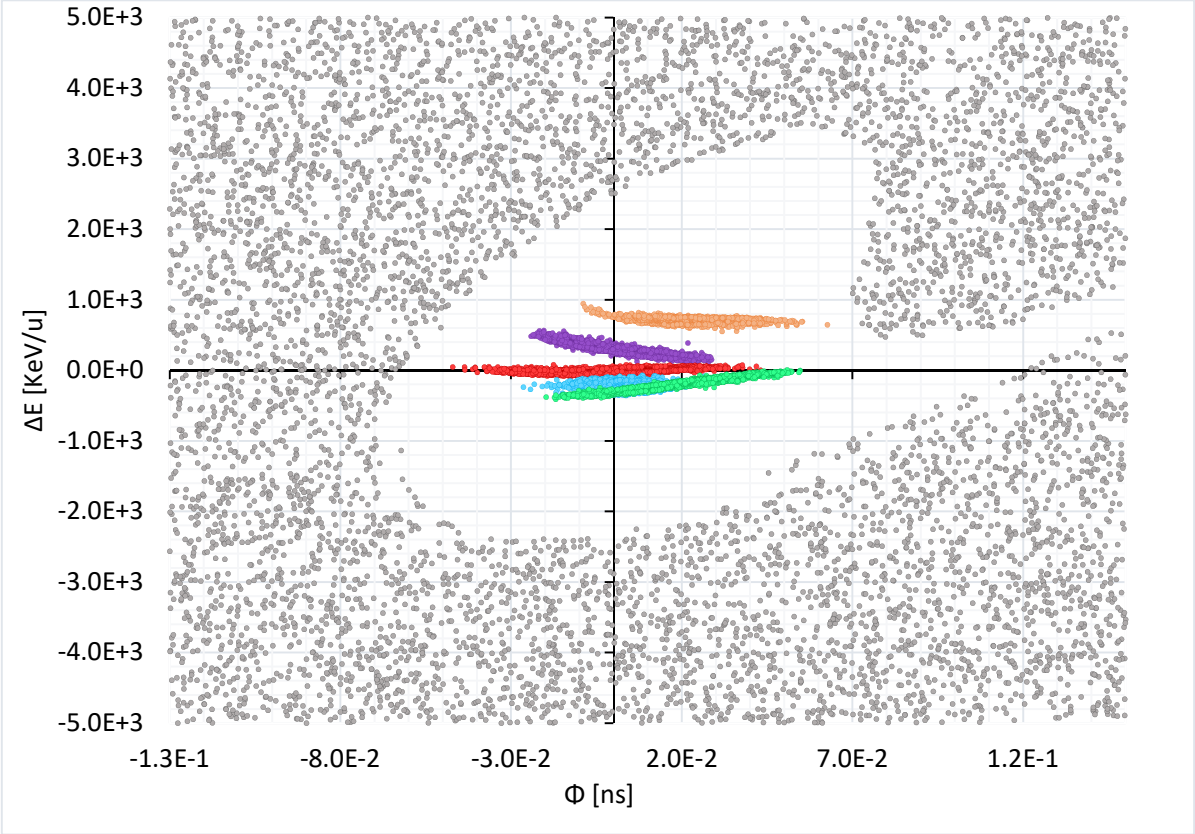

Figure 6.8: The longitudinal acceptance calculated via TRACK code and the beam initial distribution for uranium-238 with five charge states orange is 76, purple is 77, red is 78, blue is 79, and green is 80).

6.2.3 Longitudinal beam emittance along the linac

The synchronous phase was tuned as follows.

1. Preserve the longitudinal emittance along the linac with one re-buncher cavity (cavity 19) to reach the desired final energy.
2. Maintain a sufficient acceptance to transport maximum number of ions.
3. Minimize any beam losses.
4. Preserve beam quality.

The cavity 19 was set as a re-buncher ($\boldsymbol{\phi_s = -90°}$), since the longitudinal emittance grew significantly at this cavity location. We thus, had to use this cavity as a re-buncher to bring ions back in bunches and to minimize the effective emittance. Further synchronous phase tuning can be made to overlap the five charge state bunches at the linac entrance in the longitudinal phase-space. In other words, we thus, minimize the effective emittance at the linac entrance. The longitudinal emittance was tracked along the linac for uranium-238 with five charge states without errors is shown in figure 6.9. In figure 6.9, the blue is 100% longitudinal emittance, the red is 99.5% longitudinal emittance and the green is RMS longitudinal emittance for uranium-238 with the five charge states without errors. The oscillatory evolution of the RMS emittance can be explained by the fact that the beam is multi-charge-state, that is the beam evolves around the design particle. In this case, the design particle (reference particle) is the charge state 78 in red as shown in the figure 6.9. The RMS longitudinal emittance at the linac end is about 20.0 π -ns-keV/u, which is less than the initial value of 26.3 π -ns-keV/u at the inlet of the linac. That is partly due to the adiabatic damping.

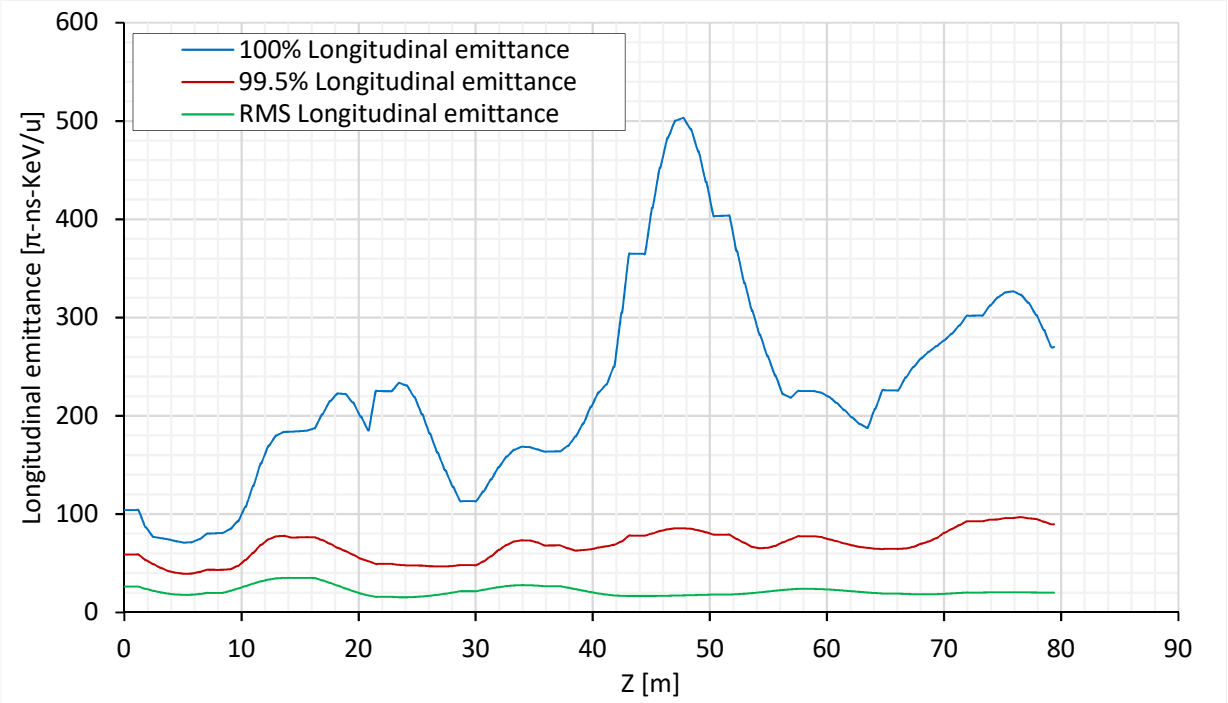

Figure 6.9: The longitudinal emittance evolution along the linac. Blue is 100% longitudinal emittance; the red is 99.5% longitudinal emittance and the green is RMS longitudinal emittance for uranium-238 with multi-charge-states.

6.2.4 Transverse beam emittance along the linac

The normalized transverse emittance was tracked along the linac as shown in figure 6.10. It shows the RMS transverse emittances of the X and Y phase-spaces almost are constant and overlapped. It indicates that the strengths of the focusing elements in the linac lattice are adequate.

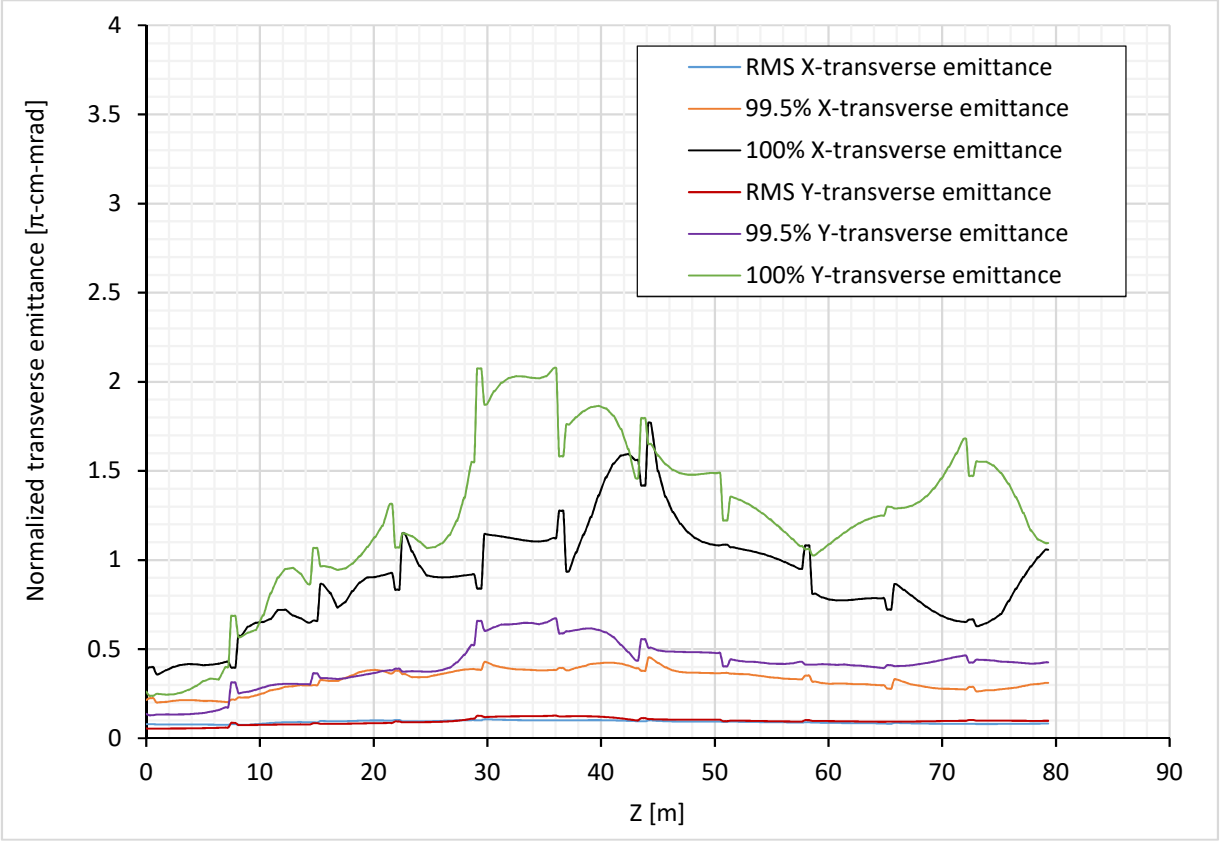

Figure 6.10: The transverse emittance evolution along the linac. Blue is RMS X-transverse emittance, the orange is 99.5% X-transverse emittance, the black is 100% X-transverse emittance, the red is RMS Y-transverse emittance, the purple is 99.5% Y-transverse emittance, the green is 100% Y-transverse emittance for uranium-238 with multi-charge-states.

6.2.5 Transverse beam envelope along the linac

The transverse beam envelope was tracked along the linac as shown in figure 6.11. It shows that the transverse beam envelope was tuned to less than 3.0 cm for maximum transverse beam envelope along the linac. The focusing strength of the magnetic quadrupole was in the range of 5500- 8900 Gauss at r = aperture radius which is still

below the saturation magnetic field (above 1.6 T) for Steel 1008 iron yoke that was utilized in the simulation on CST Studio Suite [7].

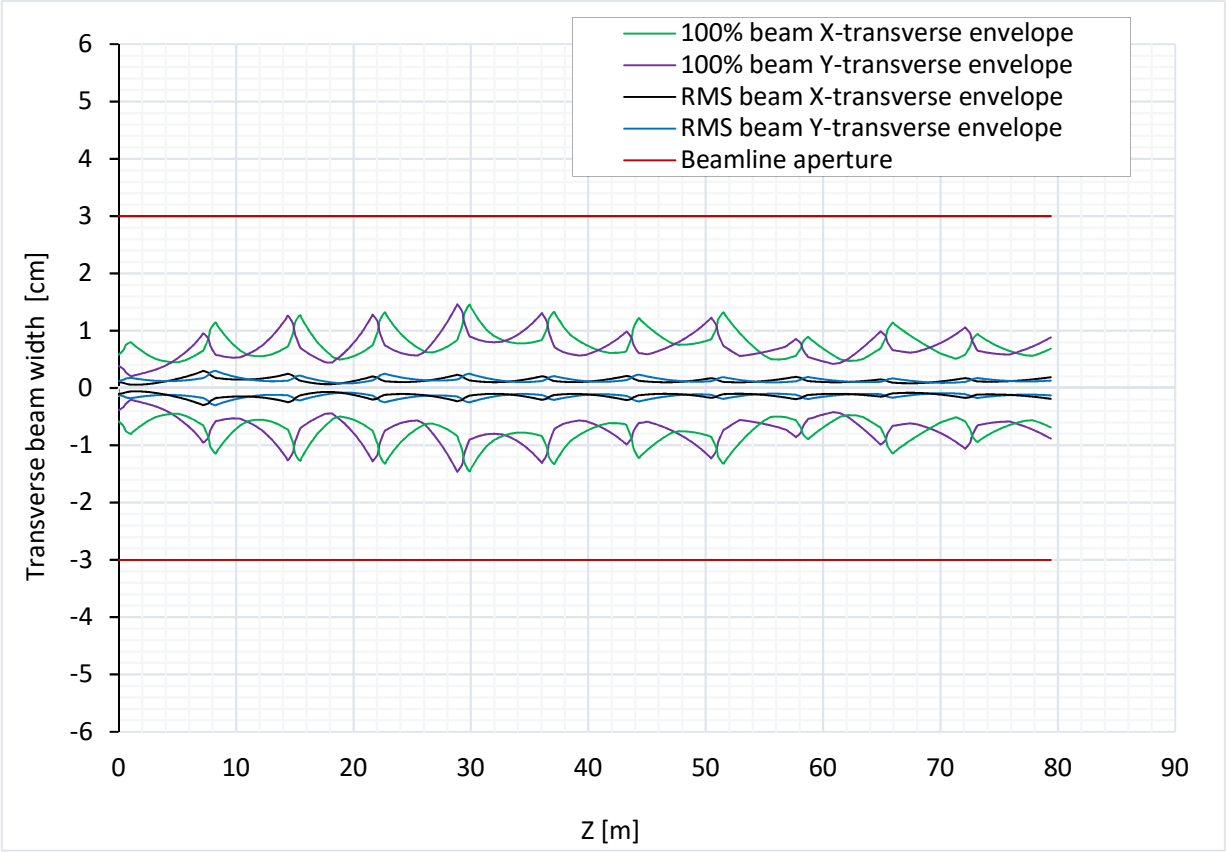

Figure 6.11: The transverse beam envelope along the linac. The green is X-transverse width of 100% beam, purple is Y-transverse width of 100% beam, black is X-transverse width of RMS beam, blue is Y-transverse envelope of RMS beam and the red is the beamline aperture.

6.3 Bunch centroids and single ion synchronous oscillations in longitudinal phase-space

6.3.1 Bunch centroid oscillations around the synchronous ion

The bunch centroid of each charge state was tracked along the linac in the longitudinal phase-space as illustrated in figure 6.12. The synchronous phase was tuned to minimize the oscillation of each charge state centroid around the synchronous ion, i.e. charge state 78 centroid that minimizes the effective longitudinal emittance and preserves beam quality. As it can be seen from figure 6.12, centroid of the charge states 76 and 80 show maximum synchronous oscillations, which longitudinally oscillate between the head and the tail of the beam.

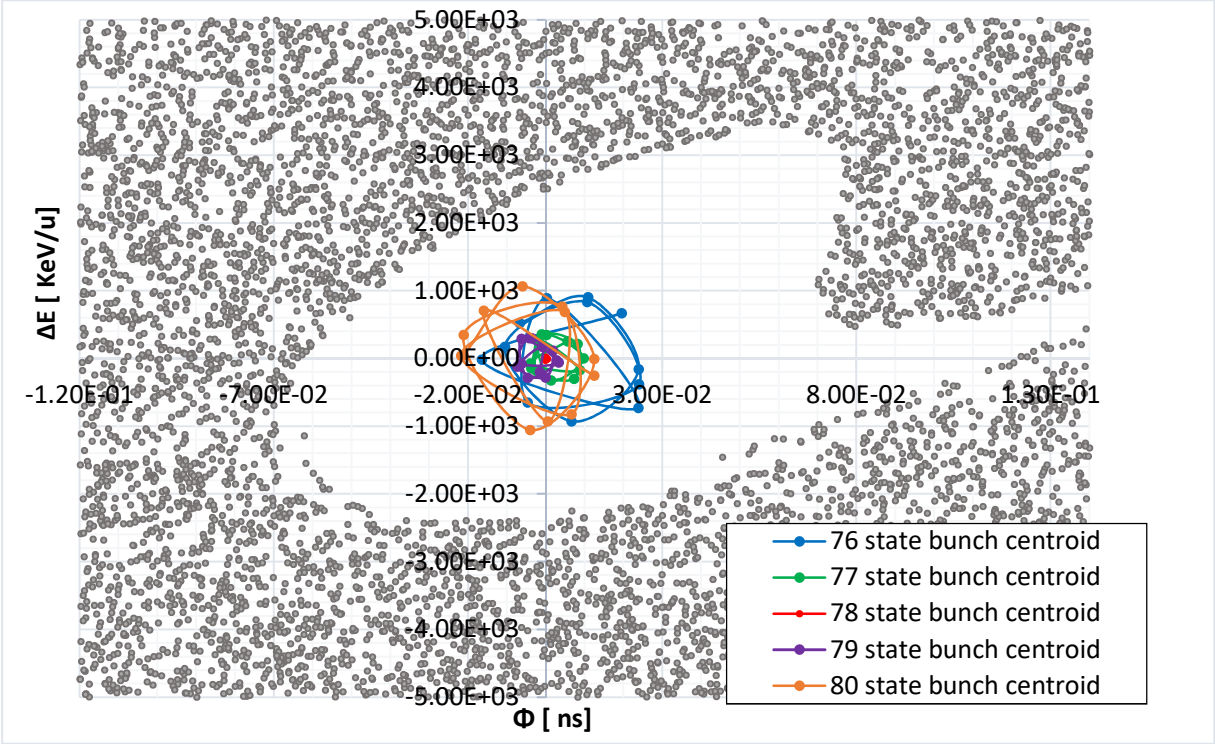

Figure 6.12: The five charge-state bunch centroids were tracked in the longitudinal phase-space along the linac within the acceptance. The blue is bunch centroid of the charge state 76, green is 77, red is 78 (synchronous particle), purple is 79, and orange is 80 charge state centroid.

6.3.2 Synchronous oscillations for arbitrary ions around the synchronous ion

An arbitrary ion from each charge state was tracked in the longitudinal phase-space as shown in figure 6.13 with the longitudinal acceptance and synchronous oscillations.

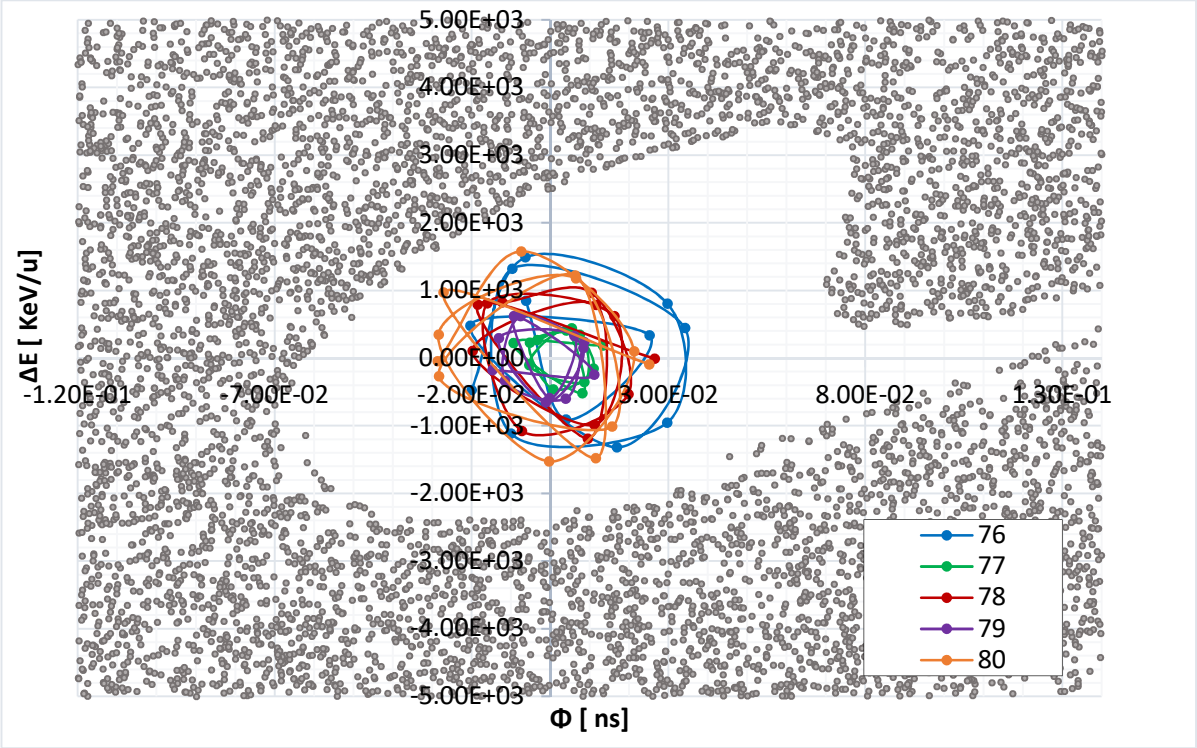

Figure 6.13: An arbitrary ion from each charge state was tracked in the longitudinal phase-space along the linac within the acceptance. The blue bunch centroid of the charge state 76, green is 77, red is 78, purple is 79, and orange is 80.

6.3.3 Linac tolerance to misalignment and field phase and amplitude errors

To investigate the linac tolerance to errors we added misalignments and field phase and amplitude errors to the simulations. The phase and amplitude static errors are uniformly distributed in the interval [1, -1]. A Gaussian distribution with a standard deviation of σ was used to represent the dynamic errors of the phase and amplitude. It is truncated at $\pm 3\sigma$ [3]. Although, usually the dynamic errors, which are the errors from external sources such as microphonic and thermal effects of the RF reference line are much smaller than the static errors (power source control), the static and the dynamic phase and field errors were given equal values to be very conservative from

linac operation point of view. The linac tolerance values in Table 6.3 are twice the values in the reference [21] except for the magnetic quadrupole misalignment value. When that value was doubled, there was beam losses (9 ions were lost from a total of 20649 ions). This sets the limitation of ±0.1 mm for the magnetic quadrupole misalignment tolerance. This is achievable as shown in the references [22] and [23] where the maximum misalignment is ±0.1 mm. In figure 6.14 the RMS longitudinal emittance was tracked along the linac for 200 seeds error trials. In all error trials, the 100% beam was transported to the linac end without any beam losses. The oscillation of the RMS longitudinal emittance due to the effect of the multi-charge states still can be seen in all error trials. The maximum growth in longitudinal emittance was observed in the error trial 82, which is shown in red in figure 6.14. Even in this error trial, the maximum value of RMS longitudinal emittance is approximately 44.3 π-ns-keV/u at the linac end without any beam losses, that is the 100% beam was transported to the linac end.

Parameter	Unit	Tolerance	Distribution Static / Dynamic
Cavity displacement	[mm]	±1.0	Uniform
Quadrupole displacement	[mm]	±0.1	Uniform
Element rotation	[mrad]	±4.0	Uniform
RF phase fluctuation	[Degree]	±1.0	Uniform/ Gaussian
RF field fluctuation		±1.0%	Uniform/ Gaussian

Table 6.3: Linac tolerance table

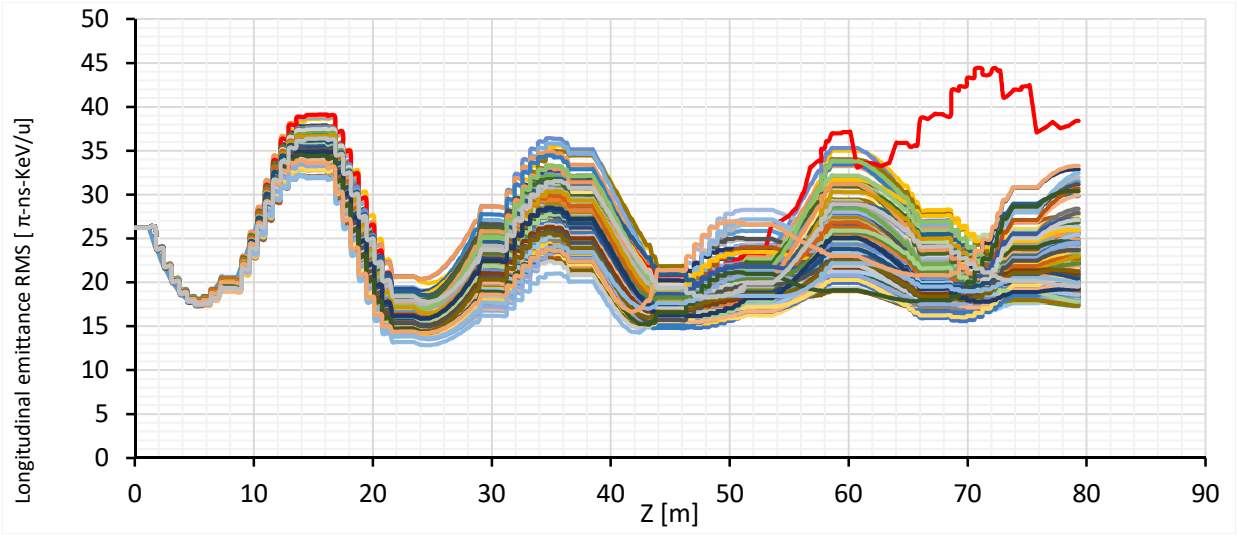

Figure 6.14: The RMS longitudinal emittance was tracked along the linac for 200 seeds error trial.

6.4 Beam loss studies

6.4.1 Linac sensitivity to misalignment

To test the robustness of the machine, we doubled all linac elements errors and we found that beam losses occurred twice in 200 error seeds. The run 109 had lost four ions at the end of the cryomodule #5 at the last cavity and quadrupole #6 as illustrated in figure 6.15. In addition, we can see that the longitudinal emittance did not grow significantly near the lost ions location as illustrated in figure 6.16. The run 194 had lost nine ions at the quadrupole #8 as shown in figure 6.17 and again the longitudinal emittance did not blow up at the vicinity of where the ions were lost as shown in figure 6.18. Clearly, that indicates the ions were lost due to the quadrupole misalignment above the machine tolerance. In order to determine the limitation of misalignment of the magnetic quadrupole, we increased the misalignment error in the magnetic quadrupole

by a 0.01 mm step size until beam losses occurred. It turned out the maximum tolerance of misalignment in the magnetic quadrupole is ≤ 0.15 mm.

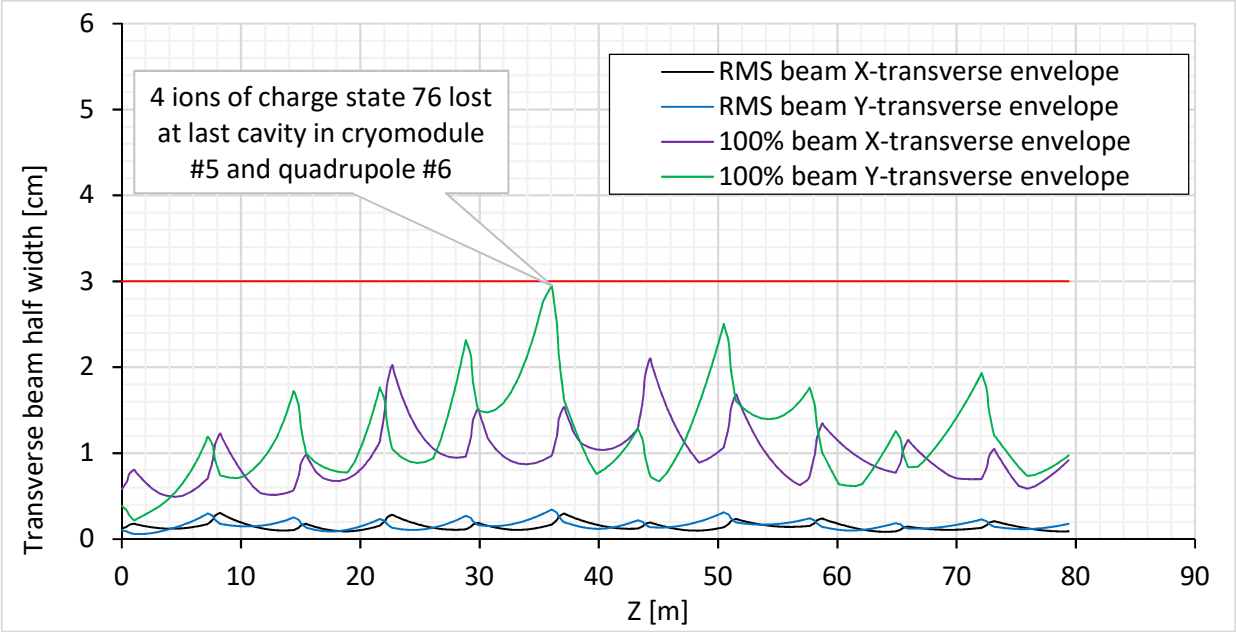

Figure 6.15: The transverse beam envelope along the linac for the run 109, which had lost 4 ions. The green is X-transverse width of 100% beam, purple is Y-transverse width of 100% beam, black is X-transverse width of RMS beam, blue is Y-transverse envelope of RMS beam and the red is the beamline aperture.

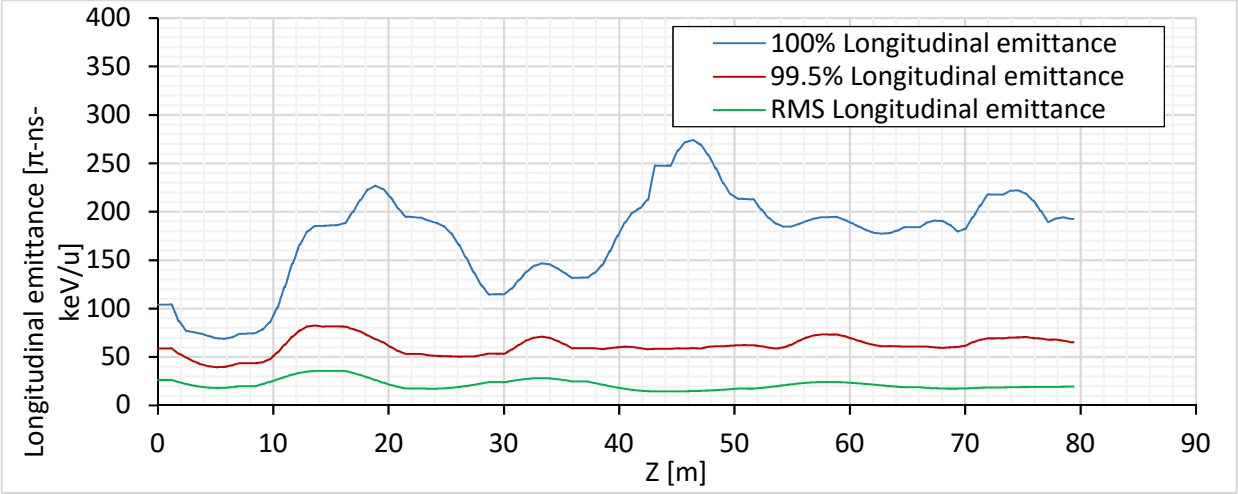

Figure 6.16: The longitudinal emittance evolution along the linac for the run 109. Blue is 100% longitudinal emittance; the red is 99.5% longitudinal emittance and the green is RMS longitudinal emittance for uranium-238 with multi-charge-states.

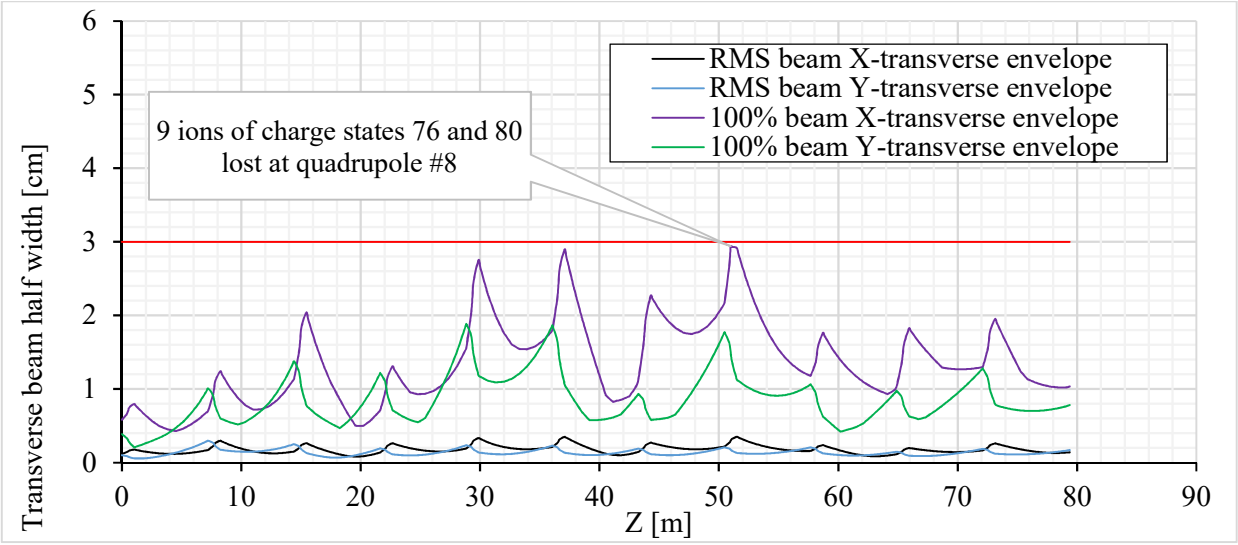

Figure 6.17: The transverse beam envelope along the linac for the run 194, which had lost 9 ions. The green is X-transverse width of 100% beam, purple is Y-transverse width of 100% beam, black is X-transverse width of RMS beam, blue is Y-transverse envelope of RMS beam and the red is the beamline aperture.

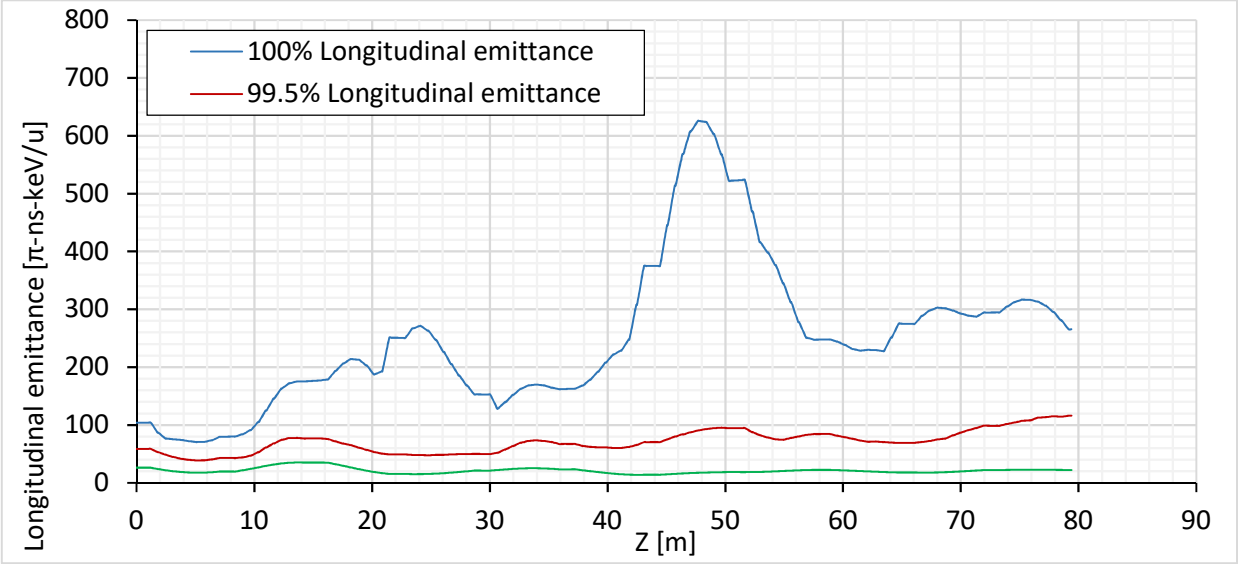

Figure 6.18: The longitudinal emittance evolution along the linac for the run 194. Blue is 100% longitudinal emittance; the red is 99.5% longitudinal emittance and the green is RMS longitudinal emittance for uranium-238 with multi-charge-states.

6.4.2 Linac sensitivity to RF phase errors

To explore the limitation of the phase errors, we implemented the error values in Table 6.1 and amplified the error values in the RF phase by a 0.1-degree step size until beam losses occurred. It turned out that the linac maximum tolerance to RF phase error is ≤ 1.4 degrees and that corresponds to a cavity longitudinal displacement of 0.9 mm if the phase is converted from degrees to distance along the beam direction. Again, the longitudinal emittance did not grow in the vicinity where the ions were lost.

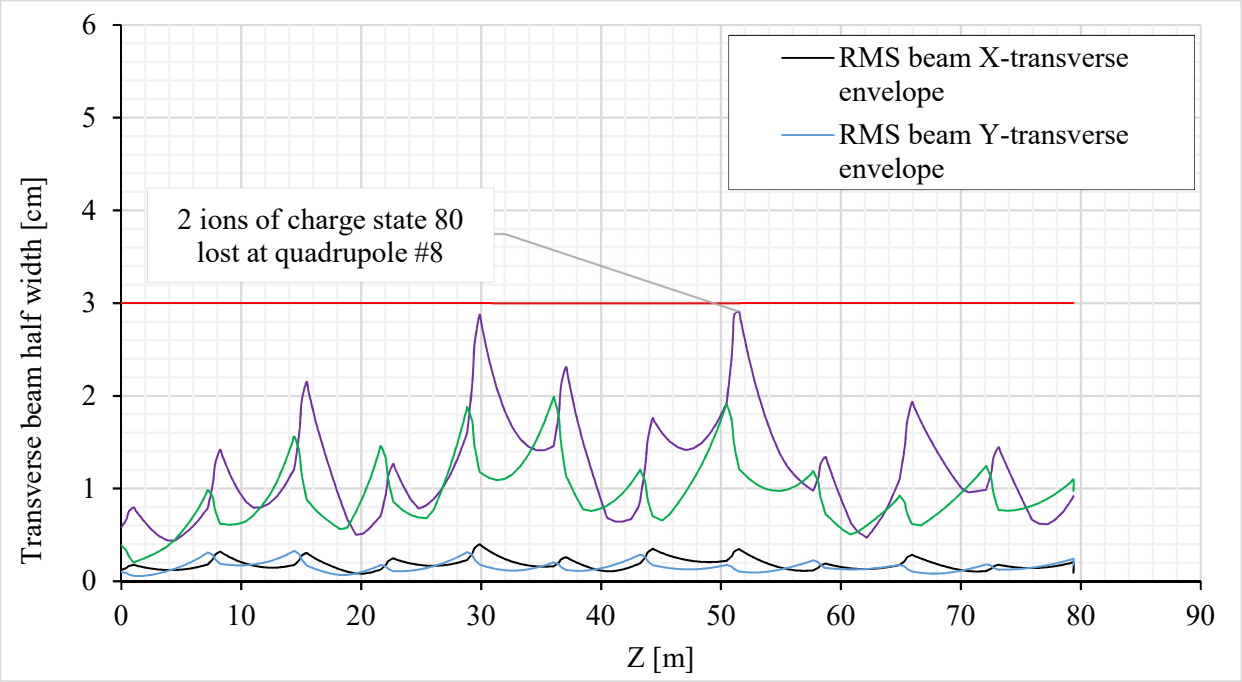

Figure 6.19: The transverse beam envelope along the linac for the run 117, which had lost 2 ions. The green is X-transverse width of 100% beam, purple is Y-transverse width of 100% beam, black is X-transverse width of RMS beam, blue is Y-transverse envelope of RMS beam and the red is the beamline aperture.

6.4.3 Linac sensitivity to RF amplitude errors

Similarly, to find out the limitation of the RF field amplitude fluctuations we implemented the error values in Table 6.1 and increased the RF field amplitude errors by a 0.1% step size until beam losses occurred. It turned out that the linac maximum tolerance to RF field amplitude error is ≤ 2.4%. Table 6.4 summarizes the linac maximum tolerance values to misalignments, RF phase and field fluctuations for no beam losses occurrence.

Parameter	Unit	Tolerance	Distribution Static / Dynamic
Cavity displacement	[mm]	±1.0	Uniform
Quadrupole displacement	[mm]	±0.15	Uniform
Element rotation	[mrad]	±4.0	Uniform
RF phase fluctuation	[Degree]	±1.4	Uniform/ Gaussian
RF field fluctuation		±2.4%	Uniform/ Gaussian

Table 6.4: Linac maximum tolerance values for no beam losses occurrence

6.4.4 Ion dynamic crossing the stable and unstable regions of the longitudinal acceptance

In order to, further understand the implication of the longitudinal acceptance, we placed an ion of charge state 80 at the tail of the longitudinal acceptance and tracked the ion evaluation in the longitudinal phase-space as shown in figure 6.20. It shows that the ion crossed the stable region to the unstable one a few times and the ion was still transported to the linac end.

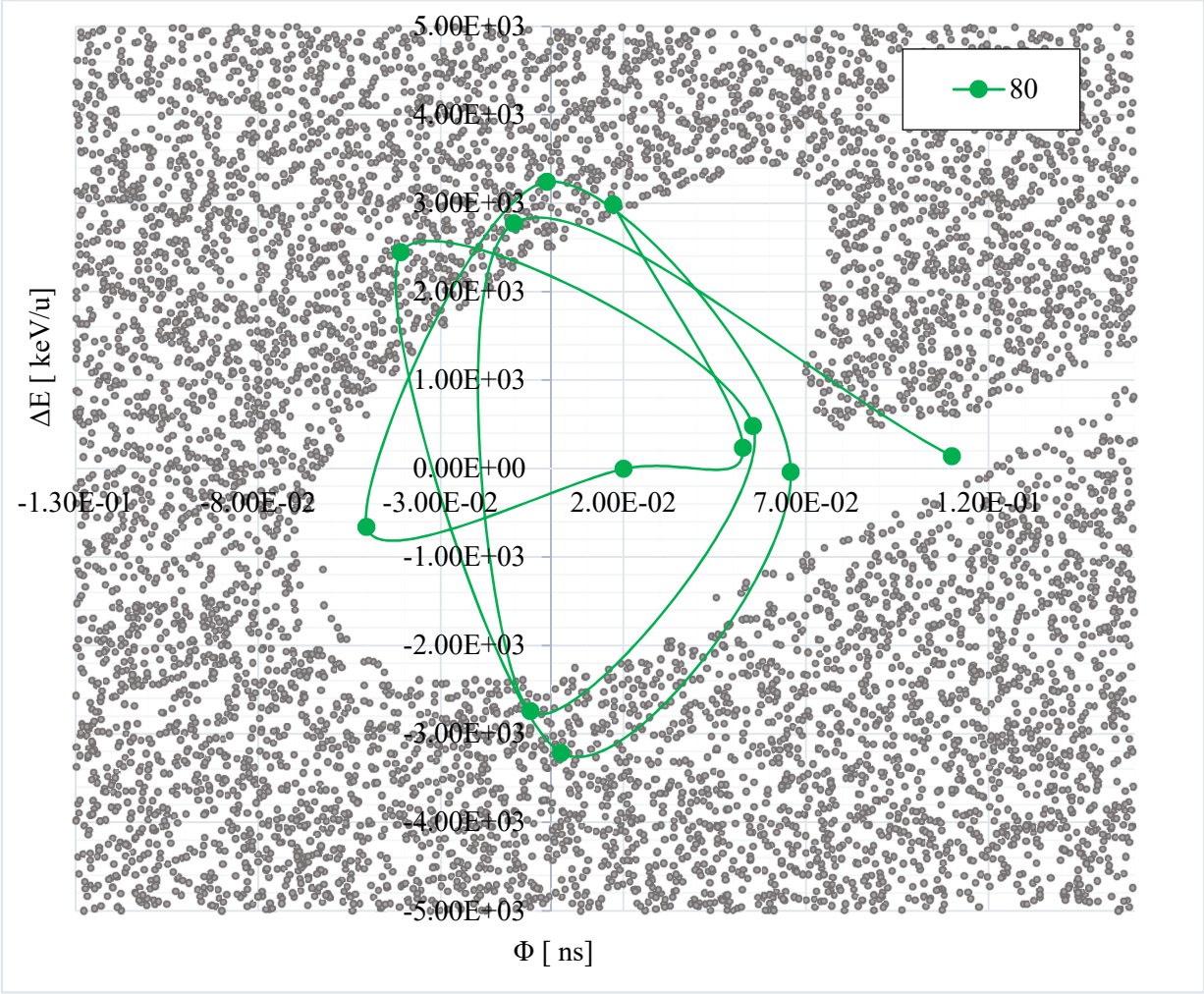

Figure 6.20: An ion of charge state 80 placed in the tail of the longitudinal acceptance was tracked in the longitudinal phase-space.

6.4.5 Ion dynamics in the unstable regions of the longitudinal acceptance

To further explore the threshold at which the ion is considered to be lost in longitudinal phase-space, we placed two ions, one with charge state of 76 in red in the unstable region (above the acceptance) and another ion with charge state of 80 in the unstable region blue (below the acceptance) as shown in figure 6.21. The two ions were injected to the linac and then their motion in the longitudinal phase-space was tracked.

Since the two ions were in the unstable region, i.e. there is not restoring force to make the ions oscillate around the synchronous ion, i.e. the ions would be eventually over or under focused and then they would hit the beam aperture and be considered lost.

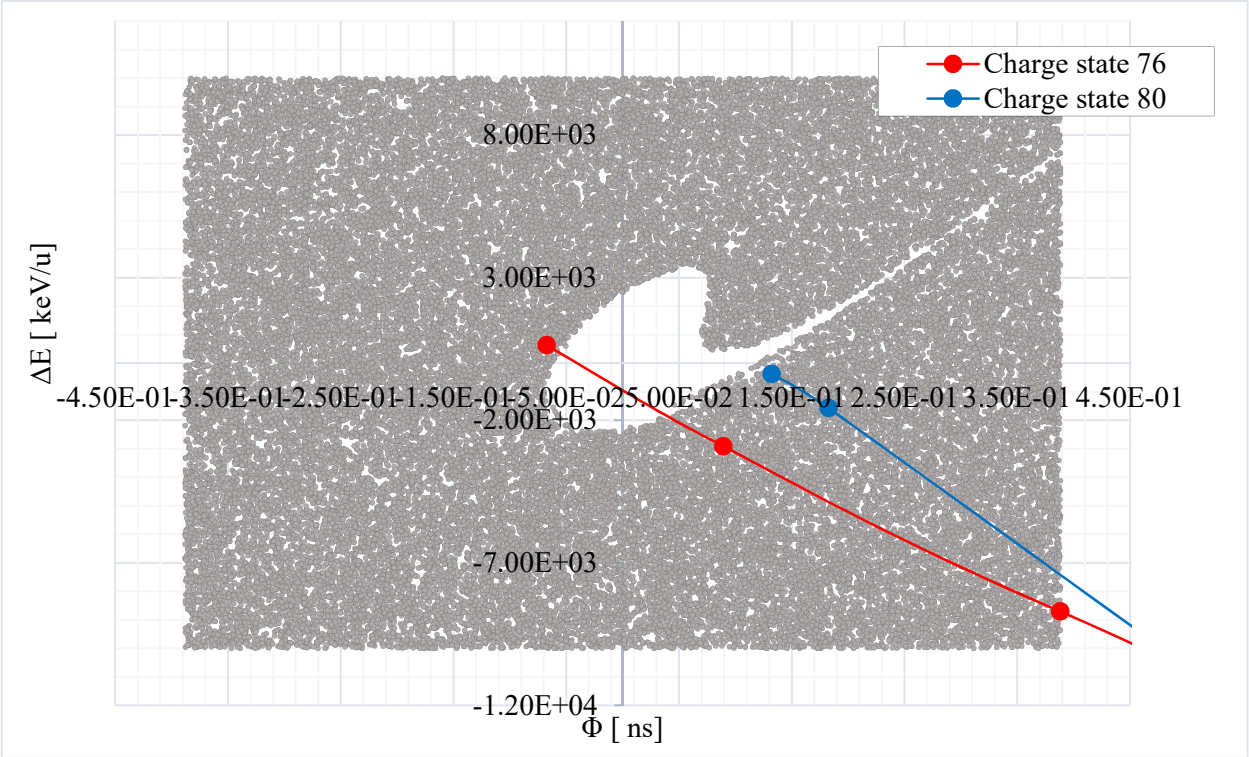

Figure 6.21: Two ions of charge states 76 and 80 placed above and below the longitudinal acceptance were tracked in the longitudinal phase-space.

6.5 1288 MHz linac cryogenics

The RF dynamic load (P_{loss}) is calculated from the equation (6.4).

$$\boldsymbol{P_{loss}\,[W] = \frac{L_{eff}^2}{(R/Q)}\,\frac{E_{acc}^2}{Q_o}} \qquad (6.4)$$

Here, for our design, (R/Q) =262.6 Ω, $L_{eff} \equiv \frac{\beta_g N \lambda}{2}$, β_g= 0.61, λ = 0.233 m, N=6 and L_{eff} = 0.426 m.

When input these numbers into equation (6.4), RF dynamic loss/cavity at E_{acc}= 25 MV/m is calculated as in equation (6.5).

$$\boldsymbol{P_{loss} = \frac{4.32\times10^{11}}{Q_0}} \quad (6.5)$$

If Q_o= 4x10^{10}, P_{loss} = 10.8 W/ cavity. The total with the nitrogen doping technology, the cavity cryogenic heat load can be lowered significantly. The linac dynamic heat load for the 1288 MHz linac is calculated for varies cavity intrinsic quality factors, Q_0. As expected and shown in Fig. 22, higher cavity quality factor reduces the dynamics heat of the linac.

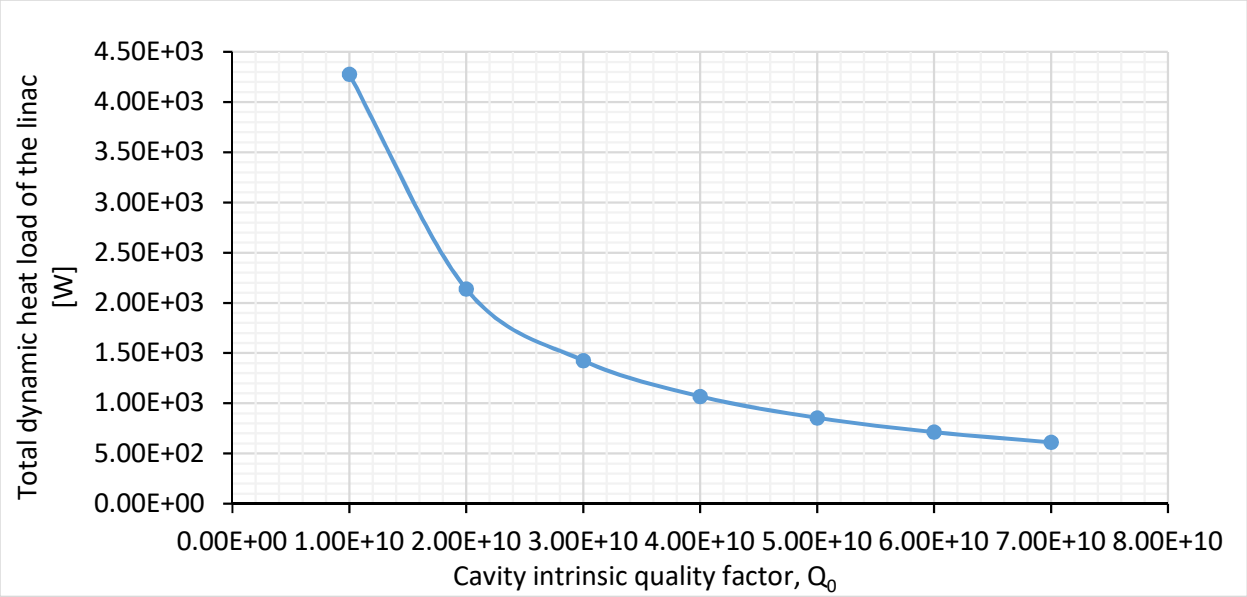

Figure 6.22: 1288 MHz linac's heat load calculations for different cavity quality factors.

6.6 1288 MHz linac beam dynamics summary

According to the above results, we conclude that the 1288 MHz linac longitudinal acceptance is sufficient for multi-charge-state beams acceleration. The beam initial

distribution was taken from FRIB linac output where a solid charge stripper (carbon foil) was used to increase uranium-238 charge states from 33 and 34 up to five charge states (76, 77, 78, 79, and 80). The space-charge force was neglected in the simulation due to the beam current is low (less than 1 mA). Beam losses studies were performed for 300 seeds error trials and confirmed that no beam losses were observed. End-to-end beam losses studies with more statistics is expected to confirm that the beam loss below 1 W/m for accelerator maintenance.

7 High Efficiency SRF Linac Strategy

7.1 RF superconductivity

7.1.1 RF superconductivity theory (BCS surface resistance)

The DC superconductivity case has zero resistance, however in the RF superconductivity, there is a fundamental surface resistance and this resistance decreases as temperature decreases for $\boldsymbol{T \leq T_c}$. That is because electrons have inertia, i.e. they cannot synchronize their motion with RF-wave, which leads to the RF time-dependent magnetic field in the RF surface will induce electric fields (according to Faraday's law) that cannot be screened by the superconducting electrons' electric fields. Thus, the unpaired electrons (normal conducting electrons) will experience electric fields at $\boldsymbol{T > 0}$, i.e. resistance will arise. In 1934, John Bardeen introduced a two-fluid model to explain superconductivity. He pointed out that the two-fluid model description of the superfluity in liquid helium by Lev Landau can be extended to explain superconductivity. He published a paper with the title "TWO-FLUID MODEL OF SUPERCONDUCTIVITY". In this paper, he assumed that the total number of the superconductor's electrons density, $\boldsymbol{n}$ is the sum of the superconducting electrons (cooper pairs) density, $\boldsymbol{n_s}$ and the (unpaired) normal conducting electrons density, $\boldsymbol{n_n}$ as described by equation (7.1) [24].

$$\boldsymbol{n = n_s + n_n} \tag{7.1}$$

The RF current can be represented by the equation (7.2).

$$J = J_0 e^{i\omega t} \tag{7.2}$$

Then the total surface current is the sum of the superconducting (supercurrent) current and the normal conducting current, which can be written in terms of the electric conductivity (in the complex plane) and the electric field as described in equation (7.3). The normal conducting current is treated as the normal conductor's current from Ohm's law and Drude's model for conducting electrons. Its surface current can be expressed in terms of the electric field, $\vec{E}$ and the electric conductivity, σ_n as $\vec{J} = \sigma_n \vec{E}$.

$$J = J_n + J_s = \sigma_n E_0 e^{-i\omega t} - i\sigma_s E_0 e^{-i\omega t} \tag{7.3}$$

Here, σ_n is the electrical conductivity of the normal conducting electrons, which can be expressed by $\sigma_n = \frac{n_n e^2}{m_e \tau}$, where m_e is the mass of an electron, e is the electron charge and τ is the normal electrons scattering time. σ_s is the electrical conductivity of the superconducting electrons, which can be expressed by $\sigma_s = \frac{n_s e^2}{m\omega}$ where m is the mass of cooper pair ($2m_e$), cooper pair charge ($-2e$) and ω is the applied RF frequency. J_s is 90 ° out of phase with RF electric field which means no power loss that is represented in a complex form, however at high enough electric field some cooper pairs start to break due to the heat accumulated during electrons collisions with impurities, lattice imperfections, and electrons themselves which increases normal electrons density, i.e. cooper pairs conductivity decreases. The supercurrent, J_s flows with zero resistance and it obeys the London equations (7.4) and (7.5) equations. For RF superconductivity case, the time-dependent magnetic field of the RF wave penetrates the superconductor surface, which induces electric fields that act on the normal conducting electrons. The depth, at which the RF wave penetrates the superconductor surface, is called the skin

depth, $\boldsymbol{\delta}$ where the majority of the surface current about (~63% of total current) is carried and it can be expressed as in equation (7.6).

$$\frac{\partial}{dt}\vec{J}_s = \frac{1}{\mu_0 \lambda_L^2}\vec{E} \tag{7.4}$$

Here, equation (7.4) says that the supercurrent flows with zero resistance even. Here, $\boldsymbol{\lambda_L}$ is London penetration depth.

$$\nabla \times \vec{J}_s = \frac{1}{\lambda_L^2}\vec{H} \tag{7.5}$$

Here, equation (7.5) says that the source of the supercurrent source is the change in the applied magnetic field of the RF wave, i.e. the induced electric field in the superconductor drives the supercurrent. The RF magnetic field penetrates the cavity (conductor) surface with a thin depth called the skin depth, $\boldsymbol{\delta}$ and that induces an electric field on the cavity surface results surface current. Majority of the surface current flows in this skin depth, which results power dissipation due to the cavity surface resistance. The skin depth depends on the cavity frequency and the cavity conductivity as described in equation (7.6)

$$\delta = \sqrt{\frac{2}{\sigma\omega\mu_0}} = \sqrt{\frac{2}{(\sigma_n - i\sigma_{s)}\omega\mu_0}} \tag{7.6}$$

Then the surface resistance, $\boldsymbol{R_s}$ of an RF superconductor can be written in terms of electric conductivity and London penetration depth, $\boldsymbol{\lambda_L}$ as in equation (7.7). The London penetration depth, $\boldsymbol{\lambda_L}$ is the length at which the magnetic field, $\boldsymbol{B_{inside}}$ inside the

superconductor surface falls to $\frac{1}{e}$ of the RF applied magnetic field, $\boldsymbol{B_a}$ and it can be expressed by equation (7.8).

$$\boldsymbol{R_S = \frac{1}{\lambda_L}\frac{\sigma_n}{\sigma_n^2 - \sigma_s^2}} \tag{7.7}$$

$$\boldsymbol{\lambda_L = \sqrt{\frac{\varepsilon_0 mc^2}{n_s e^2}}} \tag{7.8}$$

For RF frequencies, at temperature, $\boldsymbol{T \leq T_c}$ we can use the approximation $\boldsymbol{\sigma_n \ll \sigma_s}$. Then the equation (7.7) is simplified to the equation (7.9).

$$\boldsymbol{R_S \simeq \frac{1}{2}\sigma_n \omega^2 \mu_0^2 \lambda_L^3} \tag{7.9}$$

Note here,

5. The superconductor surface resistance is directly proportional to the electric conductivity of the normal conducting electrons and the electric conductivity of the normal conducting electrons, $\boldsymbol{\sigma_n \propto l}$, i.e. the surface resistance depends on the mean free path, $\boldsymbol{l}$ of the normal conducting electrons. Figure 7.1 shows that there is a minimum occurs at about ($\boldsymbol{l}$ = 30-40 nm) in the surface resistance and the mean free path, $\boldsymbol{l}$ of the normal conducting electrons plot [25]. We will see later in the sub-section 7.2 how this mean free path can be optimized such that it minimizes the superconductor's surface resistance.
6. The superconductor surface resistance is proportional to the frequency squared.

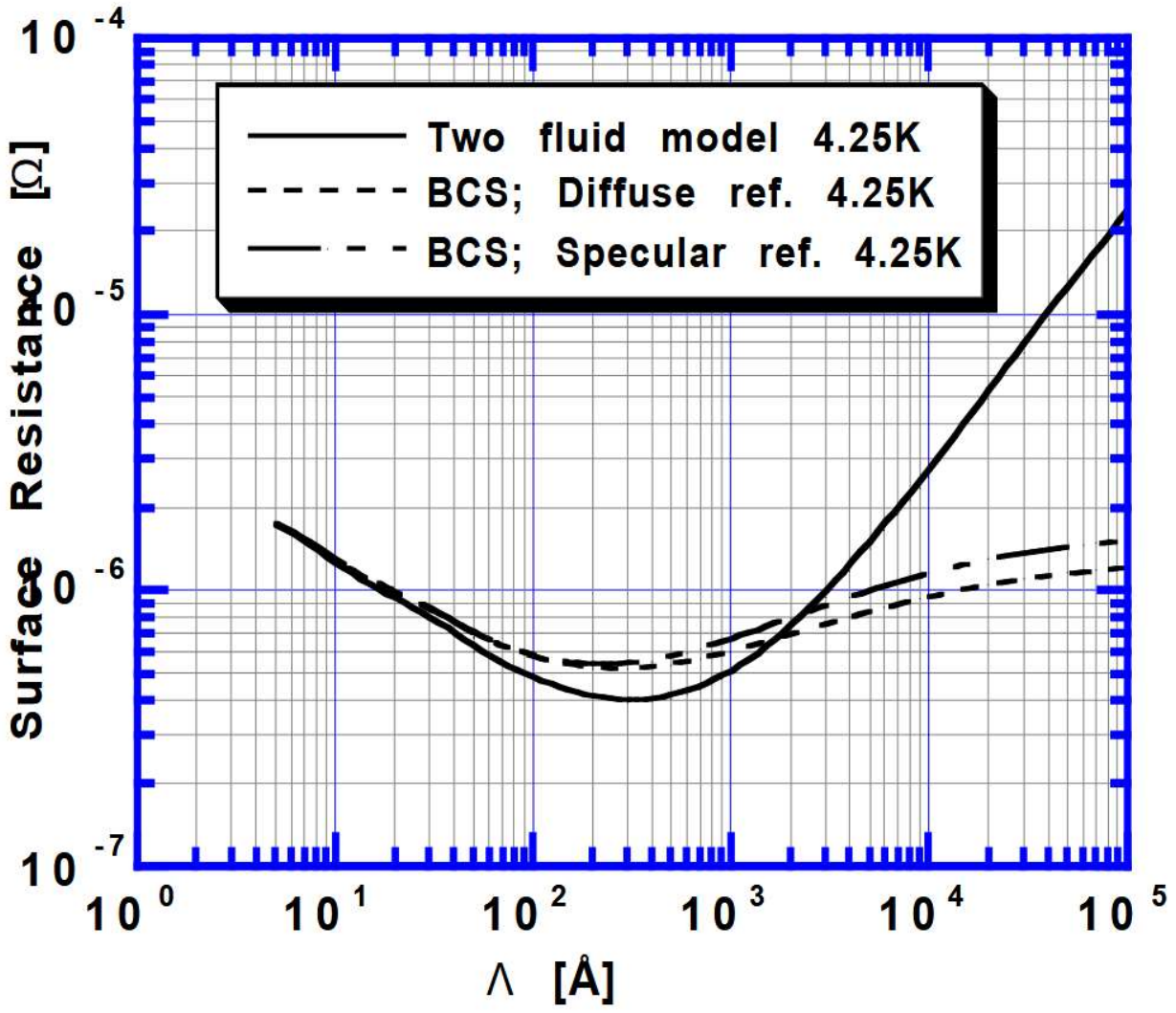

Figure 7.1: shows that there is a minimum occurs at about ($\boldsymbol{l}$ = 30-40 nm) in the surface resistance and the mean free path, $\boldsymbol{l}$ of the normal conducting electrons plot.

In 1958, John Bardeen, Leon Cooper, and John Robert Schrieffer developed a theory to explain superconductivity, which was named after them, by Bardeen-Cooper-Schrieffer theory (BCS theory) [26]. The BCS theory describes the superconductivity in a microscopic level. It basically assumes that for a superconductor, there is a force of attraction between electrons through phonon interaction to overcome the coulomb

repulsion at a temperature, $\boldsymbol{T \leq T_c}$ (**critical temperture**). This force of attraction can be explained by the interaction of electrons with lattice vibration (phonons) including the coulomb effect, which leads to forming electron pairs (cooper pairs) that flow with zero resistance. These cooper pairs (bosons-like) obey the Bose-Einstein condensation statistics. In the BCS theory, the total superconductor surface current is defined in terms of the normal conducting current, the supercurrent and the vector potential as in the equation (7.10).

$$\vec{\boldsymbol{J}}(\boldsymbol{r}) = \frac{\mathbf{3}}{\mathbf{4}\pi^{\mathbf{2}}\boldsymbol{v_F}\hbar\boldsymbol{\lambda_L^2}} \int_{\boldsymbol{V}} \frac{\vec{\boldsymbol{R}}[\boldsymbol{I}(\boldsymbol{\omega},\boldsymbol{R},\boldsymbol{T})\vec{\boldsymbol{R}}\cdot\vec{\boldsymbol{A}}(\boldsymbol{r})e^{-\frac{\boldsymbol{R}}{\boldsymbol{l}}}]}{\vec{\boldsymbol{R}}^{\mathbf{4}}} \boldsymbol{dr'} \tag{7.10}$$

Here, $\vec{\boldsymbol{R}}$ is $(\boldsymbol{r}-\boldsymbol{r'})$, $\vec{\boldsymbol{A}}(\boldsymbol{r})$ is the vector potential, and $\boldsymbol{I}(\boldsymbol{\omega},\boldsymbol{R},\boldsymbol{T})$ is the decay function at a distance $\vec{\boldsymbol{R}}\sim\boldsymbol{\xi_0}$, where $\boldsymbol{\xi_0}$ is the cooper pair coherent length.

For $\boldsymbol{T} < \frac{\boldsymbol{T_c}}{\mathbf{2}}$ and $\boldsymbol{\omega} < \frac{\Delta}{\hbar}$ case, the BCS surface resistance, $\boldsymbol{R_{BCS}}$ can be approximated as in equation (7.11) [24].

$$\boldsymbol{R_{BCS}} \simeq \boldsymbol{\mu_0^2\omega^2\lambda^3\sigma_n} \frac{\Delta}{\boldsymbol{k_BT}} \boldsymbol{ln}\left(\frac{\mathbf{2.246}\boldsymbol{k_BT}}{\hbar\boldsymbol{\omega}}\right) \boldsymbol{e}^{-\frac{\Delta}{\boldsymbol{k_BT}}} \tag{7.11}$$

Here, Δ is cooper pair's energy gap, $\boldsymbol{\lambda}$ is the effective penetration depth, which depends on the mean free path, $\boldsymbol{l}$ and the cooper pair coherent length, $\boldsymbol{\xi_0}$ that can be approximated as in equation (7.12) and $\boldsymbol{k_B}$ is Boltzmann constant.

$$\boldsymbol{\lambda} \approx \boldsymbol{\lambda_L}\sqrt{\mathbf{1}+\frac{\boldsymbol{\xi_0}}{\boldsymbol{l}}} \tag{7.12}$$

Note here,

1. BCS surface resistance, $\boldsymbol{R_{BCS} \propto \omega^2}$,
2. $\boldsymbol{R_{BCS} \propto \lambda^3}$,
3. $\boldsymbol{R_{BCS} \propto \sigma_n \propto l e^{-\frac{1.86T_c}{T}}}$,
    1. For $\boldsymbol{l \ll \xi_0}$ case, $\boldsymbol{R_{BCS} \propto l^{-1/2}}$,
    2. For $\boldsymbol{l \gg \xi_0}$ case, $\boldsymbol{R_{BCS} \propto l}$.
4. $\boldsymbol{R_{BCS} \propto \frac{1}{T}}$,
5. $\boldsymbol{R_{BCS} \propto \Delta}$.

For 1.3 GHz niobium SRF cavity case, the typical surface resistance parameters can be found in Table 7.1 from the reference [27].

Parameter	Unit	Value
Frequency	[GHz]	1.3
Critical Temperature, $\boldsymbol{T_c}$	[K]	9.2
Operating Temperature	[K]	2.0
Coherence length, $\boldsymbol{\xi_0}$	[nm]	38
London penetration depth, $\boldsymbol{\lambda_L(0)}$	[nm]	40
Gap energy, $\Delta(\boldsymbol{0})/\boldsymbol{k_B T_c}$		1.86
Mean free path, $\boldsymbol{l}$	[nm]	500
Mean free path, $\boldsymbol{l}$, (clean limit)	[nm]	>500
Mean free path, $\boldsymbol{l}$, (dirty limit)	[nm]	<10
DC resistivity, $\boldsymbol{\rho_n}$ at (300K)	[Ω]	14.5×10^{-8}
RF resistance, $\boldsymbol{R_{surf}}$ at (10K)	[Ω]	1.5×10^{-3}
Residual Resistance Ratio, $\boldsymbol{RRR = \frac{\rho_{(300K)}}{\rho_{(10K)}}}$		>300

Table 7.1: Typical BCS surface resistance parameters for 1.3 GHz SRF niobium cavity

7.1.2 SRF residual surface resistance

The residual surface resistance, $\boldsymbol{R_{res}}$ of SRF cavities tends to saturate at low temperature ($\boldsymbol{T = 1.5K}$), i.e. it is independent of temperature in that limit. It is typically in the order of 1-10 n Ω depending on the purity of the superconductor in terms of flux trapping and surface contamination of 1.3 GHz SRF cavities.

The sources of surface residual resistance are assumed to be:

1. Since there is, a natural oxide layer of Nb_xO_y covered on the SRF cavity surface. Thus, there will be dielectric losses at the interface between the dielectric layer and the superconductor bulk.
2. The material impurity, which would lead to trapping magnetic fluxes during the cavity cool-down. The cause of the magnetic flux trapping in SRF cavities can be Earth's magnetic field and the thermos-electric affects from the temperature gradient during the cavity cool-down, which generate magnetic fluxes that are trapped in the normal conducting regions by impurities.
3. Speed of the cavity cool-down can cause a formation of a normal conducting hydride phase that increases the residual resistance. It been demonstrated that the fast cavity cool-down provides higher cavity intrinsic quality factor, $\boldsymbol{Q_0}$ [28].

The total surface resistance, $\boldsymbol{R_{Surf}}$ is the sum of the residual surface resistance, $\boldsymbol{R_{res}}$ and the BCS surface resistance, $\boldsymbol{R_{BCS}}$ which can be expressed in the equation (7.13).

$$\boldsymbol{R_{Surf} = R_{res} + R_{BCS}} \tag{7.13}$$

7.2 Achieving high cavity intrinsic quality factor studies

7.2.1. Nitrogen diffusion technology

It has been demonstrated that the diffusion of nitrogen in cavity surface improves the cavity intrinsic quality factor, $\boldsymbol{Q_0}$ as illustrated in figure 7.2 [29]. It is indicated that the reduction of the electrons mean free path, $\boldsymbol{l}$, i.e. decreasing the electrical conductivity of normal conducting electrons due to nitrogen interstitials (impurity) in SRF cavity surface is the cause of the improvement of the cavity quality factor. In addition, the nitrogen interstitials pin the trapped magnetic vertices such that those magnetic vortices

do not collide with each other and generate heat analogous to Ohmic heating. In 2017, Alex Gurevich and Takayuki Kubo published a paper with the title “Surface impedance and optimum surface resistance of a superconductor with an imperfect surface” they basically explained the nonlinear behavior of the cavity surface resistance is due to imperfect cavity surface and the broadening of the Density Of States (DOS) peaks, see reference [30].

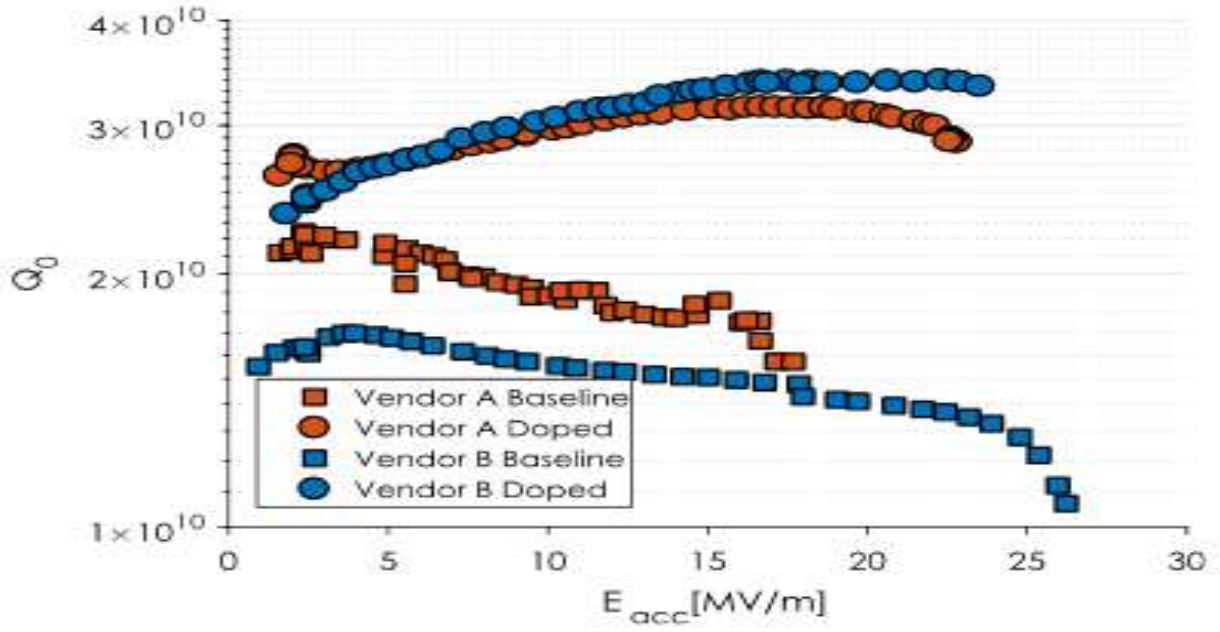

Figure 7.2: Cavity intrinsic quality factor versus accelerating electric field for 1.3 GHz cavity for baseline and nitrogen diffused (doped) cavities vertical tests for two cavities from vendors. [Courtesy: D. Gonnella, Fermi lab].

The nitrogen diffusion recipe can be found in the reference [29], which can be summarized as follows:

1. UHV furnace in vacuum at 800 ℃ for 3 hours (to remove the oxide layers).

2. Nitrogen doping in 26 mTorr of nitrogen gas for 2 min at 800 ℃.
3. Annealing in vacuum for 6 min at 800 ℃.
4. Light EP of 5–7 μ m. To remove niobium nitride (NbN) islands.

The furnace temperature profile for cavity nitrogen diffusion (doping) recipe is shown in figure 7.3.

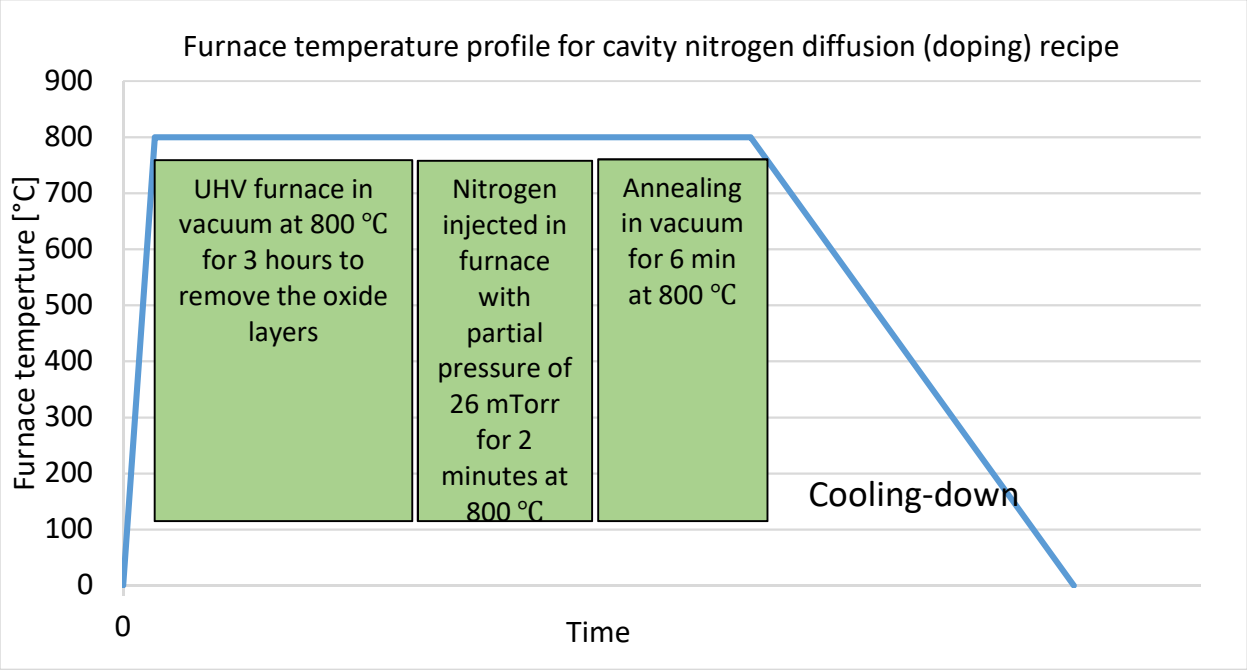

Figure 7.3: Furnace temperature profile for cavity nitrogen diffusion (doping) recipe.

7.2.2. Low temperature baking with nitrogen (infusion) technology

It has been tested that low temperature baking (120-160 ℃) with nitrogen of SRF cavities can improve the cavity intrinsic quality factor, $\boldsymbol{Q_0}$ as shown in figure 7.4 [31]. The low temperature baking with nitrogen for SRF cavities recipe can be found in the reference [31] it is summarized as follows:

1. UHV furnace in vacuum at 800 ℃ for 3 hours (to remove the oxide layers).
2. Nitrogen-low temperature baking (120-160 ℃) in a partial of a 25 mTorr of nitrogen gas for 48 hours. Annealing in vacuum for 6 min at 800 ℃. Note that it was shown that there are still tiny islands of niobium nitride NbN on the SRF cavity surface as the author mentioned which might need an Electro-Polishing (EP) to remove these NbN islands for better cavity performance.

The furnace temperature profile for cavity nitrogen infusion (doping) recipe is shown in figure 7.5.

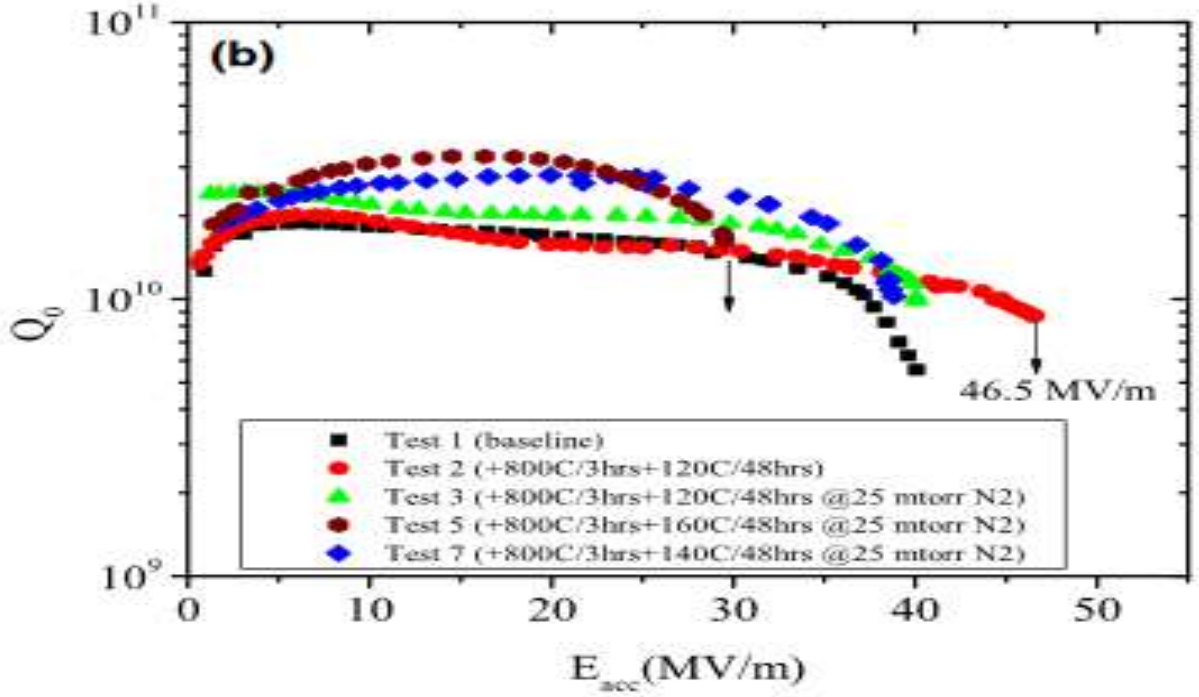

Figure 7.4: Cavity intrinsic quality factor versus accelerating electric field for 1.5 GHz cavity for baseline and low temperature baked with nitrogen vertical tests. Plot Credit: [Pashupati Dhakal, Thomas Jefferson lab].

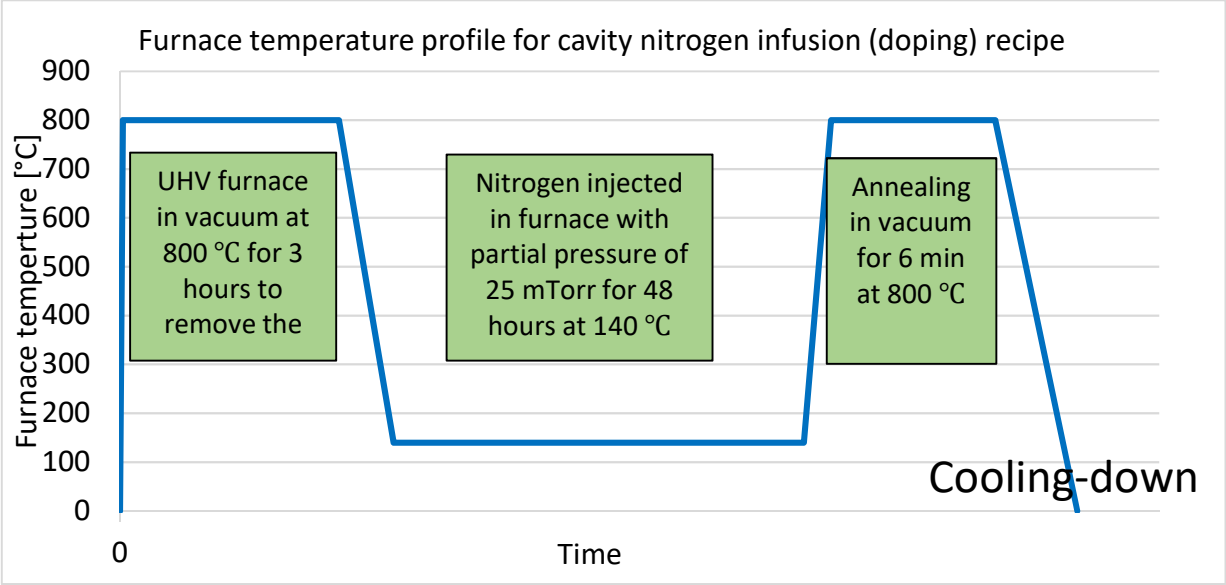

Figure 7.5: The furnace temperature profile for cavity nitrogen diffusion (doping) recipe.

7.2.3. Strategy for cavity high-quality factor, Q_0 and accelerating electric field, E_{acc}

As mentioned in section 7.2.1, the assumption that the role of the nitrogen atoms in improving the cavity high-quality factor, $\boldsymbol{Q_0}$, is that they diffuse between niobium atoms as interstitials which lower the mean free path for the normal conducting electrons and also, nitrogen interstitials pin the trapped magnetic vortices in the RF surface. However, the nitrogen could also make chemical compositions with the niobium, which produce niobium nitride layers/islands with normal conducting phases that need to be removed by Electro-polishing (EP). With that mind, one should notice that since the role of nitrogen to improve the cavity quality factor is that it acts as an interstitial atom in the RF surface then we should search for an element that does not make chemical compositions with the niobium lattice and it has an atom size similar to the nitrogen atom size. Table 7.2 compares nitrogen to neon atoms in terms of the reactivity, magnetism and atom size.

Property	Nitrogen	Neon
Reactivity	Yes	Noble
Magnetism	Diamagnetic	Diamagnetic
Van Der Waals radius [pm]	155	154

Table 7.2: A comparison of nitrogen to neon atoms in terms of the reactivity, magnetism and atom size

Based on the assumptions mentioned earlier, neon seems to be the optimum element for cavity diffusion (doping) to improve the cavity intrinsic quality factor for the following reasons:

1. Neon doping advantage is to have free niobium nitride NbN islands RF surface, i.e. a higher $\boldsymbol{Q_0}$ value and Electropolishing EP is not required after the neon treatment.
2. Neon and nitrogen atoms have similar sizes (Van Der Waals radius).
3. Neon and nitrogen atoms both are diamagnetic, how about flux expulsion during the cool-down?

We proposed an experiment to test our assumption that neon could be the optimum cavity's diffusion element. It is replacing nitrogen by neon and test cavity after the cavity diffusion treatment. In this experiment, we can determine that whether the nitrogen acts as an interstitial or chemically combines with niobium (with superconducting NbN phases) to improve the cavity intrinsic quality factor. We proposed conducting this experiment in Thomas Jefferson Laboratory in February 2019, however they did not want to introduce a new gas in their furnace due to it could affect the furnace performance and that could be very problematic to them since the furnace repair is

costly. Instead, during my visit to Jlab I learned from the SRF accelerator physicist, Pashupati Dhakal nitrogen treatment for SRF cavities and conducted a vertical test for the nitrogen treated cavities. It was a good opportunity for me to learn more on cavity treatments from Pashupati who was the first to discover the effect of nitrogen treatment in improving cavity quality factor in 2014 [32].

7.3 Cavity preparation

We prepared an SRF 1.3 GHz cavity for our cavity neon diffusion experiment proposal to improve the cavity intrinsic quality factor. My advisor Kenji Saito brought this cavity along with a movable coupler from KEK for his R&D as shown in figure 7.6. These cavity parameters are summarized in Table 7.3.

Cavity parameters	Unit	Value
$\boldsymbol{RRR}$		200
$\boldsymbol{R/Q}$		102
$\boldsymbol{G}$	[Ω]	274
E_p/E_{acc}		1.78
H_p/E_{acc}	[mT/MV/m]	4.38
Beam tube diameter	[mm]	80
Inner surface area	[cm^2]	1664
Cavity walls thickness	[mm]	2.5
A weight per 1micron material removal	[g]	1.42

Table 7.3: 1.3 GHz (K-24) cavity parameters

7.4 Cavity testing

7.4.1 Variable coupler calibration for cold test

The variable coupler was calibrated for the cold baseline test for $\boldsymbol{Q_0}$ measurements at room temperature. Table 7.4 summarizes the $\boldsymbol{Q_0}$ measurements at room temperature.

Input coupler parameters	Q_l	Calc Q_0	$Q_{ext\ 1}$	$Q_{ext\ 2}$	Span [MHz]	Input coupler length [cm]
	5635.9	8915.2	15321.9	2.1163E+12	5	12.4

S_{11} [dB]	-11.557
S_{21} [dB]	-84.069
β_1	0.582
β_2	4.2E-09

Table 7.4: Summary the $\boldsymbol{Q_0}$ measurements at room temperature

Here, the coupling parameters in Table 7.4 were calculated and measured as follow:

1. Calc Q_0 is the calculated Q_0 at room temperature = $(1+\beta_1+\beta_2)Q_l$
2. $\boldsymbol{\beta_1} = \frac{1-10^{\frac{S11}{20}}}{1+10^{\frac{S11}{20}}}$
3. $\boldsymbol{\beta_2} = \frac{10^{\frac{S21}{10}}}{1-10^{\frac{S21}{10}}-10^{\frac{S11}{10}}}$
4. $Q_{ext\ 1}$ is the input coupler quality factor = $\boldsymbol{Q_0 / \beta_1}$

5. $Q_{ext\ 2}$ is the pickup coupler quality factor = $\boldsymbol{Q_0 / \beta_2}$
6. Q_{ext2} is 100 times higher than the desired Q_0 at 2 K is fulfilled
7. Expected Q_0 at 2K about $1X10^{10}$
8. L is defined as the length between the cavity flanges to the coupler flange as illustrated in figure 7.4.
9. Near matching (critical coupling) L = 15.7 cm, The indium seal thickness of < 0.5 mm will be taken into account
10. The change in Q from 15.6 to 15.7 cm is $4.4\times10^{9.}$ The change in Q from 15.7 to 15.8 cm is 4.4×10^{9} as well. In Table 7.5, the desired Q versus input coupler antenna's lengths for the movable coupler for 4 K and 2 K measurements are calculated.

Here, $\boldsymbol{\beta_1}$ is the input coupler coupling coefficient, S_{11} is a measure of reflected signal from port 1, S_{21} is a measure of the transmitted signal from port 1 to port 2 and $\boldsymbol{\beta_2}$ is the pickup port (port 2) coupler coupling coefficient.

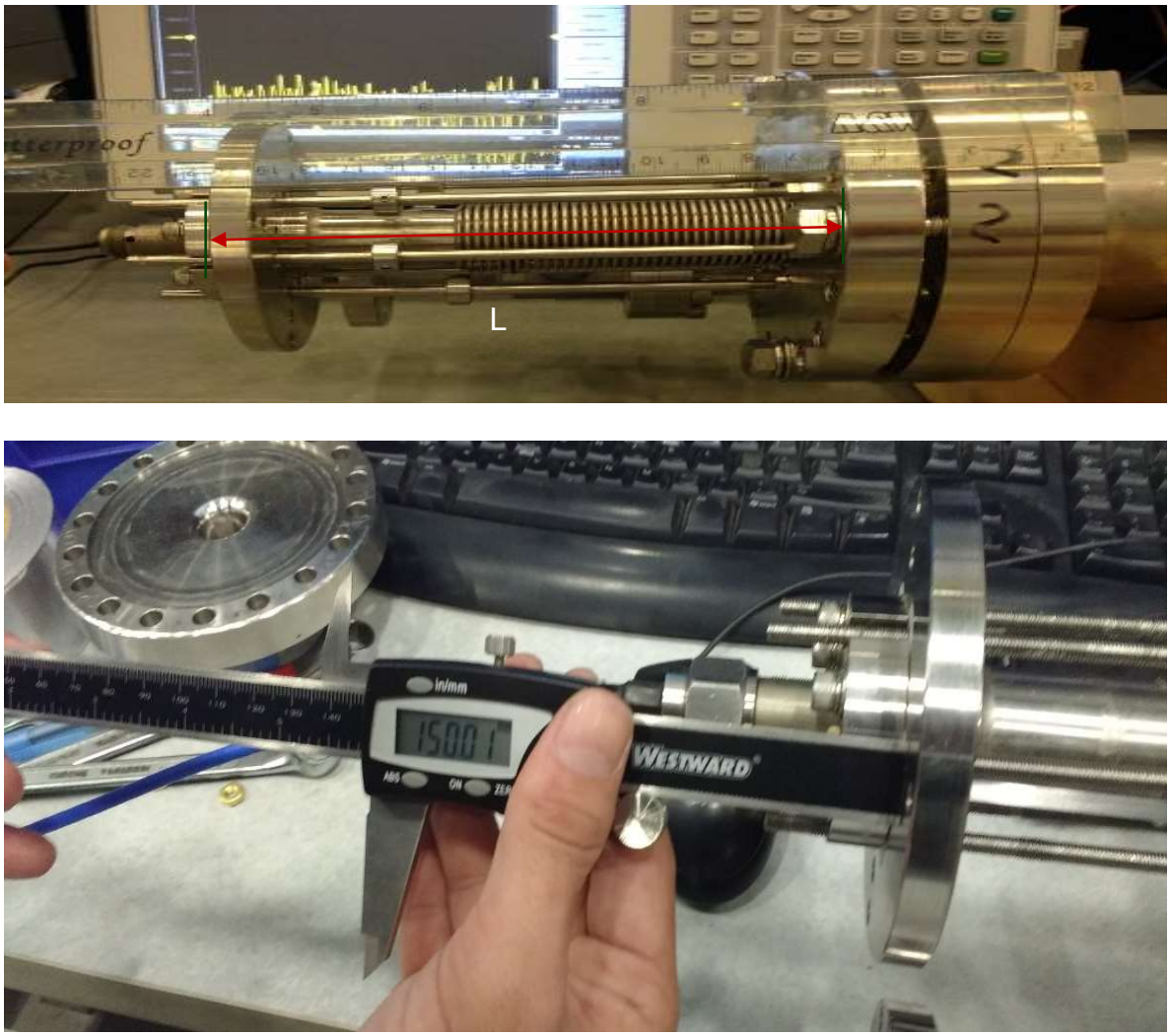

Figure 7.6: Movable coupler for 1.3 GHz cavity.

A Vernier was utilized to measure the input coupler length with an uncertainty of ±25 μm as shown in figure 7.6. Q external 2 versus input coupler antenna's lengths for the movable coupler is plotted in figure 7.5. This measurement was repeated 3 times.

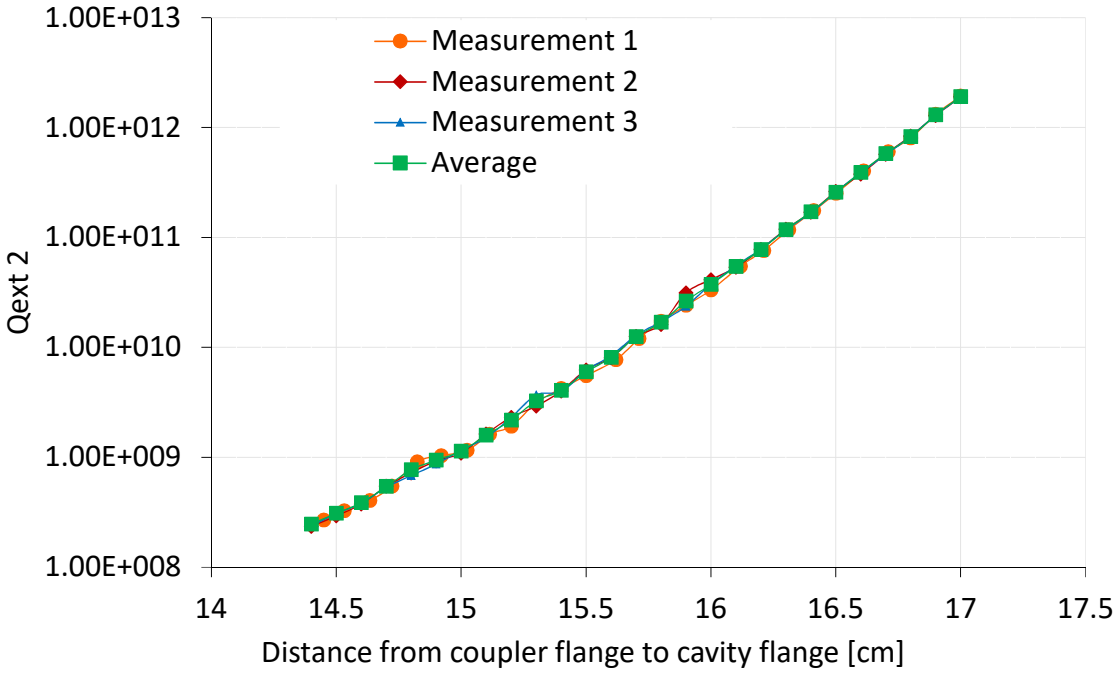

Figure 7.7: Q external 2 versus input coupler antenna's lengths for the movable coupler.

Temperature [K]	Expected Q_0	L [cm]
4	3.00E+08 ± 1.37E+07	15.7
2	1.25E+10 ± 4.37E+09	15.7
2	5.98E+09 ± 2.08E+09	15.5
2	8.06E+09 ± 4.42E+09	15.6
2	1.25E+10 ± 4.37E+09	15.7
2	1.69E+10 ± 9.49E+09	15.8
2	2.63E+10 ± 1.10E+10	15.9
2	3.74E+10 ± 1.71E+10	16.0

Table 7.5: The desired Q versus input coupler antenna's lengths for the movable coupler for 4 K and 2 K measurements

7.4.2 Cavity preparation for cold test

The cavity was electro-polished (EP) with 150 microns at KEK. It was inspected at a FRIB by Jesse Craft as shown in figure 7.7. He showed that there is pits and bumps at the cavity drift tube as shown in the top side of the figure 7.6 and he reported pits at the electron beam welding of the cell equator shown in the bottom of figure 7.6. We assumed that they were not going to impact cavity performance, thus we shipped the cavity to prepare it for vertical cold test. The cavity processed for baseline test at Jlab as follows:

1. 30 µm electro-polished (EP),
2. High Pressure Water Rinsing HPR and dried overnight,
3. Assembly and pumping for 1 day,
4. Cool-down and RF vertical test.

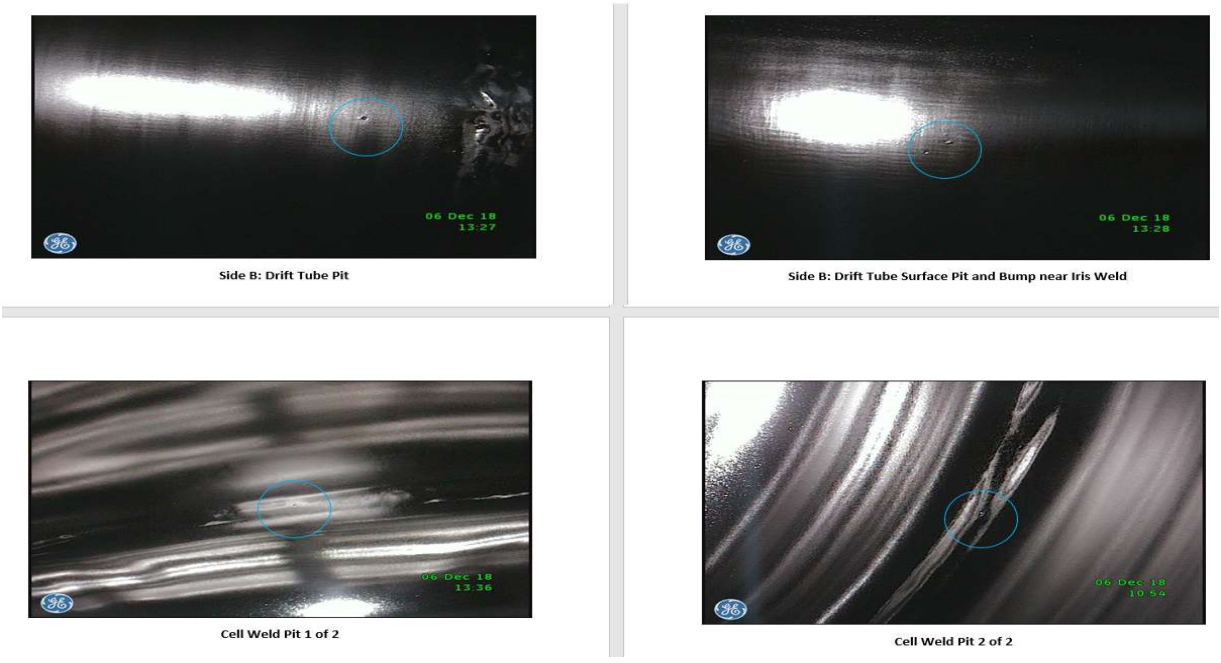

Figure 7.7: Cavity inspection via a camera located the pits and bumps.

7.4.3 Jlab Low Level RF Control (LLRF) vertical test setup

The purpose of this test is to measure the cavity intrinsic quality factor, Q_0 versus the accelerating electric field, E_{acc}.

In a typical RF vertical test, one can measure the following parameters:

1. Forward RF power, P_f, which can be measured via a power meter,
2. Reflected RF power, P_r,
3. Transmitted RF power out any of the other ports, P_t,
4. Cavity energy decay time, τ during the shut off power source, which determines the loaded quality factor. The Q_L is defined the effective quality factor of the cavity. It is the total stored energy in cavity divided by the total power loss in cavity and walls per once cycle for 2 ports system, and then the Q_L is expressed as in equation (7.12). One can use a Vector Network Analyzer (VNA) to measure the energy decay of 1/e decay time, τ of the reflected or transmitted powers and obtain the $Q_L = 2\,\pi\, f_0\, \tau$ or one can use the VNA to measure the cavity bandwidth resonance, BW at -3 dB of the full bandwidth then $Q_L = f_0 / BW$.

$$\boldsymbol{Q_L} = \frac{\boldsymbol{\omega U}}{\boldsymbol{P_{diss}+P_{emit}+P_t}} \tag{7.14}$$

Here, $\boldsymbol{P_{diss}}$ is the dissipated power on cavity walls, $\boldsymbol{P_{emit}}$ is the emitted power from cavity port and $\boldsymbol{P_t}$ is the transmitted power through port 2.

Once we have the measured RF parameters, one can calculate the following parameters:

1. Port 1 coupling coefficient, $\boldsymbol{\beta_1}$, is the strength of coupling of port 1. It is expressed as in equation (7.13),

$$\boldsymbol{\beta_1 = (1 + \beta_2)\beta_1^*} \tag{7.15}$$

Where $\boldsymbol{\beta_1^* = \frac{1 \mp \sqrt{P_{in}/P_r}}{1 \pm \sqrt{P_{in}/P_r}}}$.

Three cases for cavity ports response during the forward power shut off can be described as follows:

1. Under coupled case (weakly coupled): $\boldsymbol{\beta < 1}$, it is where most of the power is reflected. The lower sign in equation (7.13) is considered.

2. Over coupled case (strongly coupled): $\boldsymbol{\beta > 1}$, it is where the emitted power by cavity large. The upper sign in equation (7.13) is considered.

3. Critically coupled case (matched): $\boldsymbol{\beta = 1}$, it is where the emitted power is equally to the reflected power. It is good to test cavities in this case (near critical coupling), due to it would require a small additional power to achieve the desired fields with less power consumption, i.e. very small reflected-power.

2. Port 2 coupling coefficient, $\boldsymbol{\beta_2}$, is the strength of coupling of port 2. It is expressed as in equation (7.14),

$$\boldsymbol{\beta_2 = \frac{Q_0}{Q_t}} \tag{7.16}$$

3. Cavity intrinsic quality factor, Q_0 can be calculated as in equation (7.15),

$$\boldsymbol{Q_0 = (1 + \beta_1 + \beta_2)Q_L} \tag{7.17}$$

4.Stored energy in cavity, U which enables us to calculate the accelerating electric field, E_{acc} as expressed in equation (7.16).

$$\boldsymbol{E_{acc} = \sqrt{Q_0 P_{diss} \frac{R/Q}{L}}} \tag{7.18}$$

Here, L is the cavity effective length.

The theory and experiment of the RF test systems for SRF cavity at Jlab, can be found in the reference [33] and the vertical test setup can be summarized as follows:

1. RF source

In the case of testing cavity performance without beam, Low Level RF system is utilized. In this case, one does not need to fix the RF frequency nor tune the cavity to a particular frequency to match the beam frequency, instead one let the LLRF system follows the cavity resonant frequency and adjust the RF source frequency accordingly.

2. Transmitted power network

The signal of the transmitted power by the cavity field range is in order of 10 microwatts to 100 milli-watts. A directional coupler is utilized to take a sample from the transmitted power and send it to the power measurement network. Then power is transmitted through two circulators to make sure that the Voltage Standing Wave Ratio (VSWR) is minimized at the circuit input. The transmitted power network system is shown in the top left side of LLRF control system block in figure 7.8.

3. Voltage Control Oscillators in Phase Locked Loops, VCO-PLL system

The VCO-PLL is used to drive the RF signal in the cavity via Phase Locked Loops PLL. In the VCO-PLL system, a low noise amplifier (LNA) is utilized to make sure that the RF

input signal to the mixer is not under power limit or over driven. VCO-PLL system is shown in the top right side of the LLRF control system in figure 7.8.

4. Amplitude and Phase Control

The VCO output is directed to the amplitude and phase control system. A circulator is utilized make sure that the frequency change is minimized because of impedance. Directional couplers are utilized in this circuit to couple the power out for the mixer oscillator and the frequency counter. The amplitude and phase control system is illustrated in the bottom right side of the LLRF control system in figure 7.8. A computer program is utilized to control the forward power amplitude and phase.

5. Power Meter Interface

Power meters are used to measure the transmitted and reflected powers at the points of interest in the LLRF system.

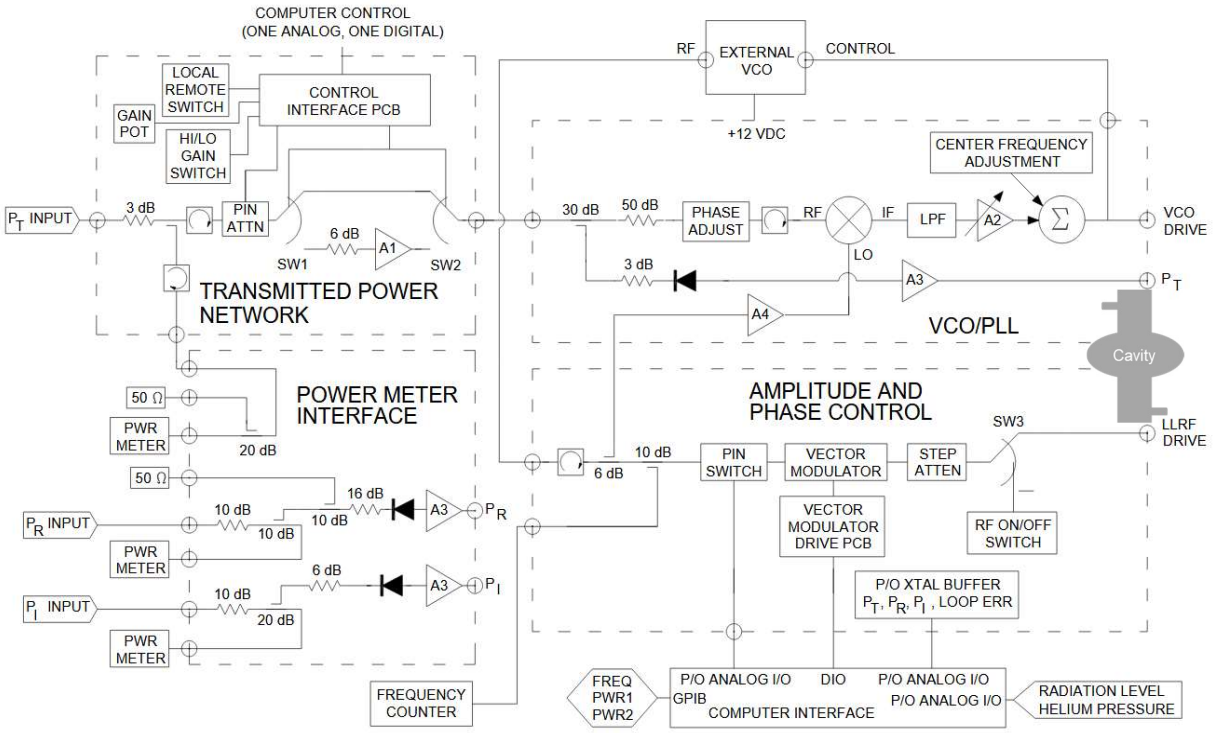

Figure 7.8: Low Level RF (LLRF) control system block at Thomas Jefferson Laboratory.

7.4.4 Cable Calibrations

In order to obtain precise measurement results in cavity vertical testing, one needs to consider the RF cables losses. In general, to calibrate an RF cable, we can use a Vector Network Analyzer (VNA) with its calibration kit. The calibration procedure of an RF cable can be performed as follows:

1. Connect the RF cable to the VNA port and follow calibration on the VNA screen
2. Connect the other end of RF cable to “OPEN” (means open circuit) from the calibration kit
3. Remove the “OPEN” from the RF cable’s end and then connect “SHORT” from the calibration kit

4. Remove the “SHORT” from the RF cable’s end and then connect “LOAD” (50 ohm resistor) from the calibration kit
5. Then remove the “LOAD” from the RF cable, then connect the RF cable to the pick cable via “PASS” from the calibration kit
6. Cable is calibrated.

For cavity cold testing, some cables cannot be reached because they are in the Dewar. That makes the cable calibration complicated. To conduct precise measurements for the cavity performance one needs to consider the RF cable losses and consider them in the cavity quality factor and the accelerating gradient calculations. Figure 7.9 shows the diagram of cavity cabling system in JLab. To do this, one can follow cable calibrations procedure as described below:

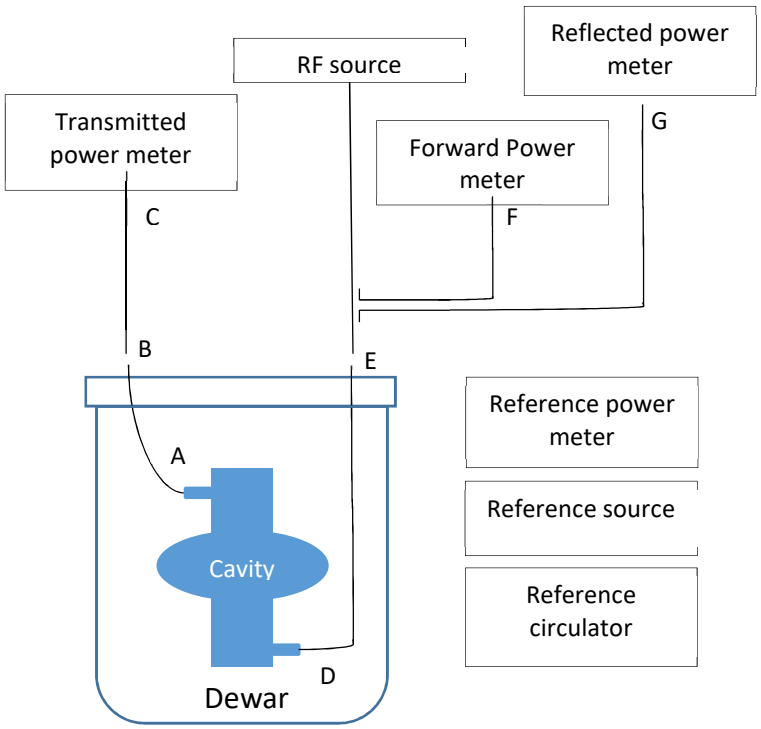

Figure 7.9: Vertical test cavity in Dewar cabling system.

Transmitted power cables calibrations:

1. Point A to point C calibration, measure one way loss of cable B-C
    1. Measure the reference source power (P1),
    2. Connect B-C,
    3. Measure power with the transmitted power meter (P2),
    4. One-way loss (P1-P2) in dB.

2. Two-way loss of A-B cable (inside the dewar)
    1. Connect the reference power source to the circulator's input,
    2. Connect the reference power meter to the circulator's load port,
    3. Record the reference power meter's power level with an open output port of the circulator and call it (P3),
    4. Connect the circulator's output to port B and record the power level via the reference power level (P4),
    5. Then the two ways loss (P3-P4) in dB,
3. Cable calibration of A-C cable, C_{AC} = (P1-P2) + (P3-P4)/2.

Power source cables calibrations:

1. Cable calibrations for D to F and D to G points
    1. Connect the power meter to the point E of the RF source,
    2. Turn on the RF source and ramp up the power until the reading on the power meters is about 2/3 of the maximum limit permitted,
    3. Record the readings of the power level from the reference meter (P5) and the forward power meter (P6),

4. Turn off the RF source,
5. Measure the reference power source level (P7),
6. Measure the power level at point G with the reflected power meter (P8),
7. Connect the RF source to point E (cavity port),
8. Turn on the RF source operate power at a frequency of about 10 to 20 KHz higher or lower than the resonant frequency of the cavity,
9. Measure the forward power (P9) and the reflected power (P10),
10. The cable calibration can be expressed as follows:

1. Forward power cable corrections, $C_{D\text{-}F}$=(P5-P6+P7-P8-P9+P10)/2 in dB,
2. Reflected power cable corrections, $C_{D\text{-}G}$= (-P5+P6+3P7-3P8-P9+P10)/2 in dB.

7.5 Cavity test results

The 1.3 GHz (K-24) was assembled and vertically cold tested (2K) at Jlab in Feb 2019 for a baseline test. However, the cavity quenched at about an accelerating electric field, $\boldsymbol{E_{Acc}}$ of 13.8 MV/m with no field emission (no X-rays) and no Q-slope as shown in figure 7.9. We suspected that the cause of the early quench is thermal breakdown in some defects in the cavity RF surface. The pits at the cell equator of the cavity could be the reason of the early quench; however, it has not confirmed. In general, cavity defects (pit or bumps) enhance the applied field, which result in heat spots that grow as the field increases until the spots become normal conducting which quenches the cavity. The radiation level during the RF test was within the acceptable limits as shown in figure 7.10.

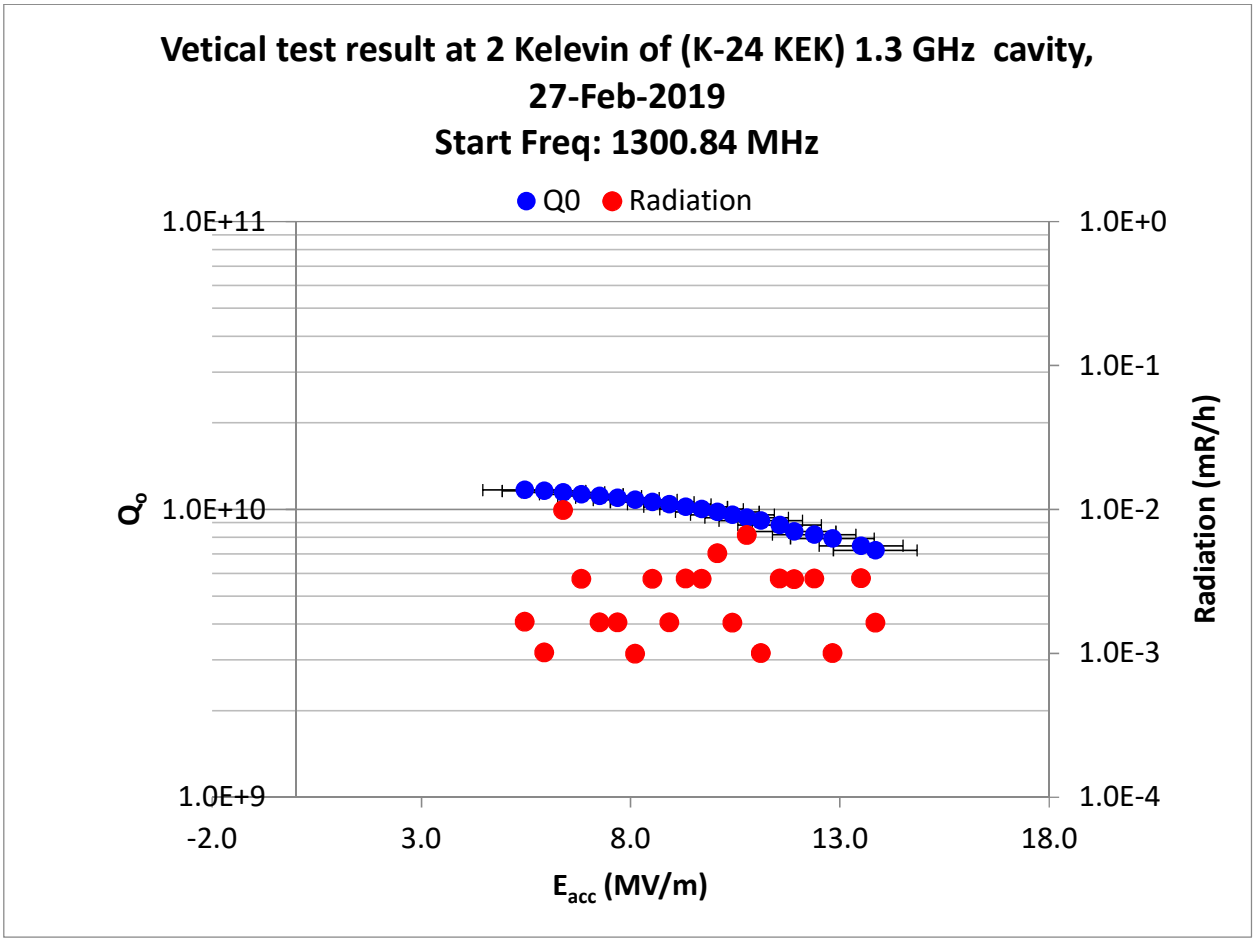

Figure 7.10: Intrinsic quality factor of 1.3 GHz cavity (K-24) versus accelerating electric fields vertical test conducted at Jlab test facility.

Since the cavity (K-24) test plan did not go as expected. Pahupati Dhakal kindly prepared a cavity from his R&D and cold tested it after nitrogen doped them. In this test, he used Buffer Chemical Polishing (BCP) instead of Electropolishing (EP) after the nitrogen-doping step to remove the niobium nitride layers (NbN). The cavity preparation and testing procedure is as follows:

1. The cavity was electropolished (EP) for 30 μm removal,
2. Cold tested cavity at 2 K for baseline test,

3. Then cavity is introduced to 2 minutes in nitrogen environment at 800 ℃ and 6 minutes vacuum,
4. Then the cavity etched by 6 μm via Buffered Chemical Polishing (BCP),
5. Cold tested the cavity at 2 K,
6. Then the cavity etched more with 3 μm surface removal again via BCP,
7. Cold tested the cavity at 2 K.

The vertical test results showed that there is an improvement in the cavity intrinsic quality factor, $\boldsymbol{Q_0}$, however the cavity quenched at early fields in comparison to the baseline test result. In addition, it showed that more cavity etching (surface removal) result higher $\boldsymbol{Q_0}$, but it still limited the accelerating electric field (gradient), $\boldsymbol{E_{Acc}}$ as illustrated in figure 7.11.

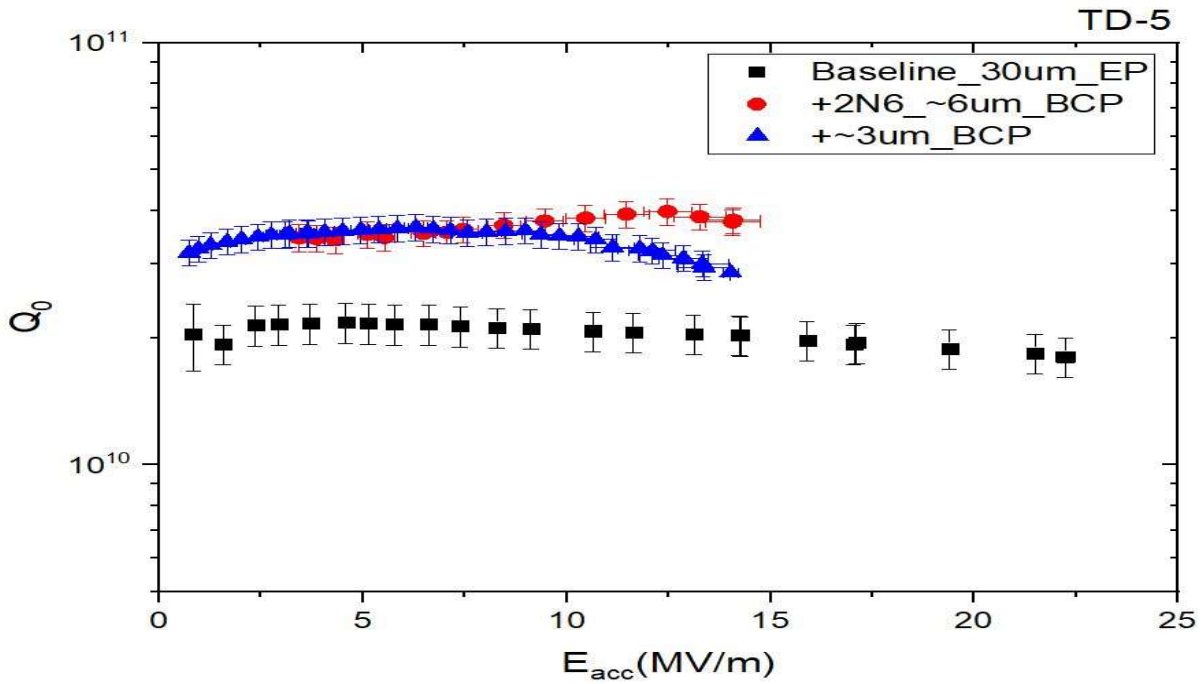

Figure 7.11: Intrinsic quality factor of 1.3 GHz cavity versus accelerating electric fields vertical test conducted at Jlab test facility.

Kenji Saito published in SRF 2001 a paper with a title "BEHAVIOR OF AIR EXPOSURE OF MEDIUM β (=0.45) NIOBIUM SC CAVITY" to report his results about the impact of air exposure on cavity performance [34]. He exposed a 1.3 GHz cavity with $\boldsymbol{\beta = 0.45}$ to air for 10 days in air (more than 78% of air is nitrogen) environment in a class 10 clean-room. The figure 7.12 shows a noticeable anti-Q slope in the cavity quality factor, $\boldsymbol{Q_0}$ and the accelerating electric field (gradient), $\boldsymbol{E_{Acc}}$. This cavity reached the fundamental limits the niobium in the magnetic field approximately, 1749 mT that corresponds to accelerating electric fields (gradient) of 46 MV/m. This is encouraging result to get high field on low/medium beta cavity for 1.3 GHz cavity.

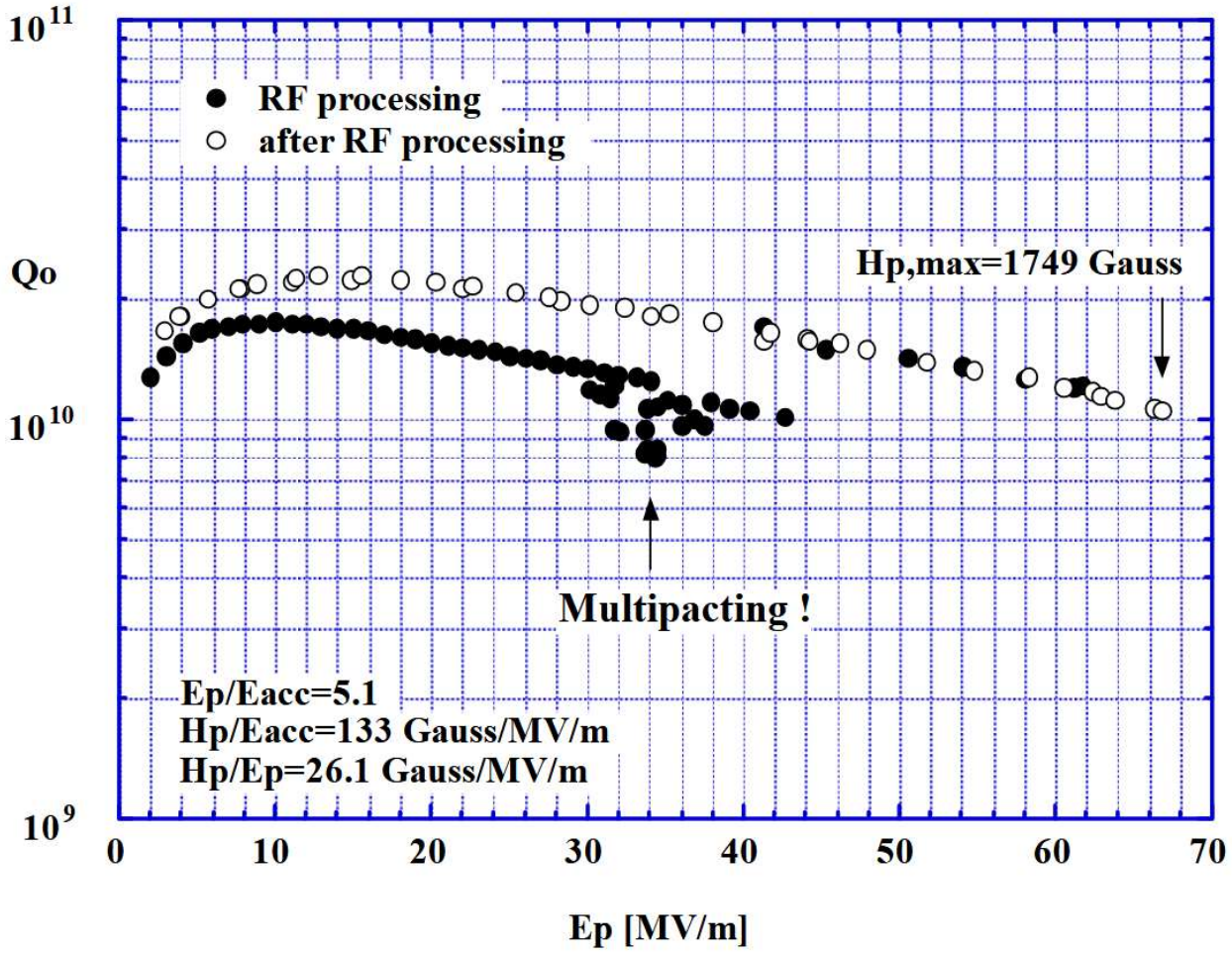

Figure 7.12: Intrinsic quality factor of 1.3 GHz cavity with β (=0.45) versus accelerating electric fields vertical test conducted at KEK test facility in 2001 by Kenji Saito.

In addition, it was experimentally observed that adding small drops of nitric acid, HNO_3 in the cavity during the electropolishing (EP) processing results an improvement in the quality factor similar to the one that was observed in nitrogen-diffused cavities. The data in the figure 7.13 suggests that the nitrogen is the main player in cavity intrinsic quality factor. Tamao Higuchi and Kenji Saito conducted this test in the early 2004. This cavity was annealed at 800 ℃, then it was processed via Centrifugal Polishing (CP) with a surface removal 18 μm then it was Electropolished (EP) etched with a surface

removal of 50 μm with small drops (~150 ppm) of nitric acid. This idea can be implemented in the EP processing in order to improve cavity intrinsic quality factor.

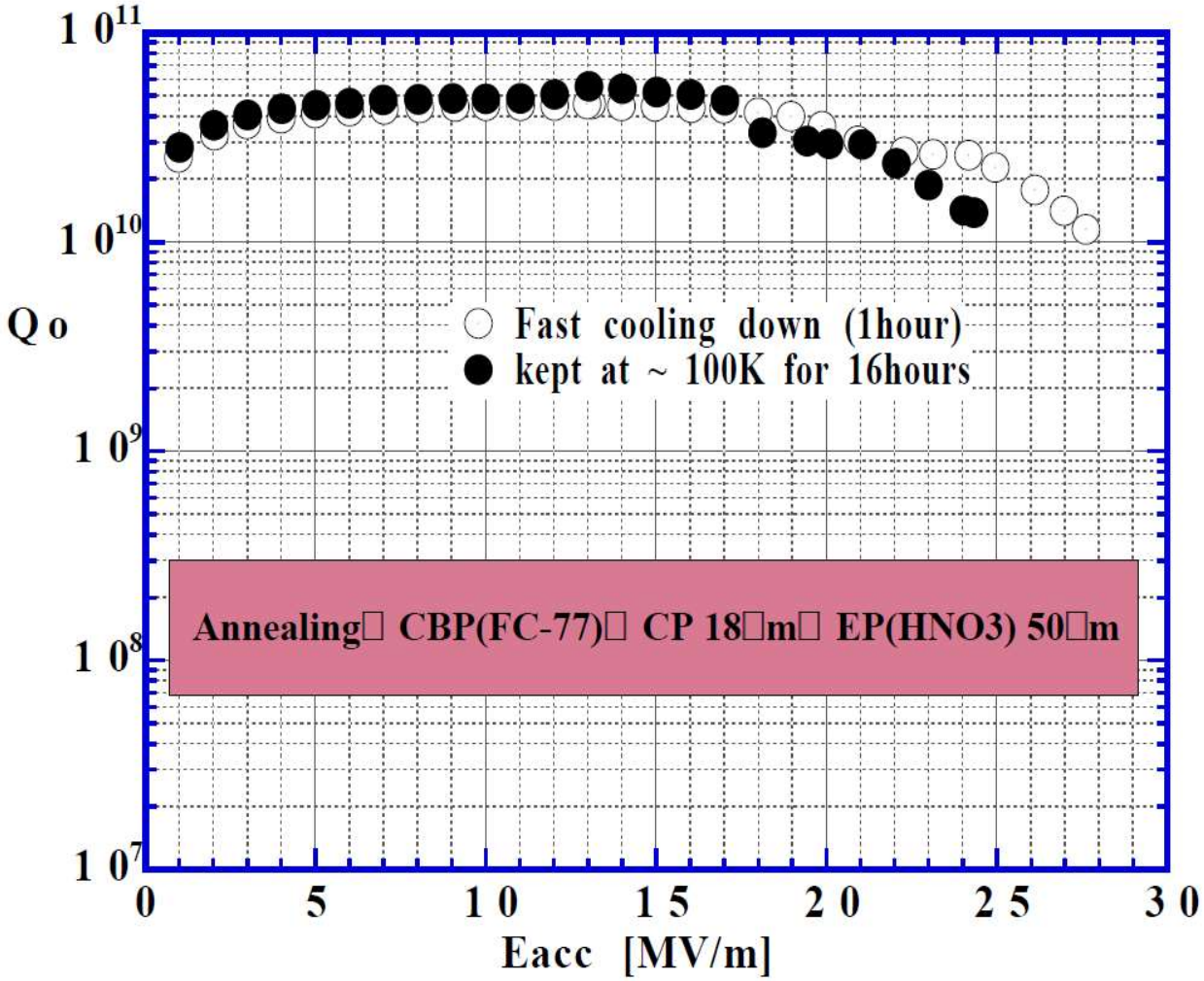

Figure 7.13: Intrinsic quality factor of 1.3 GHz cavity with (β=1) versus accelerating electric fields vertical test conducted at the KEK test facility.

8 Summary

Our studies showed that the longitudinal acceptance of the proposed high (L-band) frequency linac for medium-beta heavy ions multi-charge-state beams is sufficient for keeping the beam loss within the order limit allowing the hands-on maintenance and it preserves the beam quality (no beam loss of 20000 implies lower beam loss power than an order of several 10 W). The space-charge force and wake fields need not be considered, since the beam current is low (less than 1 mA). The simulation result is thus much more reliable than the space charge dominant case that gives rise to halo/tail formation.

The beam initial distribution was taken from FRIB linac output where a solid charge stripper (carbon foil) was used to increase uranium-238 charge states from 33 and 34 up to five charge states (76, 77, 78, 79, and 80) [10]. A slightly lower equilibrium charge state and lower energy spread would be expected if a gas charge stripper was utilized, see references [35] and [36]. The synchronous phase was tuned along the fold #3 in the FRIB linac to minimize the bunch centroids oscillations around the synchronous ion at the entrance of the high frequency section, i.e. minimize the effective longitudinal emittance. The linac filling factor is about 73.1%. End-to-end beam losses studies with more statistics is expected to further confirm that the beam losses are below one W/m for accelerator maintenance. In any case, exploiting cavity nitrogen doping technology would be beneficial for efficient cryogenics. In addition, nitrogen-doping technology has shown that it more beneficial for higher frequencies cavities. That is because the BCS surface resistance, $\boldsymbol{R_{BCS}}$ is higher than the residual surface resistance, $\boldsymbol{R_{res}}$ in higher frequencies as illustrated in figure 1.2.

APPENDIX

1. Optimization of number of cells and beta geometry for medium-beta multi-charge-state heavy ion linac

Since we used FRIB linac's output as an example for this work. At an early stage of this work, there was a proposal for improving FRIB Half-Wave Resonators (HWRs) by eliminating the High-Field-Q-Slope (HFQS), that is running the cavity at higher accelerating electric fields (Gradient) about 10 MV/m as discussed in a FRIB internal report [12]. Thus, the FRIB baseline output was considered including the improvement in HWR cavities performance. For the uranium-238 case, and the output energy is 262 MeV/u, for lighter ions such as Argon-36 the output energy is 401 MeV/u. Thus, at an early stage of this research, we used these nominal energies as initial input energies for the proposed high frequency linac to reach a final energy of ≥ 400 MeV/u.

We calculated the final energies for a few difference frequencies to find out the optimized the frequency and the cavity number of cells.

1. 644 MHz linac case, the final energy for 238U and 36Ar versus beta geometry for varies cell numbers

   The E_{acc} =16.5 MV/m, frequency = 644 MHz, final energy for 238U, q = 78, and E_i= 262 MeV/u versus beta geometry as shown in figure A1 and the final energy for 36Ar, q = 18, and E_i= 401 MeV/u versus beta geometry as plotted in figure A2.

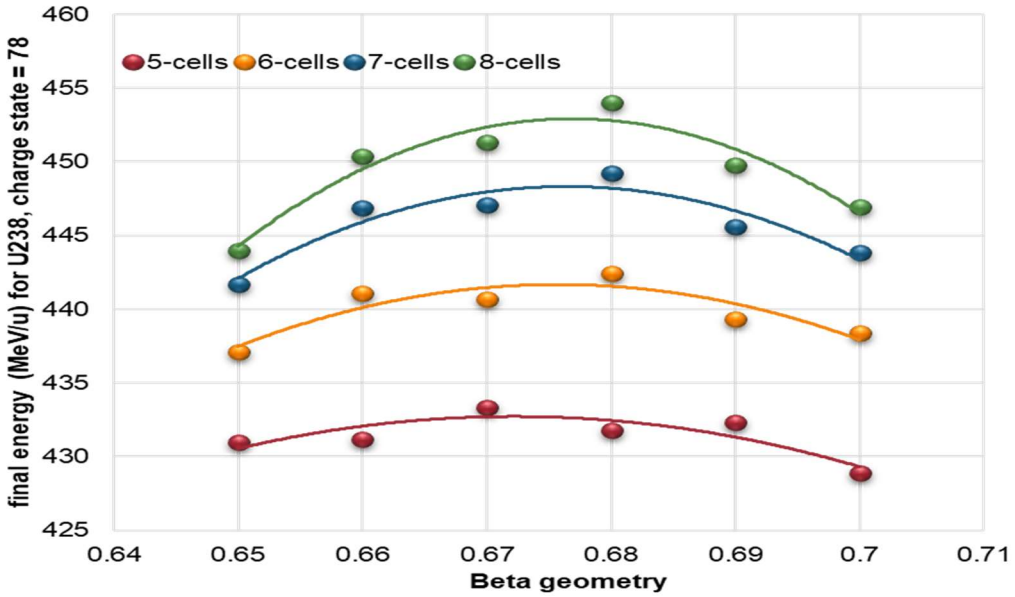

Figure A1: The E_{acc} =16.5 MV/m, frequency = 644 MHz, final energy for 238U, q = 78, and E_i= 262 MeV/u versus beta geometry.

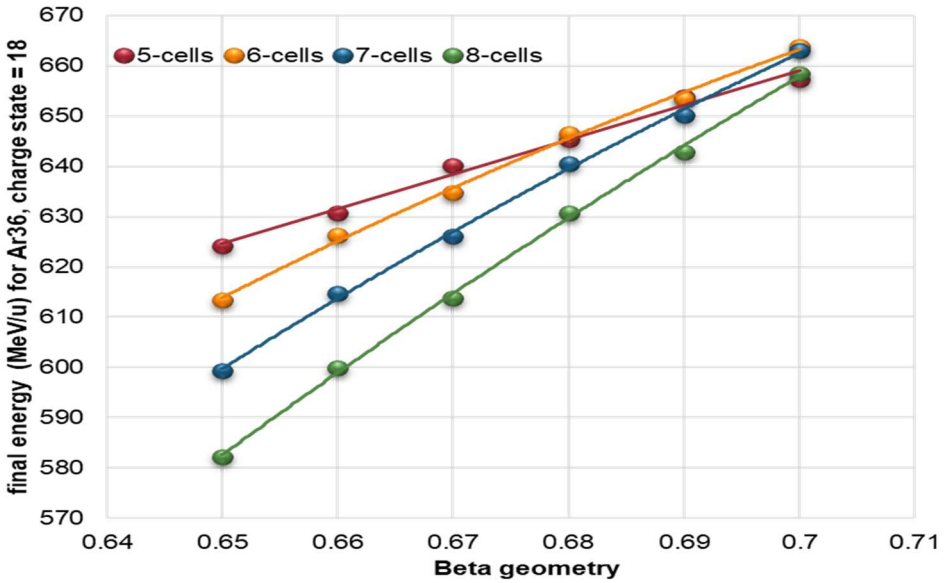

Figure A2: The E_{acc} =16.5 MV/m, frequency = 644 MHz, final energy for 36Ar, q = 18, and E_i= 401 MeV/u versus beta geometry.

2. 805 MHz linac case, the final energy for 238U and 36Ar versus beta geometry for varies cell numbers

   The E_{acc} =17.0 MV/m, frequency = 805 MHz, final energy for 238U, q = 78, and E_i= 262 MeV/u versus beta geometry as shown in figure A3 and the final energy for 36Ar, q = 18, and E_i= 401 MeV/u versus beta geometry as plotted in figure A4.

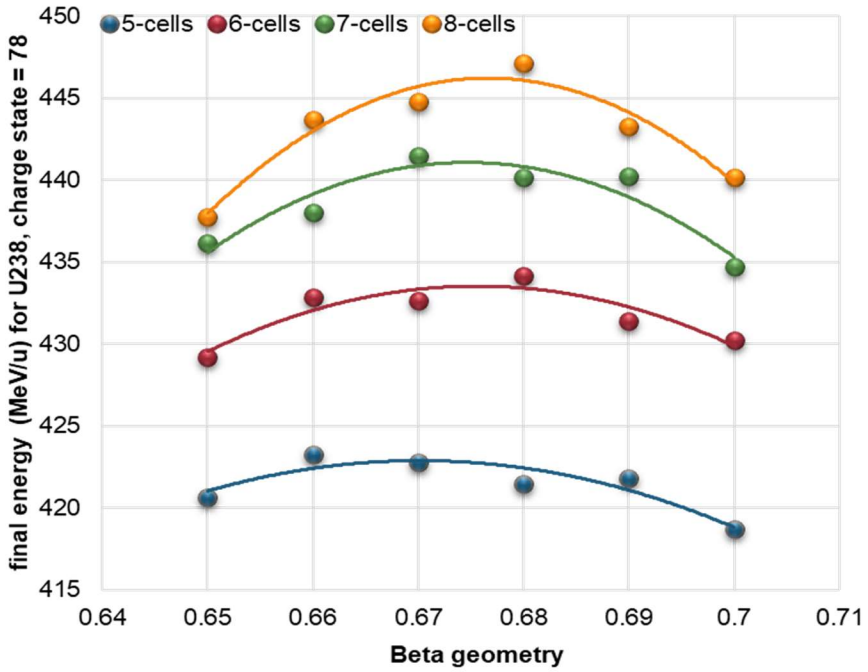

Figure A3: The E_{acc} =17.0 MV/m, frequency = 805 MHz, final energy for 238U, q = 78, and E_i= 262 MeV/u versus beta geometry.

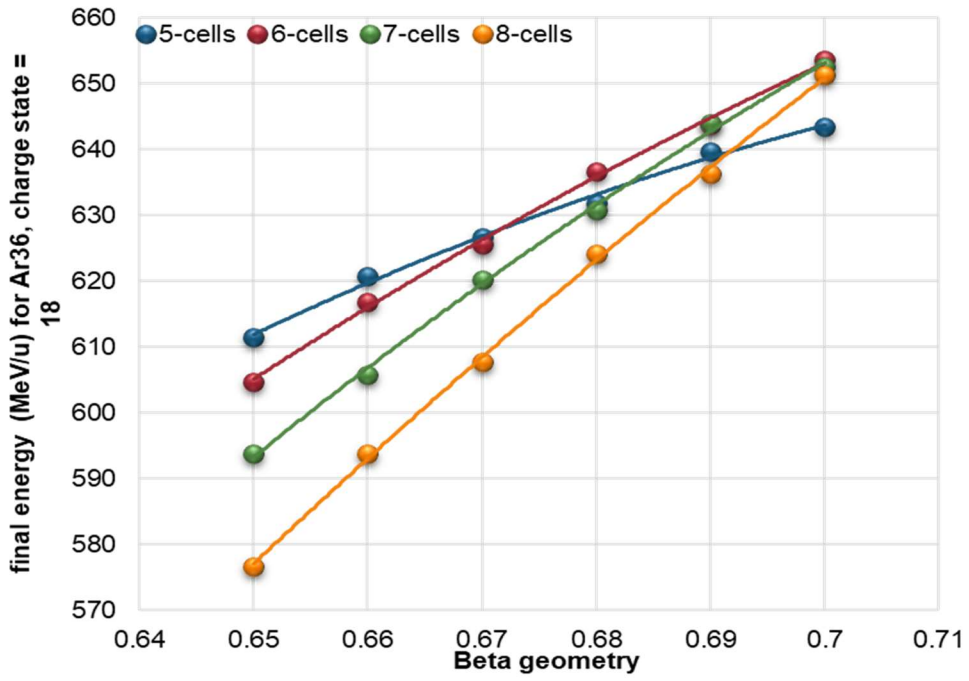

Figure A4: The E_{acc} = 17.0 MV/m, frequency = 805 MHz, final energy for 36Ar, q = 18, and E_i= 401 MeV/u versus beta geometry.

3. 966 MHz linac case, the final energy for 238U and 36Ar versus beta geometry for varies cell numbers

   The E_{acc} =17.5 MV/m, frequency = 966 MHz, final energy for 238U, q = 78, and E_i= 262 MeV/u versus beta geometry as shown in figure A5 and the final energy for 36Ar, q = 18, and E_i= 401 MeV/u versus beta geometry as plotted in figure A6.

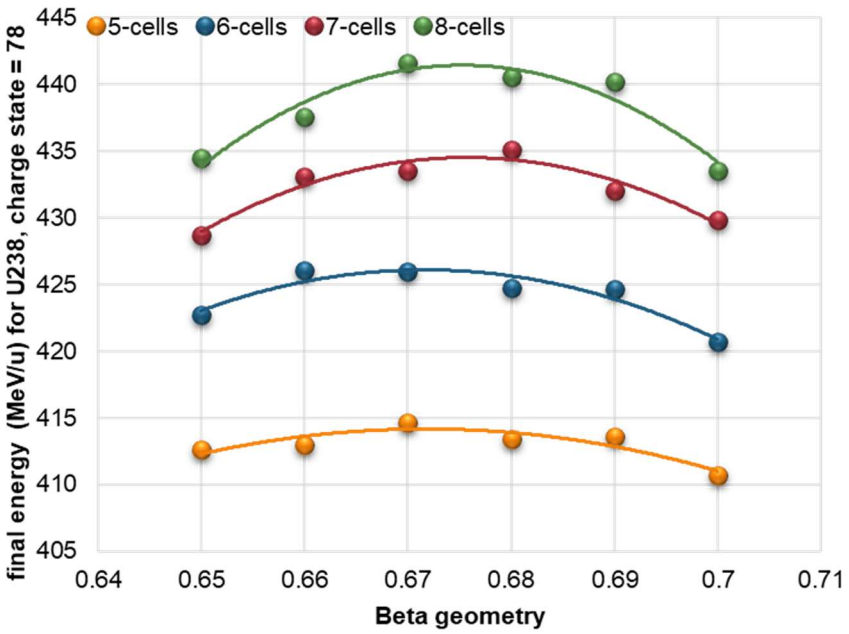

Figure A5: The E_{acc} =17.5 MV/m, frequency = 966 MHz, final energy for 238U, q = 78, and E_i= 262 MeV/u versus beta geometry.

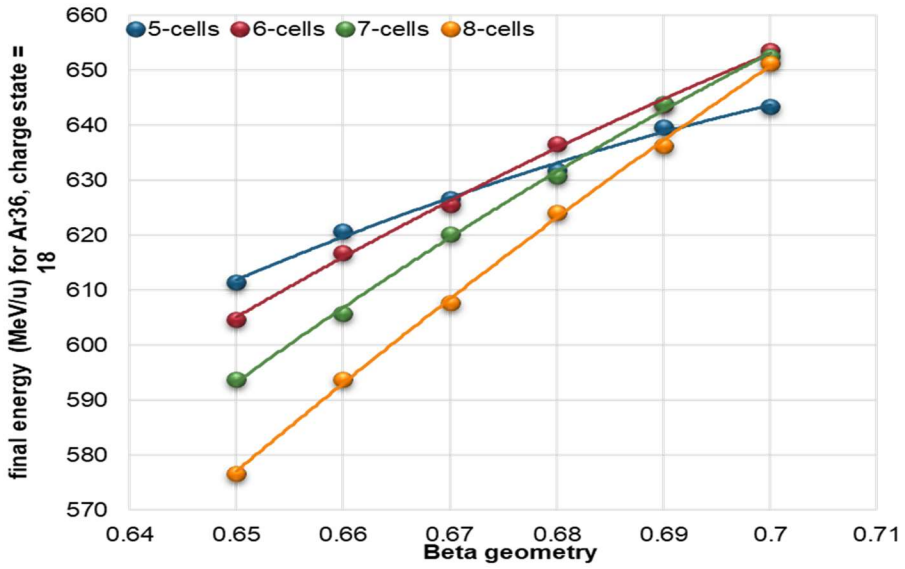

Figure A6: The E_{acc} = 17.5 MV/m, frequency = 966 MHz, final energy for 36Ar, q = 18, and E_i= 401 MeV/u versus beta geometry.

4. 1288 MHz linac case, the final energy for 238U and 36Ar versus beta geometry for varies cell numbers

   The E_{acc} =18.0 MV/m, frequency = 1288 MHz, final energy for 238U, q = 78, and E_i= 262 MeV/u versus beta geometry as shown in figure A7 and the final energy for 36Ar, q = 18, and E_i= 401 MeV/u versus beta geometry as plotted in figure A8.

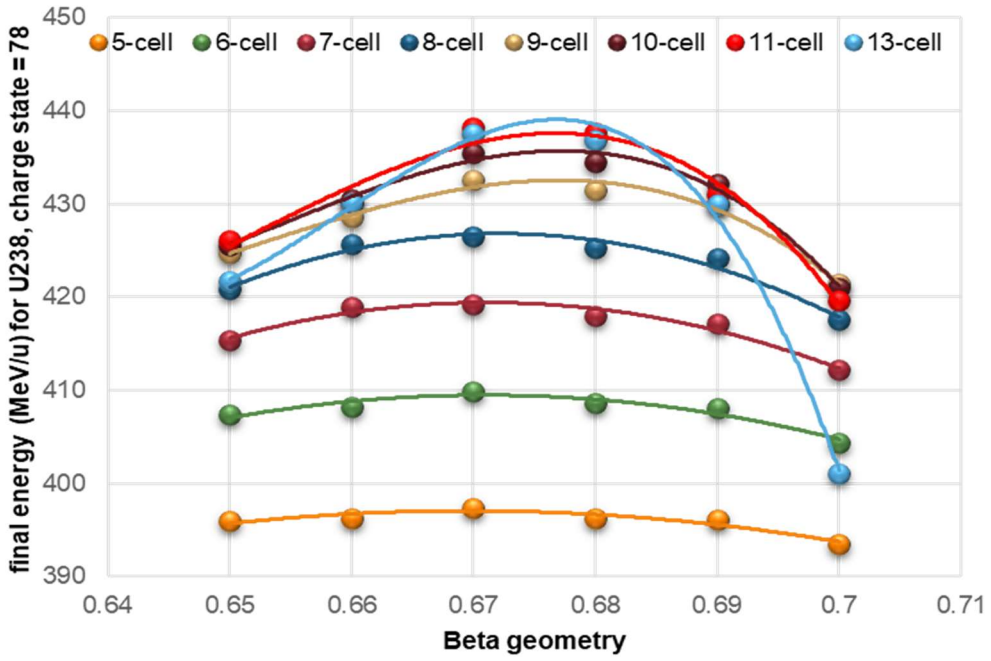

Figure A7: The E_{acc} =18.0 MV/m, frequency = 1288 MHz, final energy for 238U, q = 78, and E_i= 262 MeV/u versus beta geometry.

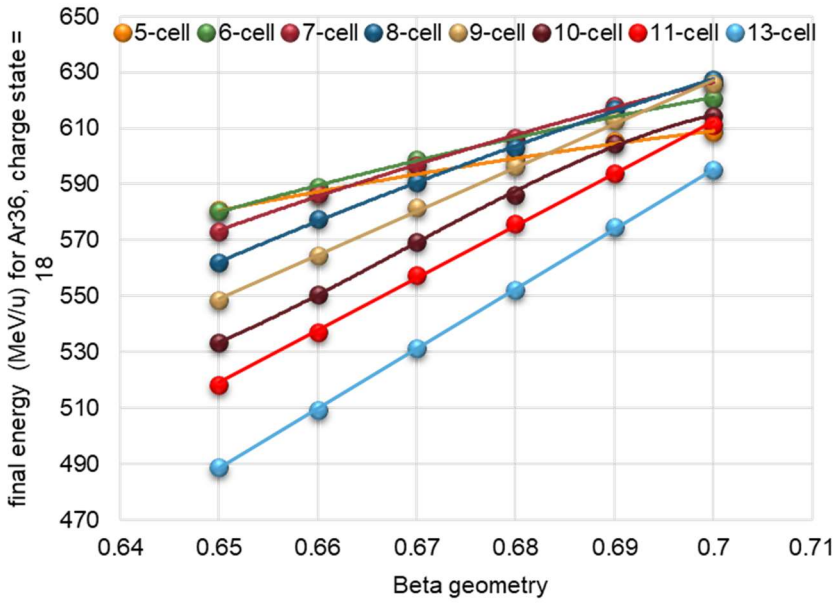

Figure A8: The E_{acc} = 18.0 MV/m, frequency = 1288 MHz, final energy for 36Ar, q = 18, and E_i= 401 MeV/u versus beta geometry.

2. Combination of Betas Option

We also have looked at how the final energy will change if we utilize two different beta geometries in 74 meters linac. A combination of betas 0.65 and 0.71 for 238U, q = 78 with final energy = 463 MeV/u. Transit time factor is plotted against beta (particle velocity) for two beta geometries as shown in figure A9. In this configuration, one obtains final energy of 463 MeV/u. The optimized beta geometries configuration is $\boldsymbol{\beta_g}$= 0.65 and $\boldsymbol{\beta_g}$ = 0.71. In contrast, for utilizing one $\boldsymbol{\beta_g}$ = 0.68 the final energy is 455 MeV/u for 238U, q = 78.

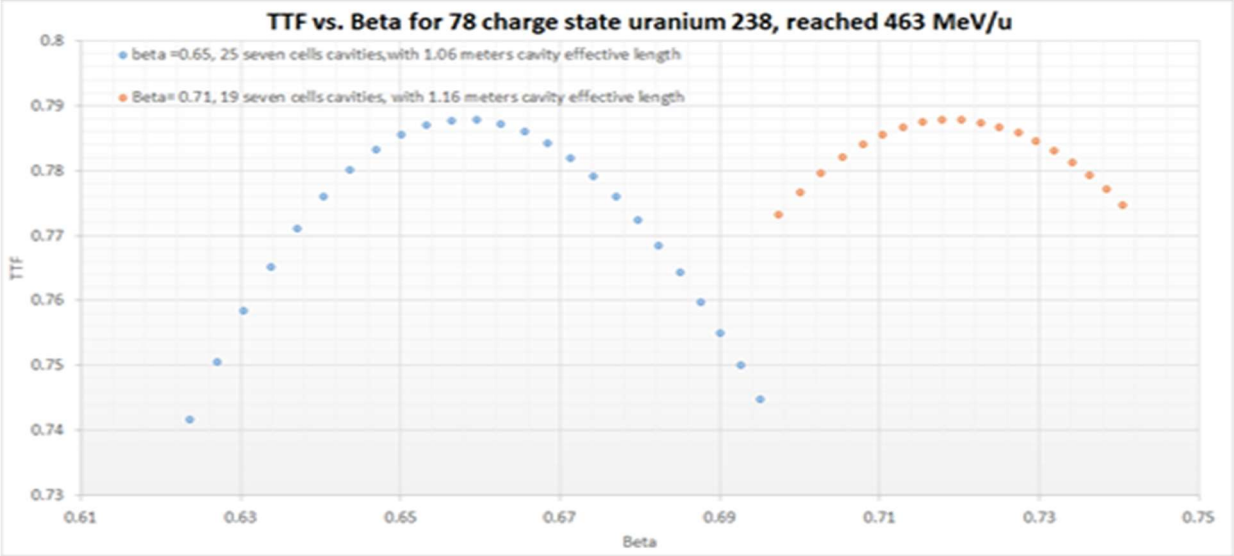

Figure A9: The E_{acc} =18.0 MV/m, frequency = 1288 MHz, final energy for 238U, q = 78, and E_i= 262 MeV/u for two optimized different beta geometries ($\boldsymbol{\beta_g}$= 0.65 and 0.71).

The energy gain per cavity for beta = 0.68 (orange dots) and combination of beta 0.65 and 0.71 (blue dots) for 238U, q = 78 is shown in figure A10. We conclude that since the difference in final energies between linac with one beta geometry is not significant compared with two betas. Moreover, two betas linac require more work than one beta linac. Therefore, one beta geometry linac is given the preference.

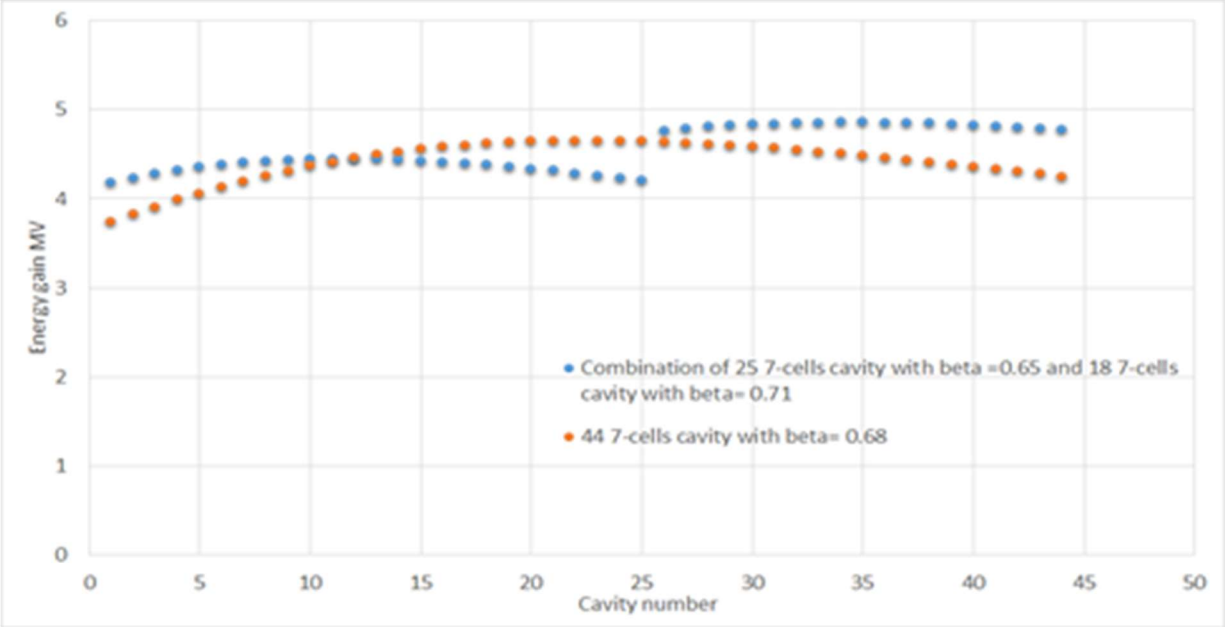

Figure A10: The energy gain per cavity for beta = 0.68 (orange dots) and combination of beta 0.65 and 0.71(blue dots) for 238U, q = 78.

Since the proposal of improving the performance of FRIB Half-Wave-Resonator (HWR) did not pass. We had to re-design the cavity and optimize it for an initial energy (output energy for FRIB baseline) of 200 MeV/u for uranium-238 an optimized beta geometry of $\boldsymbol{\beta_G = 0.61}$ that is suitable for heavy and lighter ions with 6-cell cavity.

3. 1288 MHz 6-cell cavity with shape optimization

The electromagnetic design of the 1288 MHz cavity with beta geometry of $\boldsymbol{\beta_G}$ was optimized using the code SUPERFISH. The typical design criteria is minimizing the peak surface electric field, $\boldsymbol{E_{peak}}$ and the peak surface magnetic field, $\boldsymbol{H_{peak}}$. In general, to lower the cavity $\boldsymbol{E_{peak}}$, one should make the surface of the region A blended with bigger radius (in pillbox shape the edges at the mid-cell entrance/exist are sharp, i.e. field emission would be more probable to occur) as shown in figure

A11. To lower the $\boldsymbol{H_{peak}}$, one should make the volume bigger (it is called in the SRF community by Low loss shape, LL shape) at the high magnetic field region denoted by region B in Figure A11. In addition, minimizing the multi-pacting by making the cavity shape elliptical. First, we designed the mid-cell and optimized its shape with reasonable $\boldsymbol{E_{peak}}$ and $\boldsymbol{H_{peak}}$, then similarly we designed the end cell with beam port and then finally we designed half-cavity to reduce the calculation time in SUPERFISH code as shown in figure A11.

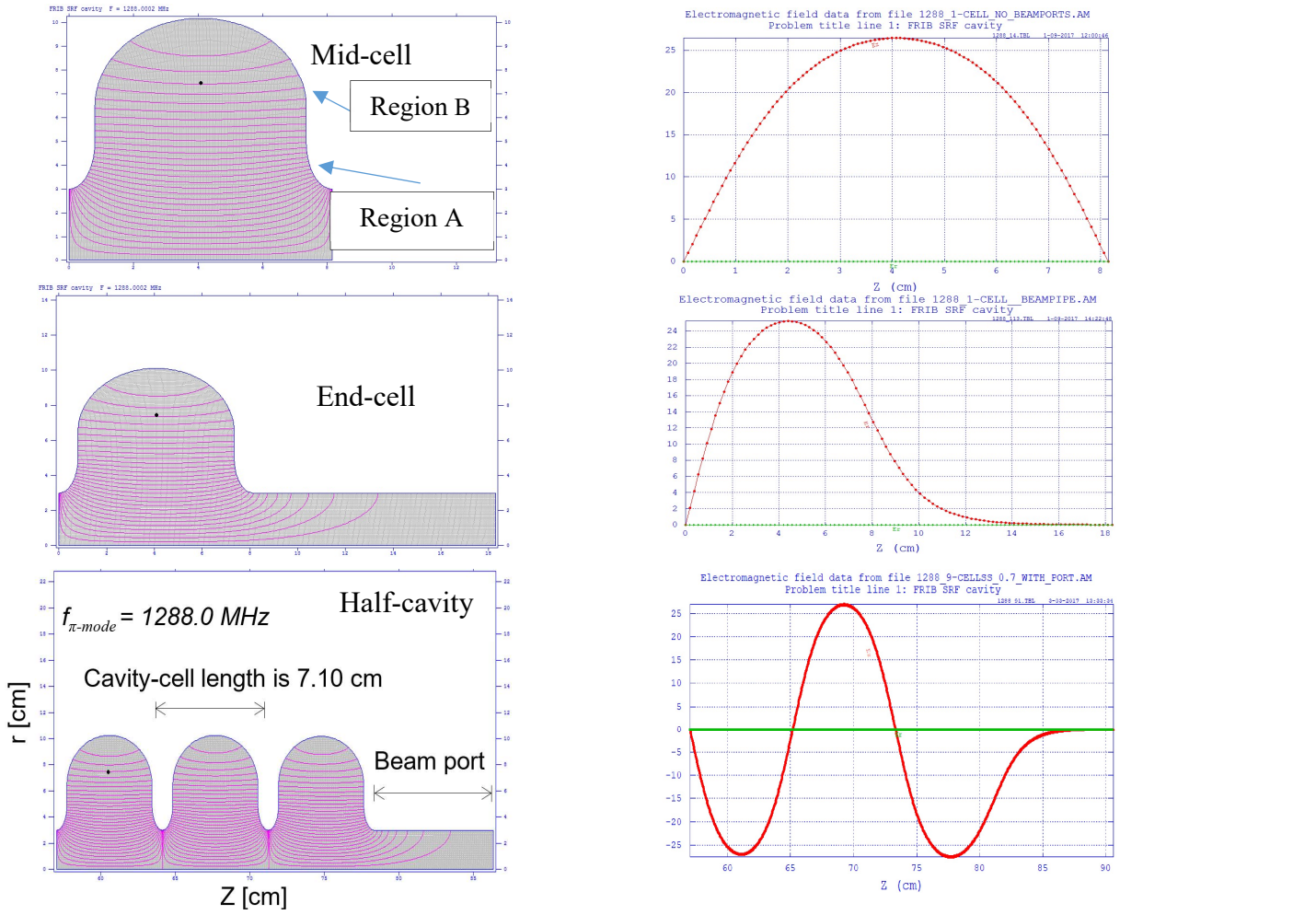

Figure A11: Left is the mid-cell optimized its shape with reasonable $\boldsymbol{E_{peak}}$ and $\boldsymbol{H_{peak}}$, end-cell design and half 6-cell cavity optimized shape. Right the accelerating electric field along the mid-cell, end-cell, and half 6-cell cavity at the cavity center.

4. The beam dynamics code TRACK

This code was intensively used in the beam dynamics simulations. It has a manual document that explains the mathematics behind the code routines. It is a linac end-to-end beam simulation code. It takes into consideration the initial distribution of a DC beam from the ion source to the target. In other words, it has the capability to simulate all accelerator components mentioned in Chapter 5 and 6 with 3D realistic

electromagnetic fields and even more. It can also calculate the longitudinal acceptance by starting with a rectangular or square beam distribution at the linac entrance as shown in figure A12 and then inject it to the linac, then track all particle along the linac components and then it can filter out the lost particles at the linac out let as shown in figure A13.

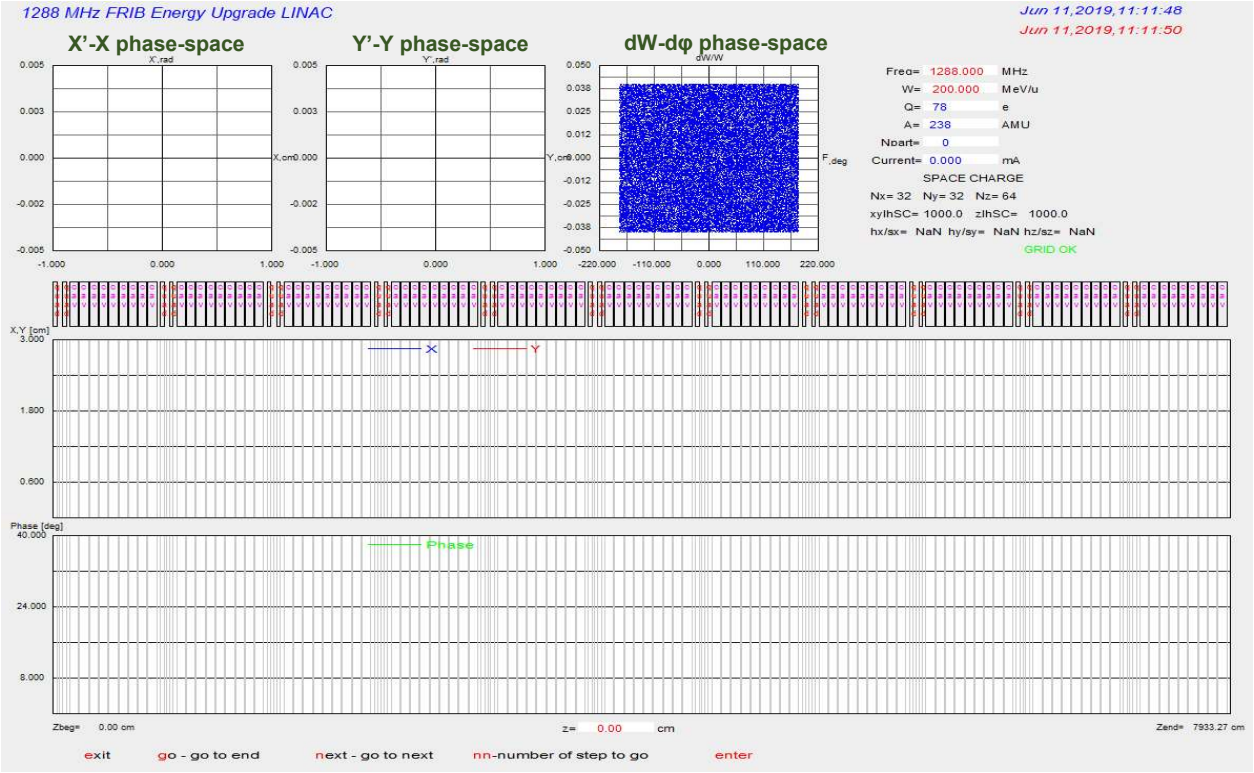

Figure A12: TRACK code graphic interface with a rectangular beam distribution show in blue for longitudinal acceptance calculations.

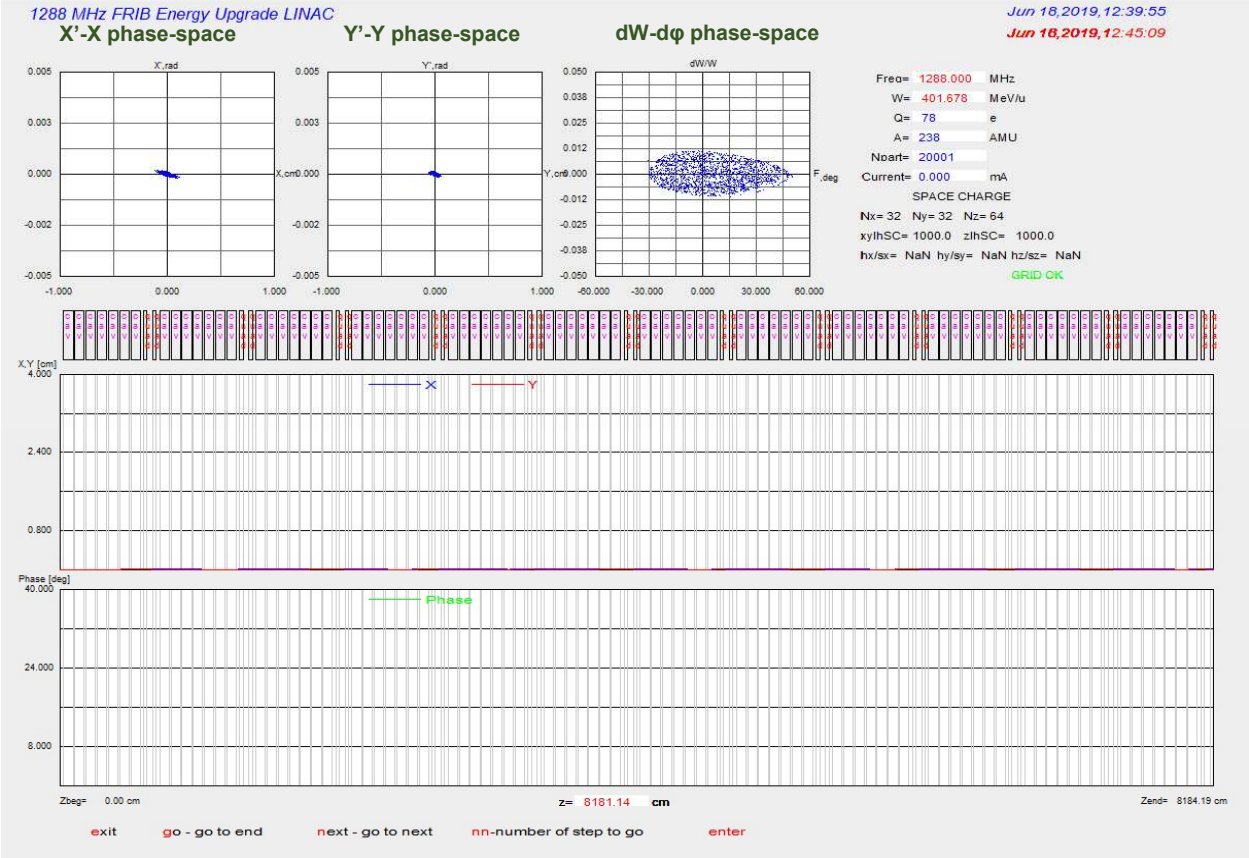

Figure A13: TRACK code graphic interface shown the longitudinal acceptance in blue (survived ions in the longitudinal phase-space at the linac outlet).

5. Beam dynamics simulation comparison between hard-edge and 3D magnetic quadrupole fields for 1288 MHz medium-beta linac

The 3D magnetic quadrupole fields can be viewed via “Plot TRACK 3D fields” feature in TRACK code supplement. Figure A14 shows the output fields for the 3D fields.

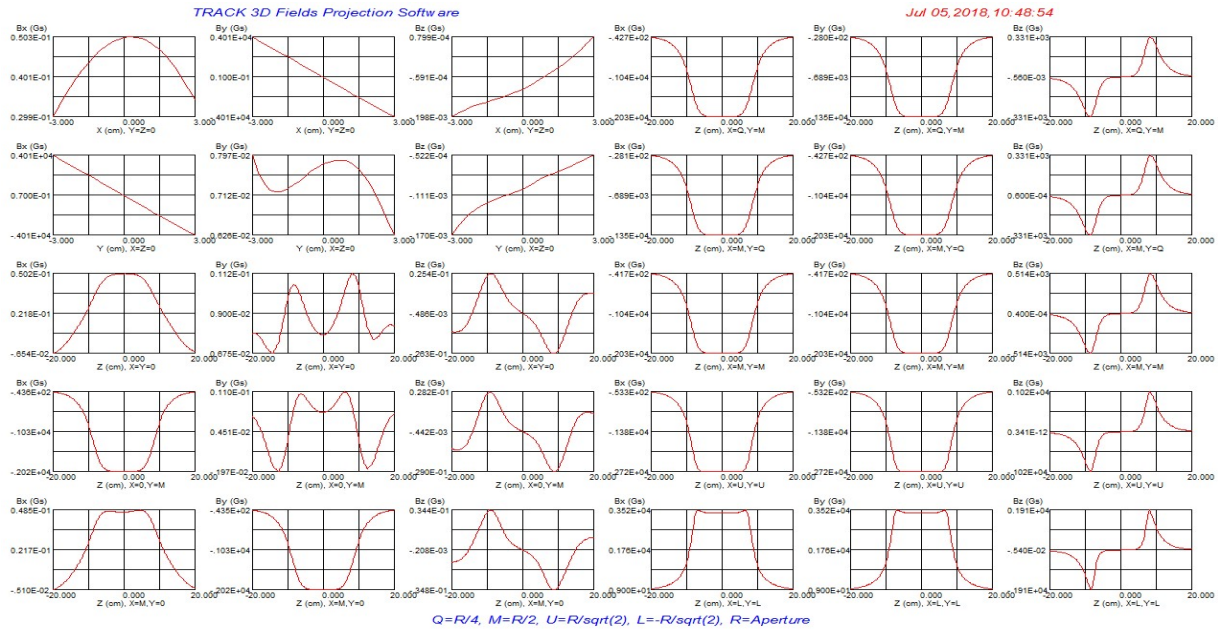

Figure A14: 3D fields for the magnetic quadrupole on Plot TRACK 3D fields.

The transverse beam envelope was tracked along the linac for both the hard-edge and 3D magnetic quadrupole fields as shown in figure A15. There is a slight difference in the transverse beam envelope between the hard-edge and the 3D fields as seen in the quadrupole 20 location, where Y_{max} was bigger than X_{max} in the hard-edge case, while in the 3D fields case Y_{max} was smaller than X_{max}. That is due to fringe field effect.

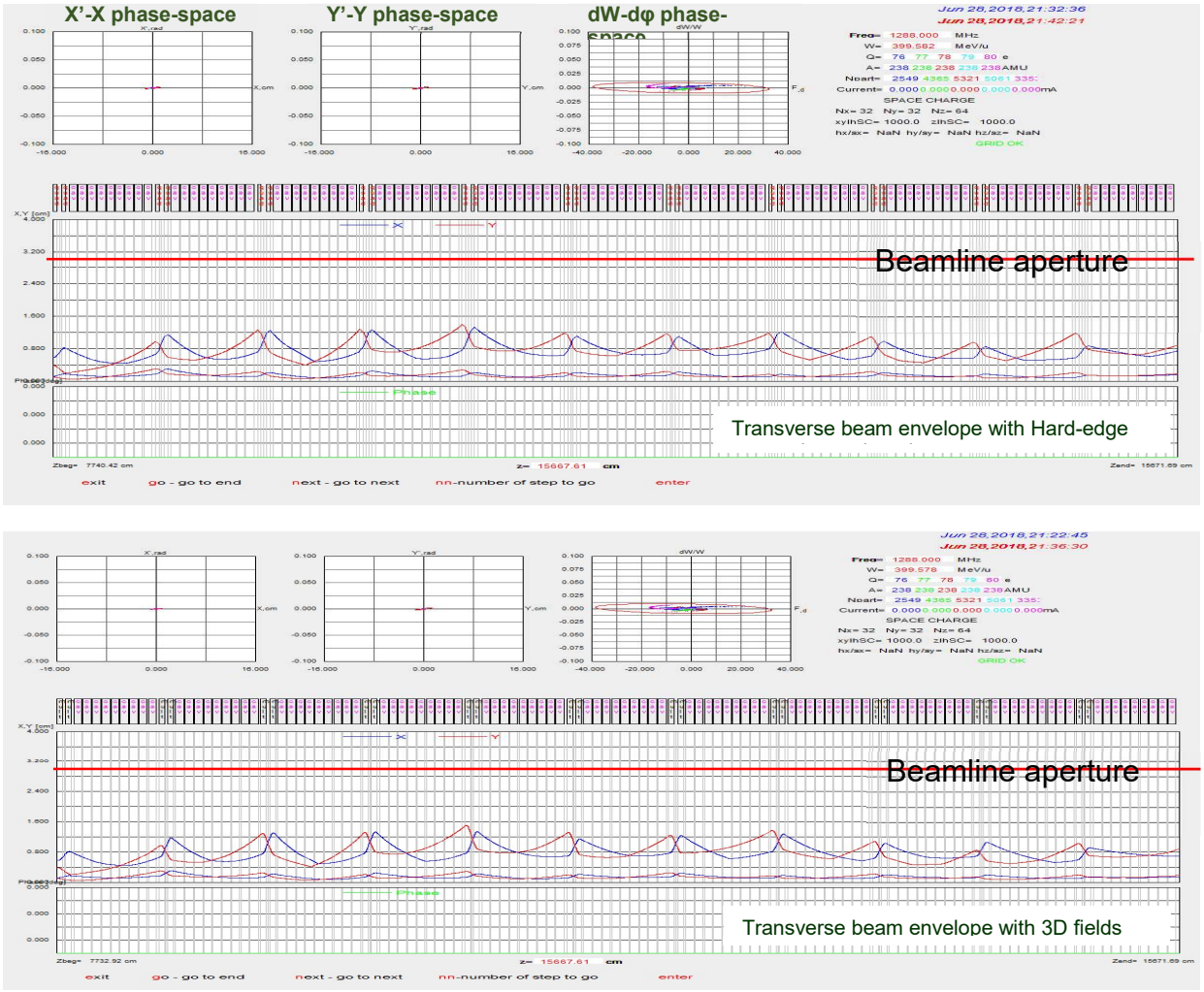

Figure A15: Beam dynamics simulation comparison between hard-edge and 3D magnetic quadrupole fields for 1288 MHz medium-beta linac.

6. Error calculations for the accelerating electric field (gradient), $\boldsymbol{E_{acc}}$ and cavity intrinsic quality factor, $\boldsymbol{Q_0}$

The uncertainty in the accelerating electric field (gradient), $\boldsymbol{E_{acc}}$ was calculated using the standard form shown in formula (1). The error in the accelerating electric field, $\Delta\boldsymbol{E_{acc}}$ is calculated as in the formula (2) [32].

$$\frac{\Delta X(y,z)}{X} = \sqrt{\left(\frac{\partial X}{\partial y}\Delta y\right)^2 + \left(\frac{\partial X}{\partial z}\Delta z\right)^2} \quad (1)$$

$$\frac{\Delta E_{acc}}{E_{acc}} = \frac{1}{2}\sqrt{\left(\frac{\left(2P_f + C_\beta\sqrt{P_f P_r}\right)}{2\left(P_f + C_\beta\sqrt{P_r P_f}\right)}\frac{\Delta P_f}{P_f}\right)^2 + \left(\frac{\sqrt{P_r}}{2\left(\sqrt{P_f} + C_\beta\sqrt{P_r}\right)}\frac{\Delta P_r}{P_r}\right)^2 + \left(\frac{\Delta\tau}{\tau}\right)^2} \quad (2)$$

Similarly, the uncertainty in the cavity quality factor, Q_0 was calculated using the standard form shown in formula (1). The error in the quality factor measurement, ΔQ_0 is calculated as in the formula (3) [32].

$$\frac{\Delta Q_0}{Q_0} = \sqrt{\left(\left(\frac{\left(2P_f + C_\beta\sqrt{P_f P_r}\right)}{2\left(P_f + C_\beta\sqrt{P_r P_f}\right)} - \frac{P_f}{P_{Disp}}\right)\frac{\Delta P_f}{P_f}\right)^2 + \left(\left(\frac{\left(C_\beta\sqrt{P_r P_f}\right)}{2\left(P_f + C_\beta\sqrt{P_r P_f}\right)} + \frac{P_r}{P_{Disp}}\right)\frac{\Delta P_r}{P_r}\right)^2 + \left(\frac{\Delta\tau}{\tau}\right)^2} \quad (3)$$

Here, P_f is the forward power, P_r is the reflected power, C_β is 1 for under coupled and -1 for over coupled,

BIBLIOGRAPHY

BIBLIOGRAPHY

[1] M. Martinello et al. SRF 2017 (TUYAA02), TTC Meeting FNAL 2017, TTC Meeting Milan 2018, IPAC 2018 (WEPML013).

[2] S. Shanab, K. Saito, and Y. Yamazaki, "Investigation of the Possibility of L-band SRF Cavities for Medium-Beta Heavy Ion Multi-Charge-State Beams", in the publication processing, Nuclear Inst. And Methods in Physics Research, A, 2019.

[3] P.N. Ostroumov, V.N. Aseev, B. Mustapha, "TRACK – a Code for Beam Dynamics Simulation in Accelerators and Transport Lines with 3D Electric and Magnetic Fields", TRACK code manual, version 39, 2017.

[4] J.K. Sekutowicz. "Superconducting Elliptical Cavities", Desy, Hamburg, Germany, https://arxiv.org/ftp/arxiv/papers/1201/1201.2598.pdf.

[5] J. Jackson. "Classical Electrodynamics" John Wiley & Sons, Inc. ISBN: 04714331, 1962.

[6] "Fundamentals of RF cavities", lecture notes, USPAS, 2016, https://casa.jlab.org/publications/viewgraphs/USPAS2016/L_10_Fundam_RF_Cav.pdf.

[7] CST Microwave Studio, User's Manual, 2017, CST GmbH, Darmstadt, Germany, http://www.cst.de/.

[8] A. Jana et al., "Electromagnetic Design of β = 0.9, 650 MHz Superconducting Radiofrequency Cavity" IEEE Trans. of Appl. Superconduct., Aug. 2013.

[9] T. P. Wangler, "INTRODUCTION TO LINEAR ACCELERATORS", Los Alamos Nat'l Lab report, 1993.

[10] Peter Ostroumov. Private communications, 2017.

[11] Qiang Zhao. Private communications, 2018.

[12] G. D. Shirkov, "A classical model of ion confinement losses in ECR ion sources", Plasma Sources Sci. Technol. 2 (1993) 250-257.

[13] F. Marti and Alberto Facco, internal report, FRIB 2016.

[14]P. Duchesne et al., “Design of the 352 MHz, Beta 0.50, Double-Spoke Cavity for ESS”, Proc. 16th International Conference on RF Superconductivity, Paris, France, (2013).

[15]P. N. Ostroumov et al., “Elliptical superconducting RF cavities for FRIB energy upgrade” Nuclear Inst. and Methods in Physics Research, A 888 (2018).

[16]D. Jeonet al., “Design of the RAON Accelerator Systems”, JKPS, vol. 65, No. 7, pp. 1010-1019, 2014.

[17]K. Halbach, R.F. Holsinger, SUPERFISH-A Computer Program for Evaluation of RF Cavities with Cylindrical Symmetry, Particle Accelerators 7, pp. 213–222, 1976.

[18]T. Raubenheimer, M. Ross, J. Chan, D. Schultz, “SCRF 1.3 GHz Cryomodule,” LCLS-II physics requirements document. pp. 3-4, 2014.

[19]K. Saito. “CRITICAL FIELD LIMITATION OF THE NIOBIUM SUPERCONDUCTING RF CAVITY” in the 10th Workshop on RF Superconductivity, Tsukuba, Japan, 2001.

[20]Takashi, Yoshimoto, private communication, 2018.

[21]P. N. Ostroumov, V. N. Aseev, B. Mustapha, “Beam loss studies in high-intensity heavy-ion linacs”, Phys. Rev. ST Accel. Beams 7, 090101, 2004.

[22]S. Hacıömeroğlu. Y. K. Semertzidis, “Systematic errors related to quadrupole misplacement in an all-electric storge ring for proton EDM experiment”, arXiv:1709.01208v1 [physics.acc-ph], September, 2017.

[23]P. Kuske, K. Ott, “BEAM-BASED ALIGNMENT AT BESSY”, Proceedings of the Fifth European Particle Accelerator Conf. C960610, mop001l, p. 887-889, 1996.

[24]J. Bardeen, “TWO-FLUIDMODELOFSUPERCONDUCTIVITY” Physical Review Letters, volume 1, 1958, https://journals.aps.org/prl/pdf/10.1103/PhysRevLett.1.399.

[25]K. Saito, P. Kneisel, “Temperature Dependence of the Surface Resistance of Niobium at 1300 MHz- Comparison to BCS Theory” Proceedings of the 1999 Workshop on RF Superconductivity (tup031), New Mexico, USA, 1999.

[26]J. Bardeen, L. N. Cooper, AND J.R. Schrieffer, “Microscopic Theory of Superconductivity”, PhysRev.106.162. 1957.

[27]P. Bauer, “Review of Models of RF Surface Resistance in High Gradient Niobium Cavities for Particle Accelerators Revision 1” TD-04-014, Fermilab, Technical Division, December 2004.

[28]A. Romanenkoa, A. Grassellinob, O. Melnychuk, and D. A. Sergatskov, "Dependence of the residual surface resistance of superconducting radio frequency cavities on the cooling dynamics around Tc" Journal of Applied Physics 115, 184903 (2014); https://doi.org/10.1063/1.4875655.

[29]D. Gonnella, et al., Industrialization of the nitrogen-doping preparation for SRF cavities for LCLS-II, Nuclear Instruments and Methods in Physics Research A, 2018.

[30]T. Kubo and A. Gurevich, "Field-dependent nonlinear surface resistance and its optimization by surface nano-structuring of SRF cavities", SRF 2019 (THFUA4), Dresden, Germany, 2019.

[31]P. Dhakal, et al., Effect of low temperature baking in nitrogen on the performance of a niobium superconducting radio frequency cavity, PRAB, 2018.

[32]P. Dhakal, G. Ciovati, P. Kneisel and G. Rao Myneni, "Enhancement in Quality Factor of SRF Niobium Cavities by Material Diffusion", IEEE Transactions on Applied Superconductivity (Volume: 25, Issue: 3), June 2015.

[33]T. Powers, "THEORY AND PRACTICE OF CAVITY RF TEST SYSTEMS", Proceedings of the 12thInternational Workshop on RF Superconductivity (sup02), Cornell University, Ithaca, New York, US, 2005.

[34]K. Saito, "Behavior of air exposure of medium β (=0.45) niobium SC cavity", Proceedings of the 10th workshop on RF superconductivity (PH004), SR 2001.

[35]H. Imao et al., "Charge stripping of 238U ion beam by helium gas stripper", Phys. Rev. ST Accel. Beams 13, 123501, 2010.

[36]H. Okuno et al., "Low-Z gas stripper as an alternative to carbon foils for the acceleration of high-power uranium beams", Phys. Rev. ST Accel. Beams 14, 033503, 2011.